

Spin Transport in an Ultra-cold Trapped Non-condensed ^{87}Rb Gas

by

Dorna Niroomand

M.Sc., Simon Fraser University, 2013

B.Sc., Ferdowsi University of Mashhad, 2007

Thesis Submitted in Partial Fulfillment of the
Requirements for the Degree of
Doctor of Philosophy

in the
Department of Physics
Faculty of Science

© Dorna Niroomand 2018
SIMON FRASER UNIVERSITY
Fall 2018

Copyright in this work rests with the author. Please ensure that any reproduction or re-use is done in accordance with the relevant national copyright legislation.

Approval

Name: Dorna Niroomand

Degree: Doctor of Philosophy

Title: Spin Transport in an Ultra-cold Trapped
Non-condensed ^{87}Rb Gas

Examining Committee: **Chair:** Igor Herbut
Professor

Jeffrey McGuirk
Senior Supervisor
Associate Professor

Paul Haljan
Supervisor
Associate Professor

Malcolm Kennett
Supervisor
Associate Professor

Stephanie Simmons
Internal Examiner
Assistant Professor

Kirk Madison
External Examiner
Associate Professor
Department of Physics & Astronomy
University of British Columbia

Date Defended: September 11, 2018

Abstract

Ultra-cold trapped atoms, with their high degree of tunability, provide ideal model systems to study physical phenomena with applications in many different fields of research. This thesis describes studies on spin transport phenomenon in a trapped ultra-cold spin-polarized ^{87}Rb gas at temperatures above quantum degeneracy. This work is focused on the less studied regime of cross-over between classical and quantum transport. Diffusion is a fundamental dissipative process that tends to relax any system towards a state of minimum inhomogeneity. In this work we study longitudinal spin diffusion as a special case of spin transport. The system studied here consists of two anti-parallel longitudinal spin domains separated by a helical domain-wall. We report that the diffusion process manifests a significant deviation from classical diffusion due to purely quantum mechanical modifications.

The two-domain spin textures are prepared using optical and microwave pulse techniques, and the dynamics of the spin structure is studied as it relaxes towards the final equilibrium state. Generally, there is a wide range of parameter space that could be studied. In this work we focused our studies on the effects related to the degree of coherence in the domain-wall as well as the effective magnetic field acting on the spins. By controllably tuning these experimental parameters, we studied in detail how the spatiotemporal behaviour of the diffusion dynamics is modified. Our results show that the longitudinal spin diffusion time scales depend sensitively on the domain-wall degree of coherence. External magnetic field gradients also alter the dynamics noticeably, manifesting a significant dependence on the sign of the applied field gradients.

Keywords: Ultra-cold trapped gases, Spin transport, Spin diffusion

Dedication

To my family

Acknowledgements

I would like to express my gratitude to my supervisor Dr. Jeffrey McGuirk, for his guidance and support. I am also thankful of my committee members Dr. Malcolm Kennett and Dr. Paul Haljan, for the challenging discussions and their helpful advice. Thanks to everyone in McGuirk group for the fun and collaborative environment to work in.

I am grateful to all members of the SFU Physics Department faculty and staff, for the friendly and relaxed working environment at SFU physics.

Thanks to all my friends, for making life more colorful. Special thanks to Azadeh, Alireza and Majid for being amazing friends and extremely supportive during the difficult times. Last and foremost, thanks to my family for their love and support.

Table of Contents

Approval	ii
Abstract	iii
Dedication	iv
Acknowledgements	v
Table of Contents	vi
List of Figures	ix
1 Introduction	1
2 Spin dynamics theory	7
2.1 A two-level system coupled to an electromagnetic field	7
2.1.1 Bloch-sphere representation and optical resonance	8
2.2 Description of the system and the dynamics	9
2.2.1 The spin transport equation	10
2.2.2 Collisional method for derivation of the transport equation	11
2.2.3 Effects of binary collisions on the spin density matrix	12
2.2.4 Derivation of the quantum Boltzmann equation	18
2.3 Effect of collective behaviour on spin diffusion in a trapped ^{87}Rb gas	22
2.3.1 Spin diffusion	24
2.3.2 Spin waves and Castaing's instability	25
2.3.3 Spin diffusion in effective magnetic field gradients	28

3	Experimental setup	30
3.1	BEC system and ultra-cold atom preparation	30
3.2	Experimental setup for spin transport studies	37
3.2.1	Uniform differential potential	40
3.2.2	The ac Stark effect and the light shift	41
3.3	Spin transport measurement	43
3.3.1	Ramsey spectroscopy	43
3.3.2	The experimental method for reconstructing spin	47
3.4	Spin profile initialization	49
4	Spin transport study in a trapped Bose gas	56
4.1	Introduction	56
4.1.1	Review of spin transport studies in ultra-cold gases	57
4.2	Quantum mechanical modifications to longitudinal spin diffusion in a non- condensed Bose gas	60
4.2.1	Experimental study of longitudinal spin diffusion in uniform magnetic fields	62
4.3	The effect of the initial transverse spin magnitude in the domain-wall	67
4.4	Discussion	73
4.5	Summary	76
5	Spin diffusion dynamics in inhomogeneous effective magnetic fields	77
5.1	Introduction	77
5.1.1	Review of ISRE-driven spin dynamics studies in nonuniform magnetic fields	79
5.2	Diffusion in a nonuniform effective magnetic field with linear symmetry . .	81
5.3	Effective magnetic field	83
5.3.1	Linear inhomogeneities in differential potential	84
5.4	Longitudinal diffusion results in applied linear field gradients	86
5.4.1	Longitudinal domain dipole oscillation	88

5.4.2	Transverse spin dynamics in the domain-wall	92
5.5	Discussion	95
5.6	Summary	101
6	Conclusion and future direction	103
	Bibliography	107

List of Figures

Figure 2.1	Bloch-sphere representation of the state vector $\vec{\psi}$ of a two-level system. The North pole corresponds to the excited state $ 2\rangle$ and the South pole corresponds to the ground state $ 1\rangle$. The azimuthal angle ϕ represents the relative phase of the superposition state.	9
Figure 2.2	Bloch-sphere representation of Rabi flopping. The black dashed vector shows the coupling field torque vector $\vec{\Omega}$, the blue vector shows the state vector $\vec{\psi}$ and the dotted line shows the path of the oscillation of the Bloch vector. The coupling field is (a) in resonance with the atomic transition and (b) detuned from resonance.	10
Figure 2.3	Schematic depiction of two identical atoms colliding with each other. As the de Broglie wavelength λ_{dB} is larger than the scattering length a , the two scattering events, (a) forward and (b) backward scattered events are indistinguishable.	16
Figure 2.4	Schematic demonstration of the spin rotation in a collision between two indistinguishable particles, using the Bloch sphere representation. The two Bloch spheres on the left represent two particles with slightly different transverse spin colliding with each other. As a result of the ISRE the spin of each particle rotates around the total spin during the collision.	25

Figure 3.1	<p>Trapping process in a 1D MOT. The atomic excited state is Zeeman-shifted in the magnetic field. The dashed line indicated on the diagram represents the energy of the incoming photon ($\hbar\nu$), detuned below the resonant transition. On the right side, the incident laser frequency is closer to the transition from the ground state to the $m = -1$ excited state, since the $m = -1$ state is shifted down due to the Zeeman shift. Therefore, the transition with $\Delta m = -1$ is closer to being resonant with the illuminating laser. As a result, the atoms on the right side scatter σ^- photons at a higher rate than the σ^+ photons. Choosing the correct polarization of the incident laser beams leads to driving the atoms towards the center of the trap.</p>	31
Figure 3.2	<p>Hyperfine structure of D_2 transition ($5^2S_{1/2} \rightarrow 5^2P_{3/2}$) of ^{87}Rb in zero magnetic field. The cooling transition ($F = 2 \rightarrow F' = 3$) and repumper transition ($F = 1 \rightarrow F' = 2$) are indicated on the diagram. The energy separations are not to scale.</p>	32
Figure 3.3	<p>Zeeman-shifted ^{87}Rb hyperfine splitting in magnetic field. It is noticeable that in low magnetic fields, the energy of $1, -1\rangle$ state increases with magnetic field.</p>	34
Figure 3.4	<p>Zeeman-shifted ground ($5S_{1/2}$) and excited ($5P_{3/2}$) states of ^{87}Rb in low magnetic field. The ARP ($1, -1\rangle \rightarrow 2, -2\rangle$) and imaging ($2, -2\rangle \rightarrow 3, -3\rangle$) transitions are shown on the diagram. The energy separations are not to scale.</p>	38
Figure 3.5	<p>Zeeman-shifted ground-state of ^{87}Rb in low magnetic field. The pseudo-spin $\frac{1}{2}$ system consists of two trapped states $1\rangle \equiv 1, -1\rangle$ and $2\rangle \equiv 2, 1\rangle$ coupled via a two-photon transition. The microwave fields are detuned from the $2, 0\rangle$ state to avoid populating the intermediate state.</p>	39

Figure 3.6	Schematic representation of the mutual compensation of the mean-field shift and Zeeman shift. The total differential potential is roughly uniform across the atomic distribution.	42
Figure 3.7	a) ω_0 is the resonant transition frequency between the two states $ 1\rangle \equiv 1, -1\rangle$ and $ 2\rangle \equiv 2, 1\rangle$ (Fig. 3.5) and $\omega_{2\nu}$ is the frequency of the applied two-photon pulses, with $\delta = \omega_{2\nu} - \omega_0$. b) Ramsey spectroscopy sequence.	44
Figure 3.8	Schematic representation of Ramsey oscillations in Bloch sphere representation. Two $\pi/2$ pulses are detuned by $\delta = \omega_{\mu\nu} - \omega_0$ and separated by time T. (a) When $\delta T = 0$ the two-pulse sequence is equivalent to a π pulse. (b) When $\delta T = \frac{\pi}{2}$ the second $\pi/2$ does not transfer the atoms as the state vector is along the field's torque vector (U - axis). (c) When $\delta T = \pi$ the second $\pi/2$ transfer the atoms back to the initial state.	45
Figure 3.9	Ramsey spectroscopy data showing an oscillation of the population of atoms in state $ 1\rangle$ measured after the second $\pi/2$ pulse in the center of the atomic distribution. The solid line is a fit to a sign wave as a guide to eye.	45
Figure 3.10	The Ramsey oscillation frequency as a function of axial position is shown. The differential energy shift between states $ 1\rangle$ and $ 2\rangle$ is extracted for different applied fields. (Red, \circ) shows uniform differential potential across the atomic distribution achieved in the mutual compensation scheme (red, \circ). Also are shown differential potential data with positive (black, \square) and negative (blue, \square) linear field gradients. Differential energy shifts are measured by Ramsey spectroscopy (Section 3.3.1).	46

Figure 3.11	Population of atoms in the two states $ 1\rangle$ ($N_1(z)$, ■) and $ 2\rangle$ ($N_1(z)$, ●). The population in each state is measured in separate experimental shots. The atomic cloud is divided into 21 axial bins for spatial resolution.	48
Figure 3.12	Ramsey oscillation data for a typical transverse spin component measurement. A sine wave with fixed frequency but time varying amplitude is fit to the data points in a window that encompasses more than one full Ramsey oscillation. This window is moved in time through each data set to extract the time evolution of the amplitude and phase of Ramsey oscillations. Maximum contrast is measured in a separate calibration Ramsey scan. Sample results of this analysis are shown in Fig. 4.6. The solid line here is a fit to a growing sine wave to guide the eye.	49
Figure 3.13	Optical setup used in producing the step optical potential schematically presented in Fig. 3.14(a). The collimated beam from the laser is expanded axially using a pair of cylindrical lenses. The dark mask is imaged on the atomic cloud by a single spherical lens.	50
Figure 3.14	Preparation of the two-domain spin structure. (a) Conceptual schematic of the off-resonant patterned laser beam. (b) Bloch sphere representation of the two-domain spin structure preparation sequence: Applying a microwave π -pulse to the atoms initially in $ 1\rangle$ while illuminating them with a masked laser transfers atoms in the unilluminated half of the distribution to $ 2\rangle$. Time goes from top to bottom. (c) Composite image of atoms in $ 1\rangle$ (right, purple) and $ 2\rangle$ (left, green) following the initialization sequence and radial expansion, destructively acquired on sequential experimental sequences.	51

Figure 3.15	(a) Population of atoms in the two states $ 1\rangle$ ($N_1(z)$, solid line) and $ 2\rangle$ ($N_2(z)$, dashed line) at $T = 650$ nK and $n_0 \simeq 2 \times 10^{13} \text{cm}^{-3}$. The population in each state is measured in separate experimental shots. The sum of population in the two states $N_{\text{total}}(z) = N_1 + N_2$ (\square), is fit to a Gaussian function to extract the Gaussian half-width ($w_z \simeq 180(4) \mu\text{m}$) of the atomic distribution. As described earlier the cloud is divided axially into 21 bins for spatial resolution; here each data point corresponds to one bin. This data is used to reconstruct the longitudinal spin component. (b) Longitudinal spin component extracted using Eq. 3.10. We fit a Gaussian-weighted hyperbolic tangent function $S_{\parallel}(z) = A \exp(-z^2/2w_z^2) \tanh(z/\ell)$ to the initial $S_{\parallel}(z)$ to extract the initial domain-wall width $\ell \simeq 74(7) \mu\text{m}$ for the presented initial spin profile data here.	52
Figure 3.16	The initial transverse spin profile phase extracted from high resolution transverse spin component measurements is shown in (a). (b) Schematic depiction of the magnitude and orientation of the initial transverse spin component across the domain-wall region.	54
Figure 3.17	The initial two-domain spin profile consists of two anti-parallel longitudinal spin domains separated by a helical domain-wall. The initial transverse spin component magnitude S_{\perp} is extracted from Ramsey fringe contrast. The total spin $N_{\text{total}} \simeq N_1 + N_2$ is also shown. Solid lines are fits to a Gaussian (S_{total}), and the same Gaussian multiplied by $\text{sech}(z/\ell)$ (S_{\perp}) and $\tanh(z/\ell)$ (S_{\parallel}). The gray shaded region shows the domain-wall.	55
Figure 4.1	(a) The two oppositely polarized spin clouds of the strongly interacting Fermi gas bounce off each other. (b) The total column density, showing a high density region at the interface between the two opposite spin states due to collisions.	58

Figure 4.2	Time evolution of the spin oscillations as a function of interaction strength. For strong interactions the spin wave dynamics is suppressed.	59
Figure 4.3	Schematic depiction of the experimental sequence used for spin diffusion studies in uniform magnetic fields.	63
Figure 4.4	Time evolution of the two-domain spin structure. (a) Longitudinal spin component, S_{\parallel} , evolution shows increased longitudinal spin domain lifetimes. (b) Typical population measurements of $ 1\rangle$ (solid line) and $ 2\rangle$ (dashed line) at $t = 1 \mu s$, used to extract the longitudinal spin projection. (c) Evolution of transverse spin component amplitude, $c(z, t)$. Initially the transverse spin component is confined in the center of the atomic distribution in a region of width $\sim 0.6 \times w_z$. The transverse spin magnitude calculated from Ramsey fringe contrast rapidly spreads toward the edges of the atomic cloud where initial transverse spin magnitude is small, covering a region of the size $\sim 1.4 w_z$ by 200 ms. Ramsey fringes at (d) the trap center and (e) edge of the atomic distribution as shown by arrows (d,e) respectively in (c).	64
Figure 4.5	The total ensemble transverse spin magnitude c_{tot} is shown as a function of time. c_{tot} is calculated by summing transverse spin magnitude for all the bins across the atomic cloud $c_{\text{tot}}(t) = \sum_{i=1}^n c_i(t)$, with $n =$ number of axial bins. At the initial stage of the dynamics $t < 100$ ms the total transverse spin increases rapidly, followed by a gradual decay. Beyond 300 ms sine fits are less reliable due to low signal-to-noise ratio and are not included.	65
Figure 4.6	(a) Dynamics of the transverse spin amplitude in uniform external magnetic field. (b) Dynamics of the transverse spin phase for regions denoted as (i),(ii) and (iii) in (a). The initial transverse spin phase across the atomic distribution stays unchanged during the relaxation of the two-domain spin profile.	67

Figure 4.7	Schematic depiction of the experimental sequence used for studying samples with different initial degrees of coherence in the domain-wall.	69
Figure 4.8	(a) Time evolution of S_{\parallel} for different initial domain-wall coherences, from top to bottom $c_{\text{init}} = S_{\perp}/S_{\perp}^{\text{max}} = 0.74, 0.51, 0.28$ respectively in the cloud center. (b) Dipole moment time evolution calculated from (a), with a representative decaying sinusoidal fit to (iii) $c_{\text{init}} = 0.28$. (c) Damping rate and (d) oscillation frequency of the dipole moment for different c_{init} . Error bars correspond to fit uncertainties for dipole moment oscillations and c_{init} measurements. The shaded band is the result of numerical simulations of Eq. 4.1.	70
Figure 4.9	(a) Time evolution of S_{\perp} for different domain-wall degrees of coherence, from top to bottom $c_{\text{init}} = 0.71, 0.51, 0.30$ respectively in the cloud center. (b) Time evolution of S_{\perp} in different spatial regions, denoted by the dotted lines (d-f) in (a-i). The dashed box indicates a change in sampling rate to measure both the fast initial rise of coherence and longer relaxation to equilibrium. (c) Time evolution of total ensemble coherence for c_{init} data shown in (a). c_{tot} for each data plot (i-iii) in (a) is calculated by summing transverse spin magnitude for all the bins across the atomic distribution for each time step.	72
Figure 4.10	Instability onset seen in the ratio of maximum ensemble coherence to initial coherence, $c_{\text{tot}}^{\text{max}}/c_{\text{tot}}^{\text{init}}$, from simulations of Eq. 4.1, plotted logarithmically to highlight instability threshold. We vary a and (a) T or (b) ℓ with other parameters set to conditions of Fig. 4.8(a-ii). Crosses represent the experimental conditions used in this work. . .	75
Figure 5.1	Schematic of the apparatus used to create linear gradients in the differential potential, showing the time averaged laser intensity profile applied on the atomic distribution.	85

Figure 5.2 U_{diff}/h for uniform (red), negative (blue) with $G \sim -121$ Hz/mm and positive (black) with $G \sim 110$ Hz/mm linear gradients across the atomic distribution. dashed (dotted) line shows a linear fit for the positive (negative) gradient. The linear fit is used to extract the linear gradient G across the atomic distribution. The solid line shows a linear fit for the uniform differential potential. U_{diff} is measured by Ramsey spectroscopy. 86

Figure 5.3 Experimental sequence for studying the effect of linear field gradients on diffusion of the two-domain spin structure, showing the timing and duration of all the different applied fields. Each sequence begins with the initial spin-state preparation into a two-domain anti-parallel longitudinal spin texture in $G \sim 0$. Following the initialization sequence in a uniform differential potential, the nonuniform U_{diff} laser pulse is applied to create linear field gradients $G \neq 0$ during the relaxation of the spin structure to its final equilibrium. After the evolution time, the longitudinal spin component is destructively measured. The experimental sequence is repeated for each value of the evolution time. The transverse spin component is measured using the Ramsey spectroscopy method. 87

Figure 5.4	<p>(a)-(c) Spatiotemporal evolution of the longitudinal spin component S_{\parallel} in negative $G \simeq -20$ Hz/mm (a), cancellation field $G \sim 0$ Hz/mm (b) and positive $G \simeq 24$ Hz/mm (c) linear effective magnetic field gradients. The initial longitudinal domains undergo dipole oscillation in $G \sim 0$ Hz/mm in (b). Propagation in an effective magnetic field with negative field gradient in (a) increases the longitudinal domain oscillation frequency and also leads to much faster relaxation of the longitudinal spin domains, while propagating in an effective magnetic field with a positive linear gradient in (c) increases the longitudinal spin domain lifetime noticeably, compared to the uniform magnetic field results in (b). (d) Dipole moment time evolution calculated for longitudinal domain oscillations in (a)-(c). The solid line shows a representative exponentially decaying sinusoidal fit for (a). Frequency f and damping rate Γ of the longitudinal domain oscillations are extracted from these fits.</p>	89
Figure 5.5	<p>(a) Dipole moment oscillation frequency f and (b) damping rate Γ for positive and negative linear field gradient G. Error bars correspond to fit uncertainties for dipole moment oscillations [Fig. 5.4(d)]. . . .</p>	90
Figure 5.6	<p>Time evolution of the transverse spin component S_{\perp} for linear magnetic field gradient $G \simeq 24$ Hz/mm (a-c) and $G \simeq -20$ Hz/mm (d-f). Spatially resolved time evolution of the transverse spin magnitude (a/d) and transverse spin phase in the domain-wall region (b/e) for positive/negative G respectively. Time evolution of the total ensemble coherence for $G \simeq 24$ Hz/mm (c) and $G \simeq -20$ Hz/mm (f). . . .</p>	93

Figure 5.7	(a) The stabilized longitudinal domains for positive linear gradient $G \simeq 24$ Hz/mm. (b) The spatiotemporal evolution of the transverse spin orientation ϕ for the domain-wall region marked with the dashed square in (a). (c) The time evolution of ϕ highlighted for two locations in the domain-wall marked with dotted lines (i) and (ii) in (b). The transverse spin orientation exhibits dipolar spin oscillations in the domain-wall region.	95
Figure 5.8	(a) The fast decaying longitudinal domains for negative linear gradient $G \simeq -20$ Hz/mm (b) The spatiotemporal evolution of the transverse spin orientation ϕ for the domain-wall region marked with the dashed square in (a). (c) The time evolution of ϕ highlighted for two locations in the domain-wall marked with dotted lines (i) and (ii) in (b). The transverse spin orientation becomes further out of phase with time across the domain-wall, in contrast to the dipolar spin oscillations observed for positive linear gradients in Fig 5.7(c).	96
Figure 5.9	The initial stage of the spatiotemporal dynamics of the transverse spin magnitude $c(z, t)$ for negative field gradient $G \sim -21$ Hz/mm (a) and uniform magnetic field $G \sim 0$ Hz/mm (b). (c) The time evolution of the total ensemble coherence c_{tot} for (a) and (b), showing the suppression of the initial rise in $c_{\text{tot}}(t)$ for $G < 0$ compared with $G \sim 0$ Hz/mm (solid/dashed line are a guide to eye).	97
Figure 5.10	$c_{\text{ratio}} = c_{\text{tot}}^{\text{max}}/c_{\text{tot}}^{\text{init}}$ decreases as linear field gradients G are applied.	98

Figure 5.11 Simulation results for longitudinal domain dynamics (a-b) and transverse spin phase (c-d) for the same positive field gradient G . The initial longitudinal domain orientation is reversed between (a-c) and (b-d), while the initial transverse spin helix is unchanged. The same external field gradient stabilizes the longitudinal domains for (a), while it leads to faster decay of the longitudinal spin domains in (b). The contrast in the time evolution of the transverse spin phase can be seen in (c) and (d). The transverse spin phase exhibits oscillations in (c), while it grows further out of phase for (d). 99

Figure 5.12 (a) Schematic representation of the two-domain spin structure. The spin vector is rotated across the domain-wall such that in the middle of the domain-wall the spin is purely transverse. (b) For this specific initial longitudinal domain orientation - positive linear gradient in the effective magnetic field - the ISRE-driven longitudinal spin currents are generated from the transverse domain-wall region towards the longitudinal domains of the same orientation. Due to this effect the total longitudinal current is decreased significantly. (c) For this specific initial longitudinal domain orientation - negative linear gradient in the effective magnetic field - the ISRE-driven longitudinal spin currents are generated from the transverse domain-wall region towards the longitudinal domains of the opposite orientation, which adds to the diffusive longitudinal spin currents from the domains. Due to this effect the longitudinal domains decay rapidly. Diffusive longitudinal spin currents from the longitudinal spin domains are not shown here. 100

Chapter 1

Introduction

The experimental realization of Bose-Einstein condensation (BEC) of a dilute gas in 1995 [1, 2] led to the Nobel prize for Eric A. Cornell, Carl E. Wieman and Wolfgang Ketterle in 2001. Although the BEC phase transition was theoretically predicted by Satyendra Nath Bose and Albert Einstein in the early 1900s, due to experimental challenges it took experimental physicists nearly a century to condense the first BEC of a trapped alkali-atom gas.

Since the ground-breaking experiments in 1995 [1, 2] many different atomic species have been successfully condensed. To date, condensation has been achieved in many bosonic alkali atomic species including ^{87}Rb [1], ^{85}Rb [3], ^7Li [4, 5], ^{23}Na [6], ^{39}K [7], ^{41}K [8], ^{133}Cs [9], as well as the rare-earth element Yb [10, 11, 12] and the alkaline earth elements ^{40}Ca [13] and Sr [14, 15, 16, 17]. Also, degenerate Fermi gases have been produced in ^{40}K [18], ^6Li [19], ^{87}Sr [20], ^{173}Yb [21], to name a few, and condensates of diatomic molecules of many of these atomic species have been achieved.

In addition to these significant scientific achievements demonstrating pure condensates of atoms, the wide range of experimental improvements made to reach condensation have opened up a whole new field of research in atomic physics. The advantages these trapped ultra-cold atomic systems possess make them ideal model systems to investigate physical problems in the quantum regime. These systems provide experimental physicists with a high degree of control over experimental parameters and interactions, as well as easy manipulation and imaging. Today the diversity of the experimental and theoretical studies using trapped ultra-cold bosonic and fermionic atom systems is huge, with research applications

in various fields of physics including precision measurements [22, 23, 24], quantum information [25, 26, 27], high energy-physics [28], condensed-matter physics [29, 30] and even cosmology [31].

The early studies in the years following the experimental realization of BECs mainly focused on exploring the equilibrium properties of ultra-cold gases, though in recent years there has been an increasing interest in using ultra-cold atomic systems to explore the less studied area of out-of-equilibrium physical phenomena. For example, in condensed-matter-physics understanding transport phenomena is crucial, but studying transport in strongly correlated systems and real materials is extremely difficult. In contrast, trapped ultra-cold atom systems indeed provide a clean and highly controllable environment to study transport and non-equilibrium phenomena. Thus, these quantum gases have been widely used as experimental quantum simulators for condensed-matter systems lately [30].

In recent years, there has also been great progress in experimental and theoretical studies of spinor Bose and Fermi gases realized in various ultra-cold trapped bosonic and fermionic atom systems. This field now covers a wide range of physical phenomena, including quantum magnetism [32, 33], non-equilibrium quantum spin dynamics and spin transport [34, 35, 36, 37], quench dynamics and the Kibble-Zurek mechanism [38, 39], spin waves [40, 41, 42] and topological defects [43].

A spinor gas is distinguished by an additional internal degree of freedom, its spin. Spinor systems realized in ultra-cold atomic systems allow fundamental studies on spin-dependent interactions, which are crucial in understanding the behaviour of many quantum systems. Also in a spinor system the collisional properties of the gas are affected by the spin orientation of atoms during collisions due to exchange interactions, which modifies the system's many-body Hamiltonian as well.

Studies on spinor gases can be realized in magnetically independent trapping potentials, such as dipole traps or optical lattices. More generally, any multi-component gas could behave as a spinor system; therefore, a pseudo-spinor can be provided by the internal hyperfine structure of many atoms allowing studies on spin-dependent interactions. There have been multiple studies exploring the high-spin systems realized in these trapped multi-component

ultra-cold gases, including spin waves in pseudo-spin 3/2 systems [42] and coherent spin oscillations in tunable effective spin 1/2 to 9/2 [44].

In this work, we study spin diffusion in a weakly interacting non-degenerate Bose gas, as a special case of quantum transport. Spin diffusion is the transport process that evens out any spatial inhomogeneity in spin density in a many-body system. The concept of spin diffusion on a phenomenological level was introduced in 1950s. However, quantum mechanical interactions can modify spin diffusion drastically, leading to significant deviations from classical behaviour.

Quantum mechanical modifications to spin transport manifest in various ways in ultra-cold atomic systems. Most transport studies focus on the behaviour of a strongly interacting Fermi gas close to unitarity, since it provides a perfect model system to study the less understood non-equilibrium dynamics of strongly interacting fermionic matter. Experiments in a one-dimensional degenerate Fermi gas showed reversal of spin currents [37]. A few other studies explore the quantum-limited spin diffusivity in the degenerate regime close to unitarity in degenerate Fermi [36] and Bose [35] gases. The experimental results show diffusion-like behaviour in one dimension but unexpected super-diffusion in two dimensional systems. Also, the Leggett-Rice effect [45, 46] was observed in a degenerate Fermi gas close to unitarity [47].

While most studies in the field focus on quantum Bose and Fermi gases whose thermal de Broglie wavelength is long compared to the interparticle spacing ($\lambda_{dB} \ll n^{-1/3}$), ultra-cold non-condensed atoms in the cold-collision regime indeed exhibit interesting behaviour as well and provide a platform to explore the cross-over between quantum and classical regimes in a controllable manner. A system is in the cold-collision regime if the thermal de Broglie wavelength is long compared to the interparticle interaction range ($\lambda_{dB} \gg a$). In this regime quantum coherence effects cannot be neglected and affect the behaviour of the system significantly. Therefore, although atomic gases in the cold-collision regime are non-degenerate, they do not behave classically due to quantum symmetry requirements during collisions between atoms.

One example is the spin-exchange interaction. The exchange interaction does not affect the dynamic properties of a Bose-condensed gas, since all the atoms in the condensate occupy the same motional state. However, in an ultra-cold non-condensed Bose gas the exchange interaction is strong and affects the spin dynamics of these non-degenerate gases significantly. The exchange symmetry in collisions between indistinguishable atoms of a non-condensed spinor gas leads to an exchange mean-field [48, 49] or equivalently a spin rotation of atoms participating in collisions [50, 51]. This exchange interaction leads to multiple interesting phenomena in an otherwise classical gas, including spin-state segregation [52, 53], spin waves in non-degenerate trapped Bose and Fermi gases [40, 41, 42], spin self-rephasing and enhanced coherence times in a weakly interacting Bose gas [54], Castaing’s instability [55, 56, 57] and localized collapse and revival of coherence in trapped ultra-cold gases [58].

Since degenerate ultra-cold gases are the main focus of interest in the field, the exchange interaction effects in the non-condensed regime in ultra-cold gas systems remain mostly unexplored. Despite this fact, there is a considerable amount of research on collective behaviour due to exchange interactions in non-degenerate dilute spin-polarized gases [59, 60, 61] due to spin rotations as a result of the identical spin rotation effect (ISRE) [48, 50].

Collective behaviour in degenerate Fermi liquids [62, 63, 64] occurs as a result of the Leggett-Rice rotation (LR) [45]. Similar effects in non-degenerate dilute spin-polarized gases are due to the ISRE interaction. ISRE interaction occurs during indistinguishable collisions of identical particles with different spins, and will be discussed in detail in Section 2.2.3. The connection between these two effects is examined in detail in Reference [46]. Although the two effects (ISRE and LR) result in similar collective behaviour, the two physical systems are very different and the physical origins of the observed effects are not the same. In degenerate Fermi liquids the spin rotation originates from a precession of a spin due to strong interactions with the background fluid. This interaction term is then added to the drift term of the kinetic equation as a so-called molecular field. However, the spin rotation effects in weakly interacting dilute non-degenerate gases originate from pure quantum symmetry requirements during collisions and emerge from the collision integral (see Chapter 2 for details).

In this work, we study the effect of exchange-interaction driven ISRE on the longitudinal diffusion dynamics of a two-domain pseudo-spin texture. This domain structure is prepared in a one-dimensional weakly interacting non-condensed trapped Bose gas. The organization of this thesis is as follows.

In Chapter 2, we describe the spin-1/2 system and give an overview of the spin dynamics theory. We derive a semiclassical Boltzmann equation to describe the dynamics of the non-condensed Bose gas and discuss the spin-exchange interaction and the nature of the ISRE term.

In the first part of Chapter 3, we summarize the experimental procedure used in preparing and measuring an ultra-cold Bose gas. In the second part, we describe the experimental methods used in this work to prepare spin textures and measure spin transport.

The experimental results of studying longitudinal spin diffusion in a weakly interacting non-condensed trapped Bose gas are presented in Chapter 4, along with numerical results studying the effect in a broader parameter space than available in our experiments. Also, we explore the effect of the degree of coherence in the system on the longitudinal diffusion dynamics in Chapter 4. Our results indeed manifest a significant deviation from classical behaviour, due to exchange interactions during collisions. We observe increased longitudinal domain lifetimes compared with classical lifetime predictions. The results also show sensitivity to the degree of coherence in the system, emphasizing further the quantum mechanical nature of the observed effects.

In Chapter 5 we explore the effect of introducing effective external magnetic fields with nonuniform profiles on the longitudinal spin diffusion dynamics. Our results show drastically different behaviour when positive and negative field gradients are introduced. For positive field gradients we observe even further stabilization of the longitudinal domains, while for negative field gradients the longitudinal domains rapidly relax to the final equilibrium state. We also observe a suppression of Castaing's instability when linear field gradients of both signs are applied. We present the experimental results along with a phenomenological discussion describing the observed effects.

In Chapter 6 we summarize the results and provide suggestions for possible future research projects to explore the spin transport phenomenon further.

Chapter 2

Spin dynamics theory

In this chapter a brief description of the theory of spin dynamics in ultra-cold non-condensed atomic gases is given. We start by describing a two-level system coupled to an electromagnetic field, which is analogous to a spin-1/2 system. Next, we present a brief discussion of the derivation of the spin transport equation for a dilute weakly interacting non-degenerate trapped gas relevant to the experiments conducted in this thesis, mainly focusing on the origins of the identical spin rotation term (ISRE) in the kinetic equation. The ISRE term does not play a role in the dynamics of a system in the classical or degenerate quantum regime. For a two-level BEC in the degenerate quantum regime phase separation occurs due to the mean-field energy differences, while in the classical regime the dynamics is described by the classical Boltzmann equation. As a special case of spin transport in the non-degenerate regime due the ISRE interactions, we discuss spin diffusion and the situation relevant to Castaing's instability. We also describe the effect of adding external effective magnetic field gradients to the diffusion dynamics of a two-domain spin structure.

2.1 A two-level system coupled to an electromagnetic field

A two-level system is conceptually the same physical object as a spin-1/2 doublet. The Hamiltonian of a two-level system (ground and excited state denoted by "g" and "e" respectively) coupled to an electromagnetic field is

$$H = \begin{pmatrix} \frac{\hbar\omega_0}{2} & \Omega_R e^{\frac{i\omega t}{2}} \\ \Omega_R e^{-\frac{i\omega t}{2}} & -\frac{\hbar\omega_0}{2} \end{pmatrix} \quad (2.1)$$

where Ω_R is the Rabi frequency, which indicates the coupling strength between the field and the atoms. ω is the frequency of the coupling field and ω_0 is the atomic resonance frequency of the two states.

Solving the time-dependent Schrödinger equation gives the probability of finding the atoms in the ground or excited state as a function of time. Starting with the system in the ground state ($P_g(0) = 1$ and $P_e(0) = 0$), the probability of finding the system in the excited state at time t is [65]

$$P_e(t) = \left(\frac{\Omega_R}{\Omega'_R}\right)^2 \sin^2\left(\frac{\Omega'_R t}{2}\right). \quad (2.2)$$

The effective Rabi frequency, Ω'_R , is

$$\Omega'_R = \sqrt{\Omega_R^2 + \delta^2}, \quad (2.3)$$

where $\delta = \omega - \omega_0$ is the detuning of the coupling field from the atomic resonant transition.

2.1.1 Bloch-sphere representation and optical resonance

The Bloch-sphere representation is a pictorial way of representing the Rabi problem, in which the system is described as a state vector $\vec{\psi}$ (Bloch vector) in a three-dimensional space (U, V, W) (Fig. 2.1). The vertical axis W represents S_{\parallel} , the longitudinal spin component and we denote its direction as \hat{e}_{\parallel} . The horizontal plane $(U - V)$ corresponds to \vec{S}_{\perp} , the transverse spin component, where the azimuthal angle ϕ indicates the relative superposition phase between the two states.

The interaction between a two-level system and an electromagnetic coupling field can be considered as a torque vector $\vec{\Omega}$ with components $(\Omega_R, 0, \delta)$ acting on the state vector of the system. In order to reach this simplification, a transformation to a frame rotating at the coupling field's frequency ω , and implementation of the rotating-wave approximation is needed [66]. The motion of the Bloch vector is described by

$$\frac{d\vec{\psi}}{dt} = \vec{\Omega} \times \vec{\psi}, \quad (2.4)$$

and is confined to the surface of a sphere (Fig. 2.1). Any decoherence in this picture is manifested as a decrease in the magnitude of the Bloch vector horizontal component.

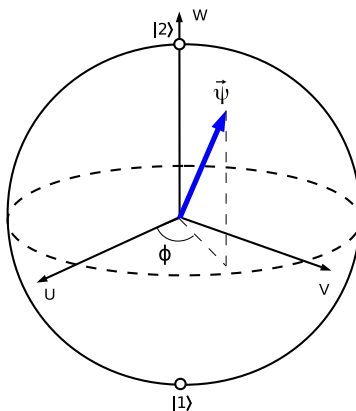


Figure 2.1: Bloch-sphere representation of the state vector $\vec{\psi}$ of a two-level system. The North pole corresponds to the excited state $|2\rangle$ and the South pole corresponds to the ground state $|1\rangle$. The azimuthal angle ϕ represents the relative phase of the superposition state.

When the electromagnetic coupling field is close to resonance, the field's torque vector lies close to the equator, and the Bloch vector $\vec{\psi}$ precesses around the field's torque vector $\vec{\Omega}$, oscillating between the two states [Fig. 2.2(a)]. When the field is detuned from the atomic resonance, the field's torque vector approaches one of the poles, depending on the sign of the detuning. In this case the Bloch vector $\vec{\psi}$ undergoes rapid precession with a small tipping angle about the torque vector, nearly staying in its initial state [Fig. 2.2(b)].

2.2 Description of the system and the dynamics

We study the dynamics of an ensemble of weakly interacting trapped identical atoms (bosons) with two internal levels. This system is similar to an ensemble of particles with spin-1/2 degree of freedom. A single trapped two-level atom is described by the Hamiltonian [67]

$$\hat{H} = \left[-\frac{\hbar^2}{2m} \nabla^2 + U_{\text{ext}}(r) \right] \hat{1} + \frac{\hbar}{2} \vec{\Omega} \cdot \vec{\sigma}. \quad (2.5)$$

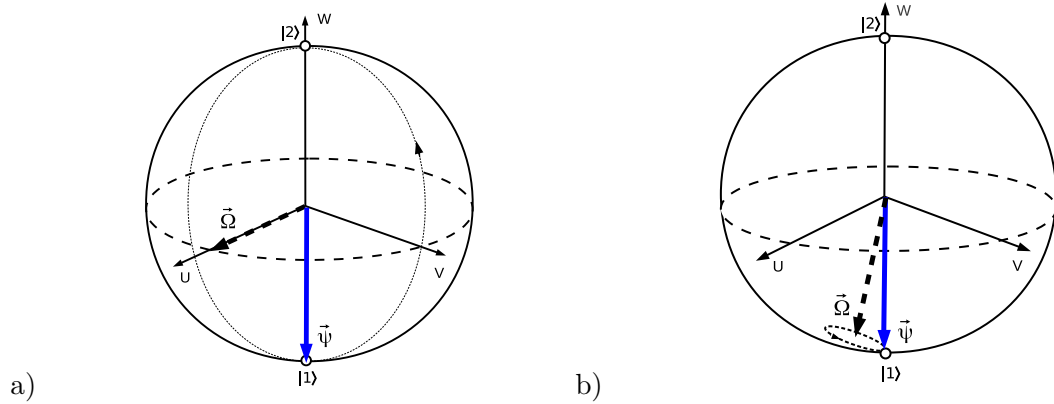


Figure 2.2: Bloch-sphere representation of Rabi flopping. The black dashed vector shows the coupling field torque vector $\vec{\Omega}$, the blue vector shows the state vector $\vec{\psi}$ and the dotted line shows the path of the oscillation of the Bloch vector. The coupling field is (a) in resonance with the atomic transition and (b) detuned from resonance.

The first term in Eq. 2.5 is the center of mass Hamiltonian including the kinetic energy and the external trapping potential terms and $\hat{1}$ is the unit 2×2 matrix. $U_{\text{ext}}(r) = \frac{m\omega_z^2}{2}[\alpha^2(x^2 + y^2) + z^2]$ is the axisymmetric harmonic trapping potential, with an aspect ratio of $\alpha = \omega_{\perp}/\omega_z$. The second term is the internal degree of freedom Hamiltonian, describing the interaction of the two-level system with the external coupling field $\vec{\Omega}(\mathbf{r})$; $\vec{\sigma}$ is the vector of Pauli matrices. In the absence of any external coupling field, $\Omega_u = \Omega_v = 0$ and in a rotating frame at Larmor frequency (ω_{hf}), $\Omega_w = \Delta(\mathbf{r})$ is a position dependent frequency splitting between the two spin states.

2.2.1 The spin transport equation

There are in general two different approaches to deriving the kinetic equation for a dilute gas of atoms with two internal states. One is the collisional method with a semiclassical treatment of Boltzmann's original derivation [68] initially used to describe transport in classical gases. In this approach collisions are considered as point processes between uncorrelated particles. Then one adds the effect of all such binary interactions at each point of space to derive the Boltzmann transport equation. This equation is a semiclassical kinetic equation, because although the particle moves along a straight line between collisions, the quantum properties are included in the scattering cross-section. This approach gives a more microscopic description of the process and one can see the origins of the extra terms

emerging in the collision integral due to the quantum properties and indistinguishability effects. In the following section, we will briefly discuss the use of this method to derive the transport equation for a trapped dilute gas relevant to our experiments.

The other method is a mean-field approach by considering the average effect of all the collisions as a pseudo-potential that modifies the drift term of the kinetic equation. A mean-field treatment of the dynamics might seem unreasonable for a dilute gas as the particles are freely moving between the collisions, but it turns out that the average over exchange interactions during all possible collisions at each point of space can be approximated by a so called “*exchange mean-field*”. In this approach one needs to insert a phenomenological collision integral term in the kinetic equation in the form of a relaxation time approximation. In [49] Fuchs *et al.* discuss the derivation of the kinetic equation using this method, showing the drift term in the transport equation is the same for the two different methods.

2.2.2 Collisional method for derivation of the transport equation

The general collisional method involves calculating the effect of all binary collisions on the single particle density operator of the system $\hat{\rho}_1$. The collisions are considered as point-like instantaneous processes between uncorrelated particles. Then one proceeds by writing an operational kinetic equation of the form

$$\frac{d\hat{\rho}_1}{dt} + \frac{1}{i\hbar} [\hat{\rho}_1, \hat{H}_1] \simeq \frac{d}{dt} |_{\text{coll}} \hat{\rho}_1, \quad (2.6)$$

with \hat{H}_1 the single particle Hamiltonian and the r.h.s. is the collision integral. The next step is to perform a Wigner transform [71] of Eq. 2.6 to derive the kinetic equation for $\hat{\rho}_W(r, p)$, the Wigner transform of $\hat{\rho}_1$. $\hat{\rho}_W(r, p)$ is the quantum mechanical analog of the single particle distribution in phase space, $f_1(r, p)$ in Boltzmann’s original method. Despite the fact that $\hat{\rho}_W(r, p)$ is not physically a probability distribution, it still can be used as a tool to derive the kinetic equation. This kinetic equation resembles the Boltzmann equation for the single particle distribution function in phase-space $f_1(r, p)$. The non-trivial parts of this derivation of the kinetic equation are finding a precise expression for the r.h.s of

Eq. 2.6, i.e. the calculation of the collision integral, as well as the calculation of the Wigner transform of the operators.

In the derivation of the transport equation for a system of indistinguishable particles with internal degrees of freedom (spin) some extra terms emerge due to quantum symmetrization properties during collisions. To show the origins of these extra terms emerging in the semiclassical transport equation as a result of the quantum indistinguishability effects, we start by describing the effect of binary collisions on the spin density operator discussed in References [50, 69] in a general derivation of the transport equation of a non-degenerate spin-polarized gas. In this method the Boltzmann collisional approach is used exploiting the S-matrix collision method. These extra terms vanish if one ignores the symmetrization (antisymmetrization for fermions) imposed by the symmetrization properties of wave functions (or Pauli principle) for indistinguishable atoms during spin-exchange collisions, emphasizing the purely quantum nature of these additional terms. Then we follow the derivation method used in Reference [49] to find the one-dimensional spin transport equation relevant to our experimental studies, which is also used in numerical calculations presented later in this thesis.

2.2.3 Effects of binary collisions on the spin density matrix

In this section we discuss the effect of binary collisions on the internal state of the colliding atoms. We start by presenting $\hat{\rho}_1$ the single particle spin density operator for a two-level (pseudo-spin 1/2) system. Then we proceed to describe the effect of a binary collision on $\hat{\rho}_1$ in the S-matrix representation considering the indistinguishability of the atoms participating in the collision. This leads us to obtain the extra terms emerging due to interference effects, one of which is the identical spin rotation term (ISRE). The ISRE term can be viewed as an extra effective Hamiltonian acting on the system. This effective Hamiltonian changes the internal state of the atoms during collisions, and for spin-1/2 can be described as a spin rotation due to an apparent effective magnetic field.

Single particle density operator

Here we consider two identical atoms possessing internal variables (spin) entering a collision. We want to study the general effect of the collision on their internal state density operator, due to the quantum indistinguishability effects during collisions. The spin state of each atom is described by a density operator $\hat{\rho}_1$ and $\hat{\rho}_2$, which in general are not equal. In the center of mass reference frame the density operator of the two-atom system before collision is given by

$$\hat{\rho}_{\text{init.}} = \int d^3k_i u(\mathbf{k}_i) \int d^3k'_i u^*(\mathbf{k}'_i) |1 : \mathbf{k}_i; 2 : -\mathbf{k}_i\rangle \langle 1 : \mathbf{k}'_i; 2 : -\mathbf{k}'_i| \otimes \hat{\rho}_1(1) \otimes \hat{\rho}_2(2), \quad (2.7)$$

which includes both external and internal (spin) degrees of freedom. $\hbar\mathbf{k}_i$ is the relative linear momentum of the two atoms, and $u(\mathbf{k}_i)$ in the interaction picture is a complex coefficient associated with a wave packet in the space of two-atom relative motion spanned by the kets $|1 : \mathbf{k}, 2 : -\mathbf{k}\rangle$. These kets are the two-atom external variable states containing the relative momentum of the two colliding particles.

For indistinguishable particles one needs to consider the symmetrization properties of the wave functions for bosons and fermions. Using the symmetrization operator, the density matrix of the system before collision is given by

$$\frac{1}{2} \left(\hat{1} + \epsilon \hat{P}_e \right) \hat{\rho}_{\text{init.}} \left(\hat{1} + \epsilon \hat{P}_e \right), \quad (2.8)$$

with \hat{P}_e the exchange operator and $\epsilon = +1(-1)$ for bosons (fermions).

We consider the unitary evolution operator \hat{S} in the interaction picture, which evolves the state of the system during the collision. We consider the interaction as spin-independent; therefore, \hat{S} acts only on the space of the external variable and does not affect $\hat{\rho}_1(1)$ and $\hat{\rho}_2(2)$. Then the density operator for the whole system after collision becomes

$$\frac{1}{2} \hat{S} \left(\hat{1} + \epsilon \hat{P}_e \right) \hat{\rho}_{\text{init.}} \left(\hat{1} + \epsilon \hat{P}_e \right) \hat{S}^\dagger, \quad (2.9)$$

which includes the symmetry properties imposed by the symmetrization postulate.

The single-particle density operator for atom 1 after collision ($\hat{\rho}'_1$) is then given by a partial trace of Eq. 2.9 over the external and spin variables of the collision partner (atom 2)

$$\hat{\rho}'_1 = \text{Tr}_2 \left[\frac{1}{2} \left(\hat{1} + \epsilon \hat{P}_e \right) \hat{S} \hat{\rho}_{\text{init.}} \hat{S}^\dagger \left(\hat{1} + \epsilon \hat{P}_e \right) \right], \quad (2.10)$$

where we used the fact that \hat{S} and \hat{P}_e are commuting operators. Before deriving the different terms of the final density operator $\hat{\rho}'_1$ by performing the partial trace, we note that \hat{P}_e appears in different terms of $\hat{\rho}'_1$. There is one term without \hat{P}_e , and one with two such operators. The main terms added due to the indistinguishability effects are the two containing only one \hat{P}_e , either on the right or the left side of $\hat{\rho}_{\text{init.}}$. These terms are due to the exchange interference effects for indistinguishable atoms, which will be discussed in more detail later in this chapter.

The matrix elements of the spin density operator of an atom after collision with velocity inside a solid angle Ω_f , $\hat{\rho}'(\Omega_f)$ are obtained by a partial trace operation on Eq. 2.9, as follows

$$\begin{aligned} \langle m | \hat{\rho}'(\Omega_f) | m' \rangle &= \int_{\Omega_f} d^3 k_f \sum_{m''} \langle 1 : \mathbf{k}_f; 2 : -\mathbf{k}_f | \langle 1 : m; 2 : m'' | \\ &\times \left(\hat{1} + \epsilon \hat{P}_e \right) \hat{S} \hat{\rho}_{\text{init.}} \hat{S}^\dagger \left(\hat{1} + \epsilon \hat{P}_e \right) \\ &\times | 1 : \mathbf{k}_f; 2 : -\mathbf{k}_f \rangle | 1 : m'; 2 : m'' \rangle. \end{aligned} \quad (2.11)$$

Since the scattering is not necessarily isotropic, the matrix element of the spin density operator is integrated over a final solid angle. In this equation $\{|m\rangle\}$ is any set of states forming an orthonormal basis in the space of internal variable (spin degree of freedom) and $\hat{\rho}_{\text{init.}}$ should be substituted from Eq. 2.7. The matrix elements of the evolution operator \hat{S} between the initial and final states are given by

$$\hat{S}(\mathbf{k}_f, \mathbf{k}_i) = \langle 1 : \mathbf{k}_f; 2 : -\mathbf{k}_f | \hat{S} | 1 : \mathbf{k}_i; 2 : -\mathbf{k}_i \rangle. \quad (2.12)$$

Considering all the information above we obtain

$$\begin{aligned}
\langle m|\hat{\rho}'(\Omega_f)|m'\rangle &= A(\Omega_f)\langle m|\hat{\rho}_1|m'\rangle + B(\Omega_f)\langle m|\hat{\rho}_2|m'\rangle \\
&+ \epsilon C(\Omega_f) \sum_{m''} \langle m''|\hat{\rho}_1|m'\rangle \langle m|\hat{\rho}_2|m''\rangle \\
&+ \epsilon C^*(\Omega_f) \sum_{m''} \langle m|\hat{\rho}_1|m''\rangle \langle m''|\hat{\rho}_2|m'\rangle,
\end{aligned} \tag{2.13}$$

with

$$\begin{aligned}
A(\Omega_f) &= \int_{\Omega_f} d^3 k_f \int d^3 k_i u(\mathbf{k}_i) \int d^3 k'_i u^*(\mathbf{k}'_i) S(\mathbf{k}_f, \mathbf{k}_i) S^*(\mathbf{k}_f, \mathbf{k}'_i), \\
C(\Omega_f) &= \int_{\Omega_f} d^3 k_f \int d^3 k_i u(\mathbf{k}_i) \int d^3 k'_i u^*(\mathbf{k}'_i) S(-\mathbf{k}_f, \mathbf{k}_i) S^*(\mathbf{k}_f, \mathbf{k}'_i).
\end{aligned} \tag{2.14}$$

Considering that $B(\Omega_f) = A(-\Omega_f)$, then in an operator form we can write Eq. 2.13 as

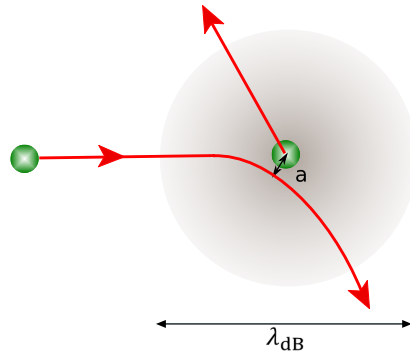
$$\rho_f(\Omega_f) = A(\Omega_f)\hat{\rho}_1 + A(-\Omega_f)\hat{\rho}_2 + \epsilon C(\Omega_f)\hat{\rho}_2\hat{\rho}_1 + \epsilon C^*(\Omega_f)\hat{\rho}_1\hat{\rho}_2. \tag{2.15}$$

The first two terms in Eq. 2.15 describe that for two distinguishable atoms, one can find either of them inside the solid angle Ω_f with the appropriate scattering probabilities. The last two terms on the r.h.s are due to interference effects between two different scattering processes for distinguishable particles (forward and backward scattering) presented in Fig. 2.3. These two terms (multiplied by ϵ) are due to the symmetrization requirements and are nonzero only when the two atoms are indistinguishable.

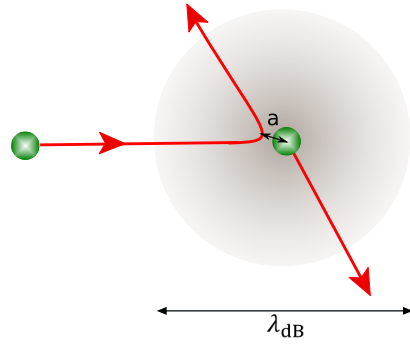
To find a more clear representation of Eq. 2.15, we can write the coefficient $C(\Omega_f)$ in terms of its real C_R and imaginary C_I parts. Then the last two terms in Eq. 2.15 can be rewritten as

$$\epsilon C_R(\Omega_f) \{\hat{\rho}_1, \hat{\rho}_2\} - i\epsilon C_I(\Omega_f) [\hat{\rho}_1, \hat{\rho}_2]. \tag{2.16}$$

In this equation $[\hat{\rho}_1, \hat{\rho}_2]$ ($\{\hat{\rho}_1, \hat{\rho}_2\}$) is the commutator (anticommutator) of $\hat{\rho}_1$ and $\hat{\rho}_2$. Since the trace of a commutator is always zero, only the real coefficient C_R affects the scattering



a)



b)

Figure 2.3: Schematic depiction of two identical atoms colliding with each other. As the de Broglie wavelength λ_{dB} is larger than the scattering length a , the two scattering events, (a) forward and (b) backward scattered events are indistinguishable.

amplitude. The coefficient C_I affects the internal state of the atoms (phase) during collisions. The second term in Eq. 2.16 is only nonzero when the two atomic density operators, $\hat{\rho}_1$ and $\hat{\rho}_2$, do not commute. Therefore the change of the spin due to this term is a pure coherence effect.

To present the origins of the coherent spin rotation term due to the indistinguishability of the atoms during collisions we kept the discussion very general up to this point. In principle the aforementioned coefficients (Eq. 2.14) have different contributions in various scattering amplitudes. To derive these terms one needs to calculate different matrix elements of the collision T matrix [70], since the evolution operator matrix elements $\hat{S}(\mathbf{k}_f, \mathbf{k}_i)$, are related to the collision T matrix by

$$\begin{aligned}\hat{S}(\mathbf{k}_f, \mathbf{k}_i) &= \langle 1 : \mathbf{k}_f; 2 : -\mathbf{k}_f | \hat{S} | 1 : \mathbf{k}_i; 2 : -\mathbf{k}_i \rangle \\ &= \delta(\mathbf{k}_f - \mathbf{k}_i) - i \frac{\pi m}{\hbar^2 k_i} \delta(k_f - k_i) T(\mathbf{k}_f, \mathbf{k}_i).\end{aligned}\tag{2.17}$$

The calculation of these different coefficients is complicated and beyond the scope of this thesis (see [49, 50] for details). We present the important conclusions of those calculations relevant to our work, mainly focusing on the low-energy limit where the collisions occur in the extreme quantum regime ($\lambda_{dB} \gg a$) and s-wave scattering is dominant. In this regime the T matrix is approximated by [49]

$$T(\hat{k}, \hat{k}') = -\frac{\hbar^2}{2\pi^2 m} f_k(\theta) = \frac{\hbar^2}{2\pi^2 m} (a - ika^2 + \dots).\tag{2.18}$$

In the low-energy limit ($ka \ll 1$) the contribution of all the terms due to the indistinguishability of the particles becomes negligible except for the ISRE in the forward direction (see References [49, 50] for details). This allows us to derive a simplified kinetic equation by including the effect of the spin rotation in the forward direction as a correction to the drift term, added as an internal effective magnetic field to the r.h.s of the kinetic equation. Next we present the derivation of this simplified version of the kinetic equation exploiting the collisional method following the approach discussed by Fuchs *et al.* [49].

2.2.4 Derivation of the quantum Boltzmann equation

In the previous section we discussed the effect of collisions of indistinguishable atoms on the spin state of the colliding atoms by calculating how the single particle spin density operator of an atom $\hat{\rho}_1$ evolves through a collision. To describe the dynamics of the system then one needs to solve the kinetic equation as presented in Eq. 2.6, by calculating how the density operator evolves in time. This derivation involves calculating the collision integral (the r.h.s. in Eq. 2.6). Following the same approach used in the previous section based on References [49, 50, 69], the rate of change of $\hat{\rho}_1$ is approximated by the variation $(\hat{\rho}'_1 - \hat{\rho}_1)/\Delta t$, for Δt much longer than the collision time

$$\frac{d}{dt}|_{\text{coll}}\hat{\rho}_1 \simeq \frac{1}{\Delta t}\hat{T}r_2 \left[\frac{1}{2}(\hat{1} + \epsilon\hat{P}_e)[\hat{S}\hat{\rho}_{\text{init.}}\hat{S}^\dagger - \hat{\rho}_{\text{init.}}](\hat{1} + \epsilon\hat{P}_e) \right], \quad (2.19)$$

with $\hat{\rho}_{\text{init.}}$ given in Eq. 2.7. The standard method to derive the transport equation for the ensemble of atoms involves performing a Wigner transform on both sides of the operational kinetic equation Eq. 2.6. The collision integral on the r.h.s. of Eq. 2.6 is then substituted with Eq. 2.19.

The Wigner transform of the l.h.s of Eq. 2.6 involves performing a Wigner transform of a product of operators, which can be done using Groenewold's formula [71, 72]. This method gives the result as an infinite series of a gradient expansion. Keeping up to the first order in the gradient expansion for \hat{U}_{ext} then the l.h.s of Eq. 2.6 can be approximated by

$$\partial_t \hat{\rho}_W(\mathbf{r}, \mathbf{p}) + \frac{\mathbf{p}}{m} \cdot \nabla_{\mathbf{r}} \hat{\rho}_W(\mathbf{r}, \mathbf{p}) + \frac{1}{i\hbar} [\hat{\rho}_W(\mathbf{r}, \mathbf{p}), \hat{U}_{\text{ext}}] - \frac{1}{2} \{ \nabla_{\mathbf{p}} \hat{\rho}_W(\mathbf{r}, \mathbf{p}), \cdot \nabla_{\mathbf{r}} \hat{U}_{\text{ext}} \}. \quad (2.20)$$

The anticommutator in this equation corresponds to the classical force term, which should be included in the kinetic equation. Therefore, in the Wigner transform of the r.h.s of the equation, a gradient expansion up to first order must be included.

The r.h.s of the kinetic equation is obtained by performing a Wigner transform on Eq. 2.19, including the gradient expansion terms up to first order. The low-energy limit of this calculation using the approximate T matrix of Eq. 2.18 leads to the kinetic equation

[49]

$$\begin{aligned} \partial_t \hat{\rho}_W(\mathbf{r}, \mathbf{p}) + \frac{\mathbf{p}}{m} \cdot \nabla_{\mathbf{r}} \hat{\rho}_W(\mathbf{r}, \mathbf{p}) + \frac{1}{i\hbar} \left[\hat{\rho}_W(\mathbf{r}, \mathbf{p}), \hat{U}_{\text{ext}} + \epsilon g \hat{n}(\mathbf{r}) \right] \\ - \frac{1}{2} \left\{ \nabla_{\mathbf{p}} \hat{\rho}_W(\mathbf{r}, \mathbf{p}), \cdot \nabla_{\mathbf{r}} (\hat{U}_{\text{ext}} + g \hat{n}(\mathbf{r}) \hat{1} + \epsilon g \hat{n}(\mathbf{r})) \right\} = I_{\text{coll}}[\hat{\rho}]. \end{aligned} \quad (2.21)$$

$g = 4\pi\hbar^2 a/m$ is the coupling constant and $\hat{n}(\mathbf{r})$ is the integrated density operator over momentum $\hat{n}(\mathbf{r}) = \int d^3p \hat{\rho}_W(\mathbf{r}, \mathbf{p})$. In this equation the forward scattering terms (linear in a) are included in the l.h.s of the kinetic equation, as a correction to the drift term due to the indistinguishability of particles, discussed in the previous section. In Eq. 2.21 the terms proportional to a^2 are included in $I_{\text{coll}}[\hat{\rho}]$, but since in the low-energy limit the ISRE term is the only dominant term, we can obtain a simplified collision integral by a relaxation time approximation instead.

Although in this model the collisions are spin independent, we can generalize this kinetic equation for a gas with spin-dependent interactions to describe the system thoroughly. This is done by a similar procedure as discussed for spin-independent interactions, only instead of Eq. 2.18 for the T matrix, a more complicated expression should be used in the calculation of the collision integral on the r.h.s of the kinetic equation. The final kinetic equation in this case is similar to Eq. 2.21 but with a more complicated expression for the mean-field term, such that the effective single-particle potential term \hat{U} should be replaced by

$$\hat{U} = \hat{U}_{\text{ext}} + \begin{pmatrix} (1 + \epsilon)g_{22}n_2 + g_{12}n_1 & \epsilon g_{12}n_{21} \\ \epsilon g_{12}n_{21} & (1 + \epsilon)g_{11}n_1 + g_{12}n_2 \end{pmatrix}. \quad (2.22)$$

$g_{\alpha\beta} = 4\pi\hbar^2 a_{\alpha\beta}/m$ is the coupling constant, with various scattering lengths $a_{\alpha\beta}$ depending on spin of colliding atoms. $n_i (i = 1, 2)$ is the local density of atoms in each state and n_{21} is the density of atoms in the superposition state. The resulting equation gives a general kinetic equation for a non-degenerate gas with spin-dependent interactions in the low-energy limit,

including the mean-field and external potential effects:

$$\begin{aligned} \partial_t \hat{\rho}_W(\mathbf{r}, \mathbf{p}) + \frac{\mathbf{p}}{m} \cdot \nabla_{\mathbf{r}} \hat{\rho}_W(\mathbf{r}, \mathbf{p}) + \frac{1}{i\hbar} [\hat{\rho}_W(\mathbf{r}, \mathbf{p}), \hat{U}(\mathbf{r})] \\ - \frac{1}{2} \{ \nabla_{\mathbf{p}} \hat{\rho}_W(\mathbf{r}, \mathbf{p}), \cdot \nabla_{\mathbf{r}} \hat{U}(\mathbf{r}) \} = I_{\text{coll}}[\hat{\rho}]. \end{aligned} \quad (2.23)$$

The second term on the l.h.s. is the usual free drift term and the anticommutator is the force term due to any gradients in the external potential and the mean-field. The commutator is a spin rotation term due to all of the contributing effective magnetic fields including the ISRE term. The approximations applied are that s-wave scattering is assumed to be dominant in low-energy collisions and the collision integral can be replaced by a simple relaxation time approximation.

One-dimensional quantum Boltzmann equation for spin density

Any 2×2 matrix (\hat{A}) can be decomposed into $\hat{A} = A_0 \hat{1} + \vec{A} \cdot \hat{\sigma}$, with $A_0 = \text{Tr}(\hat{A})$. Therefore, the Wigner distribution function $\hat{\rho}_W(\mathbf{r}, \mathbf{p})$ can be rewritten in the basis of the Pauli matrices $\hat{\sigma}$ and the unit 2×2 matrix

$$\hat{\rho}_W(\mathbf{r}, \mathbf{p}, t) = \frac{1}{2} \left(f(\mathbf{r}, \mathbf{p}, t) \hat{1} + \vec{M}(\mathbf{r}, \mathbf{p}, t) \cdot \hat{\sigma} \right). \quad (2.24)$$

Then in terms of the phase-space atomic density f and spin density \vec{M} the coupled Boltzmann equations are given by

$$\partial_t f + \frac{\mathbf{p}}{m} \cdot \nabla_{\mathbf{r}} f - \nabla_{\mathbf{r}} U_0 \cdot \nabla_{\mathbf{p}} f - \nabla_{\mathbf{r}} \vec{U} \cdot \nabla_{\mathbf{p}} \vec{M} = I_{\text{coll}}^{(f)}[f, \vec{M}] \quad (2.25)$$

and

$$\partial_t \vec{M} + \frac{\mathbf{p}}{m} \cdot \nabla_{\mathbf{r}} \vec{M} - \nabla_{\mathbf{r}} U_0 \cdot \nabla_{\mathbf{p}} \vec{M} - \nabla_{\mathbf{r}} \vec{U} \cdot \nabla_{\mathbf{p}} f - \frac{2\vec{U}}{\hbar} \times \vec{M} = I_{\text{coll}}^{(M)}[f, \vec{M}], \quad (2.26)$$

with \hat{U} also decomposed as $\hat{U} = \frac{1}{2} \left(U_0(\mathbf{r}, t) \hat{1} + \vec{U}(\mathbf{r}, t) \cdot \hat{\sigma} \right)$. The scalar component U_0 is the overall trapping potential plus the mean field energy. The vectorial component $\vec{U}(\mathbf{r}, t)$ is

given by

$$\vec{U}(\mathbf{r}, t) = \frac{\hbar \Omega(\mathbf{r}, t)}{2} \hat{e}_{\parallel} + \frac{\epsilon g_{12} \vec{m}}{2}, \quad (2.27)$$

with $\hbar\Omega(\mathbf{r}, t)$ the differential potential experienced by atoms in the two different states, which can be set to almost zero by canceling the contributions from the differential Zeeman and mean-field shifts in a mutual compensation scheme. $\vec{m}(\mathbf{r}, t)$ is the experimental observable spin, which is obtained by integrating spin density $\vec{M}(\mathbf{r}, \mathbf{p}, t)$ over all momentum, $\vec{m}(\mathbf{r}, t) = \int dp \vec{M}(\mathbf{r}, \mathbf{p}, t)/2\pi\hbar$.

Since the system is quasi one-dimensional (trap frequency ratio $\omega_{\perp}/\omega_z \simeq 40$), we can derive a one-dimensional transport equation along the axial dimension z to describe the dynamics of the experimental system. Since the radial frequency is the fastest experimental timescale and the radial equilibrium is reached quickly, integrating the full kinetic equation in Eq. 2.26 over radial coordinates gives the one-dimensional kinetic equation for $f(z, p_z, t)$ and $\vec{M}(z, p_z, t)$ [49]

$$\partial_t f + \frac{p_z}{m} \partial_z f - \partial_z U_0 \partial_{p_z} f - \partial_z \vec{U} \cdot \partial_{p_z} \vec{M} \simeq -(f - f^{eq})/\tau_{(f)} \quad (2.28)$$

and

$$\partial_t \vec{M} + \frac{p_z}{m} \partial_z \vec{M} - \partial_z U_0 \partial_{p_z} \vec{M} - \partial_z \vec{U} \partial_{p_z} f - \frac{2\vec{U}}{\hbar} \times \vec{M} \simeq -(\vec{M} - \vec{M}^{eq})/\tau_{(\vec{M})}. \quad (2.29)$$

The collision integral on the r.h.s. is also replaced by a simple relaxation time approximation with f^{eq} (\vec{M}^{eq}) the local equilibrium density (spin density) in phase space and τ the relaxation time. The confining energy is of the order of $k_B T \simeq 14 \text{ kHz} \times h$, which is much larger than the mean-field interaction $gn(0) \simeq 140 \text{ Hz} \times h$. Since the mean-field interaction energy is much smaller, U_0 can be approximated by the external confining potential $\frac{1}{2}m\omega_z^2 z^2$. \vec{U} acts as an effective magnetic field and is made of two terms. One contains all the contributions from external fields, and the other is the exchange ISRE term [49]

$$\vec{U}(z, t) = \frac{\hbar\Omega(z, t)}{2} \hat{e}_{\parallel} + \frac{\epsilon g_{12} \vec{m}(z, t)}{2}. \quad (2.30)$$

The coupling constant g is renormalized by a factor of 1/2 in the process of radial averaging [73]. $\hbar\Omega(z, t)$ is the total differential potential containing all the contributions from different origins and acts as an effective magnetic field for the pseudo-spin system. $\vec{m}(z, t)$ is the total spin, which is obtained by integrating spin density $\vec{M}(z, p, t)$ over all momentum. Also, the force terms $\partial_z \vec{U} \partial_p f$ and $\partial_z \vec{U} \partial_p \vec{M}$ can be neglected since the differential trapping energy is usually set to a negligible value by canceling the effects of the mean-field shift and Zeeman shift in a mutual compensation scheme as will be discussed in Section 3.2.1. Even if the differential potential is not mutually canceled, the force term due to spatial gradients in the differential potential is small and the effects observed during the experiments presented in this thesis are not due to differential mechanical force terms.

For a non-degenerate and weakly interacting gas, the atomic Gaussian profile does not vary in time when the external forces (excluding the trapping force) are negligible. The initial equilibrium Maxwell-Boltzmann atomic phase-space density $f(z, p_z)$ is assumed to be stationary and solves the kinetic equation Eq. 2.28. Therefore, the dynamics can be described solely by the kinetic equation for $\vec{M}(z, p_z, t)$. Considering all these specific simplifying conditions, the final one-dimensional quantum Boltzmann equation for the spin density $\vec{M}(z, p_z, t)$ is

$$\partial_t \vec{M} + \frac{p}{m} \partial_z \vec{M} - m\omega_z^2 z \partial_p \vec{M} - \frac{1}{\hbar} (U_{\text{diff}} \hat{e}_{\parallel} + g' \vec{m}) \times \vec{M} \simeq - (\vec{M} - \vec{M}^{eq}) / \tau_{cl}, \quad (2.31)$$

where U_{diff} is the total differential potential experienced by atoms in the two different states and g' is the modified coupling constant, which is renormalized by 1/2 in the process of radial averaging. τ_{cl} is the radially averaged mean collision time $\tau_{cl}(z) = [16a^2 n_0(z) \sqrt{\pi k_B T / m}]^{-1}$ [67].

2.3 Effect of collective behaviour on spin diffusion in a trapped ^{87}Rb gas

The theoretical discussion of the first part of this chapter is very general and can be applied to various systems of fermionic or bosonic nature. In this section we focus on the specifics of our experimental system and discuss the phenomenon studied in this thesis

project. We study the diffusion of a two-domain spin structure in a weakly interacting gas of trapped atoms. Although the system is non-degenerate, it is far from a classical system and we expect to see quantum mechanical modifications to the dynamics.

The thermal de Broglie wavelength λ_{dB} of particles with mass m at temperature T is given by $\lambda_{dB} = (2\pi\hbar^2/mk_B T)^{1/2}$, where \hbar is the Planck constant and k_B is the Boltzmann constant. When this wavelength is negligible compared to other length scales in a system, quantum effects can be neglected. For ^{87}Rb atoms at $T = 600$ nK the thermal de Broglie wavelength is $\lambda_{dB} \simeq 240$ nm, which is much larger than the s-wave scattering length $a = 5.3$ nm and the collisions occur deep in the quantum regime. Therefore, the discussions of the previous section are applicable to our experimental system, and we expect to observe quantum modifications to the diffusion dynamics of the two-domain spin structure due to the indistinguishability of atoms during collisions. For collisions in the classical regime, considering $\lambda_{dB} \sim a$ (or equivalently $\mu < 1$) results in much higher temperatures ($T \sim 10\mu\text{K}$), which are not explored in this work.

Collective behaviour due to exchange interactions in degenerate Fermi liquids [45] has been known for many years. This collective behaviour is due to the strong interactions between a spin and the liquid background, which leads to spin oscillations [62, 63, 64]. It came as a surprise when twenty years later it was proposed that collective behaviour could also exist in nondegenerate dilute spin-polarized gases. This behaviour is due to spin-exchange driven ISRE [48, 50] as described in the first part of this chapter, and was observed as unexpected nuclear magnetic resonance signals in multiple experiments in dilute spin-polarized gas systems [59, 60, 61].

Collective behaviour due to the exchange degeneracy effects during collisions in non-condensed two-component trapped atomic gases was first observed by Lewandowski *et al.* [52], where the two components of a trapped ^{87}Rb gas sample were segregated spatially. The observed spatial separation of the gas into two components could not be explained by thermal energy considerations. This phenomenon was described [67, 73, 74, 75] as spatiotemporal pseudo-spin oscillations (spin waves) arising from the spin rotation effect, ISRE [50], which occurs in collisions between indistinguishable atoms in the quantum regime (see

Section 2.2.3). This observation renewed the interest in spin-wave studies in dilute non-degenerate quantum gases in trapped ultra-cold atoms.

Later, Kuklov and Meyerovich proposed that this analogy is richer in nature and predicted that other phenomena observed in the dynamics of spin-polarized gases can be observed in trapped ultra-cold atomic systems [56]. Fuchs *et al.* [55] numerically studied the presence of an instability in the longitudinal diffusion dynamics of a similar system (the so-called Castaing’s instability), using system parameters similar to the experiment described in [52]. Ragan theoretically studied the formation of longitudinal spin domains in such systems in inhomogeneous effective magnetic fields [76].

2.3.1 Spin diffusion

Particle indistinguishability during collisions affects spin diffusion significantly, making the classically simple spin diffusion dynamics anisotropic and highly nonlinear due to quantum modifications. Spin diffusion at low temperatures becomes dominated by the identical spin rotation effect and instead of being a purely dissipative process, it acquires an oscillatory character [77].

Coherent spin oscillations due to the ISRE in non-degenerate gases are usually studied in the hydrodynamic regime. The collision regime is characterized by comparing the mean free path l_{MF} with a relevant characteristic length scale in a system l . In the hydrodynamic regime ($l_{MF} \ll l$), the system does not deviate far from local equilibrium. In this regime, the transverse spin diffusion acquires an oscillatory character and the coherent spin interactions decrease the diffusion of transverse spin by canceling out inhomogeneities in the transverse spin. These effects lead to smaller diffusion coefficients for transverse spin diffusion [50]. In this regime the longitudinal spin diffusion remains a purely dissipative process. All the coherent interactions vanish from the longitudinal spin diffusion equations, since longitudinal spin components are distinguishable and the ISRE does not occur. Therefore, the spin diffusion dynamics becomes anisotropic with respect to transverse and longitudinal diffusion. Longitudinal and transverse here refer to directions in spin space and are described in Section 2.1.1.

But in the intermediate regime between the limits of hydrodynamic and collisionless ($l_{MF} \gg l$), the coherent spin rotation due to the ISRE actually produces a longitudinal component (Fig. 2.4), leading to the so-called longitudinal spin waves [67, 75, 74]. Although indistinguishability effects are still absent from the longitudinal spin interactions directly, and purely longitudinal spin oscillations are not affected by the ISRE interactions, the transverse spin interactions indirectly affect the longitudinal spin diffusion. Therefore, to describe the behaviour of the diffusion in our experiments thoroughly we need to consider the full kinetic equation in phase-space (Eq. 2.31). The experimental and numerical results discussed in this thesis show that coherent spin interactions indeed affect the longitudinal spin diffusion significantly. (see Chapters 4,5)

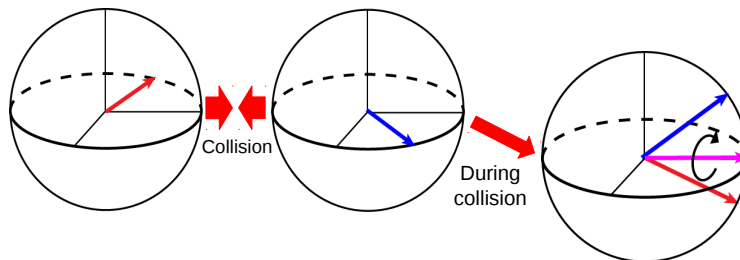


Figure 2.4: Schematic demonstration of the spin rotation in a collision between two indistinguishable particles, using the Bloch sphere representation. The two Bloch spheres on the left represent two particles with slightly different transverse spin colliding with each other. As a result of the ISRE the spin of each particle rotates around the total spin during the collision.

2.3.2 Spin waves and Castaing's instability

The spin transport equation Eq. 2.31 for a dilute non-degenerate gas in the hydrodynamic limit close to local equilibrium reduces to equations equivalent to Leggett equations

for degenerate Fermi liquids [45], which describe small amplitude transverse spin waves in these systems. These equations for a dilute non-degenerate gas are written as [55, 77]

$$\begin{aligned} \partial_t \vec{m} + \partial_z \vec{j} &= \vec{\Omega} \times \vec{m} \\ \partial_t \vec{j} - \left(\Omega \hat{e}_{\parallel} + \frac{g\vec{m}}{2\hbar} \right) \times \vec{j} + \frac{k_B T}{m} \partial_z \vec{m} + \omega_z^2 z \vec{m} &\simeq -\frac{\vec{j}}{\tau}, \end{aligned} \quad (2.32)$$

with $\vec{j}(z, t) = \int dp \frac{p}{m} \vec{M}(z, p, t)$, the spin current along z . These equations only contain position variables, and the momentum dependence vanishes. Our experimental system lies in the intermediate regime between the hydrodynamic and collisionless, and the spin oscillations have large amplitude. Despite the fact that the hydrodynamic approximation does not thoroughly describe the behaviour, we present analytical calculations in the hydrodynamic limit in this section to describe phenomena observed during experiments.

Quantitative studies in the hydrodynamic limit in zero effective external magnetic fields, *i.e.* $\Omega = 0$ in Eq. 2.32 or $U_{\text{diff}} = 0$, demonstrate that in a system with a homogeneous longitudinal spin distribution, m_{\parallel}^0 , a smoothly varying transverse inhomogeneity $\delta \vec{m}_{\perp}$, *i.e.* $\vec{m} = m_{\parallel}^0 \hat{e}_{\parallel} + \delta \vec{m}_{\perp}$, leads to generation of spin waves with spectrum [56]

$$\omega = \frac{Dk^2}{1 + \mu^2 m_{\parallel}^0{}^2} (i - \mu m_{\parallel}^0). \quad (2.33)$$

$D = k_B T \tau_{el} / m$ is the spin diffusion coefficient, with τ_{el} the collisional spin relaxation time. $\mu = \omega_{\text{exch}} \tau = gn\tau / \hbar$ is the ISRE spin rotation parameter, with density n and coupling constant g . In his studies on spin-polarized gases [78] Castaing showed that when a small transverse spin inhomogeneity of the form $\delta \vec{m}_{\perp} e^{i(kz - \omega t)}$ is added to a purely longitudinal spin distribution with a non-equilibrium longitudinal gradient ($\nabla m_{\parallel} \neq 0$), an instability in the transverse spin component occurs. This instability is due to an additional term in the imaginary part of the transverse spin-wave dispersion relation [56]

$$\text{Im}(\omega) = \frac{D}{1 + \mu^2 m_{\parallel}^0{}^2} \left(k^2 - 2\mu \vec{k} \cdot \vec{\nabla} m_{\parallel}^0 \frac{\mu^2 m_{\parallel}^0{}^2}{1 + \mu^2 m_{\parallel}^0{}^2} \right). \quad (2.34)$$

In Eq. 2.34, for wave vectors satisfying

$$k^2 < 2\mu\vec{k} \cdot \vec{\nabla}m_{\parallel}^0 \frac{\mu^2 m_{\parallel}^0{}^2}{1 + \mu^2 m_{\parallel}^0{}^2}, \quad (2.35)$$

the imaginary part of the dispersion relation has a negative sign. This negative term results in an exponential rise in the magnitude of the initial transverse perturbation ($\delta\vec{m}_{\perp}$), creating an instability in the transverse spin channel. This instability is referred to as Castaing's instability after him.

In a trapped atomic system the wave vectors k are bounded by the presence of the trap, as the size of a system L constrains the allowed wave vectors, imposing $k > \pi/L$. For $\mu m_{\parallel}^0 > 1$ this sets the observability criterion of Castaing's instability as

$$2\mu\nabla m_{\parallel}^0 > \frac{2\pi}{L}. \quad (2.36)$$

The spin rotation parameter in our system is $\mu \sim 3$, and we are capable of creating longitudinal spin gradients with a length scale of $\ell = l_{\nabla m_{\parallel}} \simeq 0.4 w_z$ (see Section 2.4), where w_z is the Gaussian half-width of the trapped atomic cloud along the axial direction (*i.e.* $L = 2w_z$). It is clear that these parameters, *i.e.* $\nabla m_{\parallel}^0 = 1/\ell$ and $\mu \sim 3$, are consistent with the instability criterion (Eq. 2.36); therefore, it is conceivable that Castaing's instability occurs in the longitudinal spin diffusion experiments studied in this thesis. However, we should emphasize that the signature of Castaing's instability in our results cannot be unambiguously distinguished from other dynamical processes observed.

In Chapter 4 of this thesis, the experimental results of the longitudinal spin diffusion studies in uniform external effective magnetic fields are presented, along with the results of the numerical solution of the one-dimensional transport equation (Eq. 2.31). We study the signature of the presence of Castaing's instability in spin diffusion experiments, which appears as an initial rise in the total transverse spin magnitude across the atomic distribution.

2.3.3 Spin diffusion in effective magnetic field gradients

Effective magnetic field gradients also affect the longitudinal spin diffusion dynamics significantly. The spin-torque term in the transport equation (Eq. 2.31), $(U_{\text{diff}} \hat{e}_{\parallel} + g\vec{m}) \times \vec{M}$, contains two terms. The first term in the parenthesis is any effective magnetic field applied to the system, and the second is the ISRE spin rotation term due to indistinguishability effects during binary collisions discussed in the first part of this chapter. When effective magnetic field gradients exist, the effect of the apparent ISRE magnetic field ($g\vec{m}$) and the effective nonuniform external magnetic fields (U_{diff}) can either cooperate or compete. The overall behaviour of the system depends on the relative strength of these contributing pieces as well as whether the effects cooperate or compete.

Experimental and theoretical studies in spin-polarized gases showed that the presence of effective magnetic field gradients can stabilize the longitudinal spin current even if Castaing's criterion is met [79, 80, 81, 82]. Ragan predicted that the effect of the linear field gradient in stabilizing the longitudinal spin diffusion is asymmetric with respect to the sign of the applied field gradient [81], and the stability diagram is drastically different between positive and negative linear field gradients. The reason for this striking difference is due to the fact that the initial longitudinal spin domain orientation breaks the symmetry of the system by introducing a specific direction. Then for one orientation of the effective magnetic field gradient with respect to the initial longitudinal domain profile orientation, the effect of the ISRE and the external field gradient cooperate, while for the other orientation they compete.

Conversely, magnetic field gradients can lead to formation of stable longitudinal spin domains in spin-polarized systems [82]. In the hydrodynamic regime, Ragan *et al.* [76] theoretically studied the formation of stable longitudinal spin domains in a trapped gas when linear effective magnetic field gradients G exist, considering $U_{\text{diff}}/\hbar = Gz$. They obtained an expression showing the relation between the width of the stable domain-wall ℓ_{eq} and the applied field gradient G [83]

$$G = \frac{1}{\mu M} \frac{\omega_z}{w_z} \left(\frac{\pi/2}{1.1\ell_{eq}/w_z} \right)^3 \omega_z \tau, \quad (2.37)$$

with w_z the Gaussian half-width of the atomic distribution. This stable domain state then slowly relaxes to the final equilibrium. For uniform external effective magnetic fields, $G = 0$, the longitudinal domain state becomes unstable with respect to transverse perturbation as described by Castaing's instability [56, 55].

We study the effect of nonuniform effective magnetic fields on longitudinal diffusion of the two-domain spin structure by applying positive and negative external effective magnetic fields with linear symmetry. The results of these studies are presented in Chapter 5, along with the results from the numerical simulation of the spin transport equation (Eq. 2.31), containing linear magnetic field gradients. We indeed observe the stabilizing effect of the linear field gradients in the initial stage of the dynamics, as the signature of Castaing's instability is suppressed when field gradients of both signs are applied. We also observe a drastic contrast between the longitudinal spin diffusion timescales for positive and negative linear field gradients. While for positive field gradients we observe slower longitudinal relaxation and longer longitudinal spin domain lifetimes, adding negative field gradients leads to a rapid relaxation of the longitudinal spin domains.

Chapter 3

Experimental setup

This chapter gives an overview of the experimental setup and methods used in studying spin transport in a non-condensed trapped gas of ^{87}Rb atoms. We worked with a Bose-Einstein condensation (BEC) system, but for these experiments, we studied non-degenerate samples rather than condensates. In the first part of this chapter, we give a brief overview of our BEC system and describe the procedure used to prepare and detect ultra-cold atomic samples. In the second part, we focus on the spin-state preparation and measurement techniques used in studying spin transport in this thesis project.

3.1 BEC system and ultra-cold atom preparation

Various sorts of trapping and cooling techniques are used to create Bose-Einstein condensates of different atomic species. Our apparatus is designed based on the work of H.J. Lewandowski *et al.*, which was an attempt to create a simplified BEC machine designed to "*consistently produce a stable condensate even when it is not well optimized*" [84]. The specifics of this system are explained in great detail in [57, 85] and will be summarized only briefly here.

To prepare an ultra-cold trapped atomic sample, first we trap and cool ^{87}Rb atoms in a magneto-optical trap (MOT). Trapping in a MOT exploits a combination of laser cooling and inhomogeneous magnetic fields to cool and confine neutral atoms in three dimensions. Three pairs of counter-propagating laser beams tuned below an atomic transition (cooling transition) cool the atoms down to μK temperatures, and the magnetic field provides the position-dependent trapping force to confine the atoms (Fig. 3.1). The density of trapped

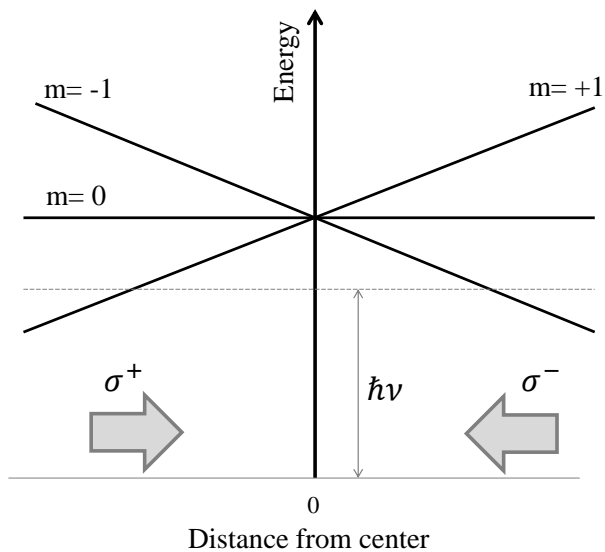


Figure 3.1: Trapping process in a 1D MOT. The atomic excited state is Zeeman-shifted in the magnetic field. The dashed line indicated on the diagram represents the energy of the incoming photon ($\hbar\nu$), detuned below the resonant transition. On the right side, the incident laser frequency is closer to the transition from the ground state to the $m = -1$ excited state, since the $m = -1$ state is shifted down due to the Zeeman shift. Therefore, the transition with $\Delta m = -1$ is closer to being resonant with the illuminating laser. As a result, the atoms on the right side scatter σ^- photons at a higher rate than the σ^+ photons. Choosing the correct polarization of the incident laser beams leads to driving the atoms towards the center of the trap.

atoms in a MOT is limited by reabsorption of spontaneously emitted photons from trapped atoms. Due to this process the density of trapped atoms in a MOT is limited to $\sim 10^{11}$ cm^{-3} .

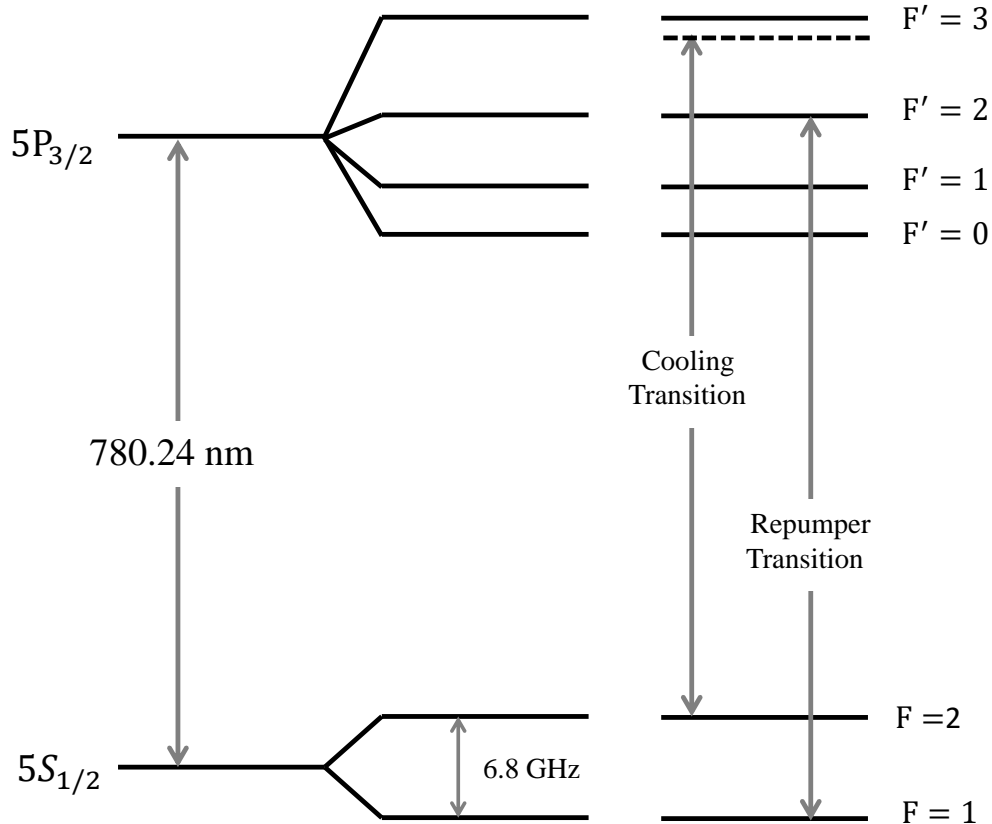


Figure 3.2: Hyperfine structure of D_2 transition ($5^2S_{1/2} \rightarrow 5^2P_{3/2}$) of ^{87}Rb in zero magnetic field. The cooling transition ($F = 2 \rightarrow F' = 3$) and repumper transition ($F = 1 \rightarrow F' = 2$) are indicated on the diagram. The energy separations are not to scale [86].

Figure 3.2 shows the hyperfine structure of the D_2 transition ($5^2S_{1/2} \rightarrow 5^2P_{3/2}$) of ^{87}Rb in zero magnetic field [86]. We tune the trapping laser for the MOT (cooling laser) to the $F = 2 \rightarrow F' = 3$ transition, where prime notation refers to an excited state. Due to off-resonant transitions some atoms are excited to the $F' = 2$ hyperfine sublevel, and decay from the $F' = 2$ to the $F = 1$ hyperfine level. Since $F = 1$ is not in the trapping cycle, a different laser (repumper laser) tuned to the $F = 1 \rightarrow F' = 2$ transition is used to force the atoms back into the cooling cycle. We use two different methods to lock lasers to desired transitions. We use the saturated absorption spectroscopy (SAS) method to lock the MOT

beams. A phase-locked loop (PLL) setup is used to lock the probe laser used for imaging the atoms and also the "Stark shift laser" used in preparing spin states and driving spin dynamics. See [57] for details of both techniques.

The atoms cooled down to micro-Kelvin temperatures are then transferred mechanically from the MOT to an ultra-high vacuum (UHV) science cell where the atoms are confined in the harmonic potential of a hybrid Ioffe-Pritchard magnetic trap (HIP trap). In the science cell, the atoms are then cooled further down into the quantum regime by means of rf-induced evaporative cooling. To trap the atoms in the HIP trap, we load the atoms into a magnetically trappable hyperfine state. These are the states whose energies increase as the magnetic field is increased. The magnetically trappable hyperfine states for the ground-state of ^{87}Rb in low magnetic fields are $|1, -1\rangle$, $|2, 1\rangle$ and $|2, 2\rangle$ (Fig. 3.3). We turn off the repumper light to pump the atoms into the $F=1$ state. The atoms in the $|1, -1\rangle$ sublevel will be trapped in the HIP trap after being transferred to the science cell.

The magnetic trap used in our experimental setup is slightly different than a standard Ioffe-Pritchard trap [87]. Our trap consists of a pair of permanent magnets and four electromagnetic coils. This trap is referred to as a hybrid Ioffe-Pritchard (HIP) trap. In this configuration instead of Ioffe bars, the permanent magnets provide radial confinement without any power consumption. They produce a strong radial quadrupole field in the center of the trap. The axial confinement is produced by two pairs of electromagnetic coils (I-P coils). There are two pinch coils (outer pair) that produce axial curvature. Two bias coils (inner pair) in a Helmholtz configuration produce a uniform magnetic field in the center of the trap. The magnitude of the resulting magnetic field is

$$|\vec{B}(\rho, z)| \approx \sqrt{(\eta\rho)^2 + \left(B_0 + \frac{\beta}{2}z^2\right)^2}, \quad (3.1)$$

where η is the radial field gradient produced by the permanent magnets (ρ is the radial coordinate), and β is the axial curvature produced by the pinch coils (z is the axial coordinate). $B_0 \sim 3.2$ G is the bias magnetic field. The magnetic trapping potential near the

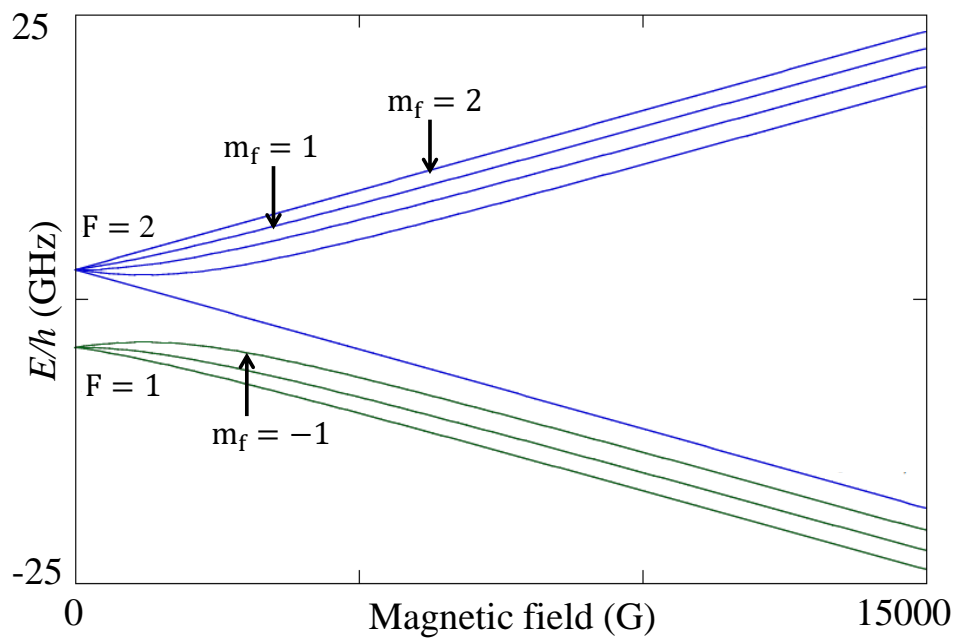


Figure 3.3: Zeeman-shifted ^{87}Rb hyperfine splitting in magnetic field. It is noticeable that in low magnetic fields, the energy of $|1, -1\rangle$ state increases with magnetic field.

center of the trap can be approximated as an anisotropic harmonic potential [87]

$$U \approx \frac{1}{2}m(\omega_r\rho^2 + \omega_z z^2). \quad (3.2)$$

The radial frequency ω_r and axial frequency ω_z are

$$\omega_r = \sqrt{\frac{m_f g_f \mu_B}{m B_0}} \eta \quad (3.3)$$

and

$$\omega_z = \sqrt{\frac{m_f g_f \mu_B \beta}{m}}. \quad (3.4)$$

g_f is the Lande g-factor, μ_B is the Bohr magneton and m is the mass of Rb atoms. In our experiment the trap frequencies are $\omega_z = 6.7$ Hz and $\omega_r = 255$ Hz. The trapped atomic cloud has an ellipsoidal geometry that is highly elongated along the axial direction with typical sizes of $10 \times 10 \times 380$ μm .

The next step in preparing a trapped ultra-cold atomic sample is to cool the trapped atoms into the quantum regime. We use rf-induced evaporative cooling to cool the atoms confined in the HIP trap close to or into quantum degeneracy. The principle of evaporative cooling is to remove atoms with higher energies than the average energy of the atomic sample and allow the sample to rethermalize through elastic collisions to a lower temperature [65].

In our experiment we use transitions to untrapped Zeeman-shifted levels to remove atoms from the trap. Atoms with lower energies are on average closer to the center of the trap and have smaller Zeeman shifts. The high energy atoms mostly reside in the regions with higher magnetic field values farther from the center of the trap, where the Zeeman-shift is larger. By applying rf radiation tuned to transitions from the trapped $|1, -1\rangle$ to the untrapped $|1, 0\rangle$ state, the targeted atoms are ejected from the trap carrying away energy.

Thus by sweeping the rf frequency from high to low, we can target atoms selectively based on their energies to cool the atomic cloud. As long as the atom-loss rate is not too fast, this process leads to an increase in the phase-space density, since the volume decreases as the atoms with lower energies occupy the space closer to the center of the trap. Although we

are capable of creating BECs using this procedure, we stop evaporation above degeneracy to study spin transport properties of a non-degenerate trapped Bose gas presented in this thesis.

The atomic cloud cooled via evaporative cooling is then imaged in order to infer the trapped atomic sample properties. It is preferable to use a cycling transition as the imaging transition, since it increases the signal-to-noise ratio. The atoms are trapped in the $|1, -1\rangle$ state in the HIP trap, but there is no cycling transition to the excited state for this state. Therefore, first we coherently transfer the atoms from the $|1, -1\rangle$ state to the $|2, -2\rangle$ state using an adiabatic rapid passage (ARP) technique [65]. Then the $|2, -2\rangle \rightarrow |3, -3\rangle$ cycling transition is used for imaging (Fig. 3.4).

We use a destructive absorption imaging technique to measure the population of the atoms in the $|1, -1\rangle$ state. In this procedure the atomic cloud is illuminated with a resonant probe beam tuned to the $|2, -2\rangle \rightarrow |3, -3\rangle$ cycling transition using a PLL locking scheme. The atoms absorb the resonant probe light, producing a shadow of the atomic cloud, which is focused on a CCD camera. The optical density (OD) of the atoms is then calculated after corrections for background and saturation using Beer's law

$$OD = \ln(I_0/I), \tag{3.5}$$

where I_0 is the probe beam intensity, and I is the measured intensity when atoms are present. The number of atoms and temperature of the atomic cloud are calculated using the measured OD, since the measured OD depends on the number of atoms in the cloud that absorb the probe laser beam.

Several systematic effects are important to consider during the imaging process. The atomic energy splitting varies across the atomic cloud due to the inhomogeneity in the trapping magnetic field. Thus the probe light cannot be resonant with the entire cloud. Imaging the atoms in a more uniform magnetic field minimizes this effect. We also need to expand the atomic cloud beyond the resolution limit of our CCD camera. Expanding the cloud is also important to avoid a high absorption, otherwise we might underestimate the

number of atoms in the cloud. We expand the atomic cloud in the anti-trapped $|2, -2\rangle$ state after being transferred from the $|1, -1\rangle$ state.

Figure 3.4 shows the Zeeman-shifted ground and excited states in ^{87}Rb in low magnetic field and the imaging transitions. The atoms initially in the $|1, -1\rangle$ state in ~ 3 G magnetic field are transferred to the $|2, -2\rangle$ state in $t_{\text{ARP}}=0.65$ ms. In the $|2, -2\rangle$ state, the atomic cloud is expanded in an intermediate ~ 50 G magnetic field. After proper expansion the bias magnetic field value is increased to high 100 G and the imaging pulses are applied.

Generally, we fit the absorption image to three different functions depending on the degeneracy of the atoms, to infer the atomic cloud properties. For normal clouds studied in this thesis, we fit the image to a 2-D Gaussian, and the number, temperature and phase-space density are extracted using the fit parameters (see [85] for more details on cloud parameter calculations). For studying spin transport in trapped non-degenerate Bose gas we use near degenerate atomic clouds with peak density $n_0 \simeq 2 \times 10^{19} \text{ m}^{-3}$ and temperature $T = 650$ nK.

3.2 Experimental setup for spin transport studies

The two-level system (pseudo-spin 1/2) studied in this thesis project consists of two hyperfine ground-states of ^{87}Rb atoms confined in the external harmonic potential of a purely magnetic trap, described in the previous section. We study spin diffusion as a special case of spin transport. To generate longitudinal spin diffusion, we create a longitudinal spin gradient via preparing the system in a non-equilibrium two-domain structure of anti-parallel longitudinal spin states in the trapped non-degenerate sample of ^{87}Rb atoms as will be detailed in Section 3.4. We study the diffusion dynamics during the relaxation of the initial non-equilibrium spin state to the final equilibrium as the longitudinal spin gradient relaxes to zero.

The experimental spin doublet used here is shown in Fig. 3.5. It consists of two magnetically trapped hyperfine ground-states of ^{87}Rb : $|1\rangle \equiv |1, -1\rangle$ and $|2\rangle \equiv |2, 1\rangle$. For a specific magnetic field these states experience the same first-order Zeeman shift, thus the inhomogeneity in the transition frequency due to trapping magnetic field is minimized across the

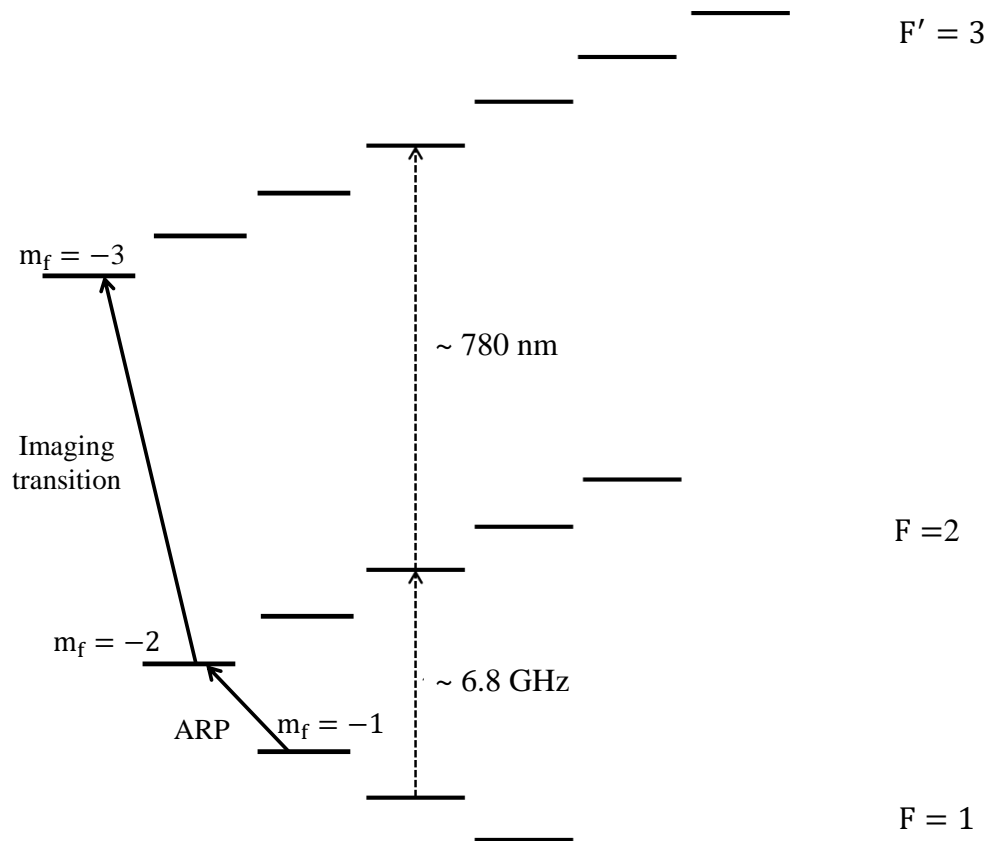


Figure 3.4: Zeeman-shifted ground ($5S_{1/2}$) and excited ($5P_{3/2}$) states of ^{87}Rb in low magnetic field. The ARP ($|1, -1\rangle \rightarrow |2, -2\rangle$) and imaging ($|2, -2\rangle \rightarrow |3, -3\rangle$) transitions are shown on the diagram. The energy separations are not to scale.

atomic distribution for small magnetic fields. The two states $|1\rangle$ and $|2\rangle$ are coupled via a two-photon microwave-rf transition. The transition cannot be induced by a single photon, since the two states are different by two units of angular momentum. We use a combination of optical patterning and microwave pulse techniques to prepare the initial two-domain spin texture as will be explained in Section 3.4. We manipulate the atomic energy splitting across the atomic cloud via the ac Stark effect induced by applying a patterned optical field. This gives us spatial control for state preparation.

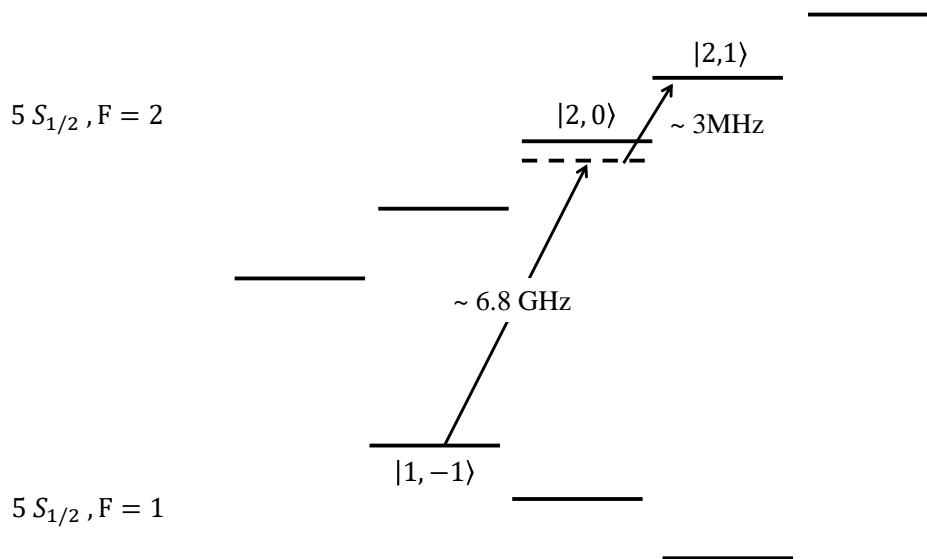


Figure 3.5: Zeeman-shifted ground-state of ^{87}Rb in low magnetic field. The pseudo-spin $\frac{1}{2}$ system consists of two trapped states $|1\rangle \equiv |1, -1\rangle$ and $|2\rangle \equiv |2, 1\rangle$ coupled via a two-photon transition. The microwave fields are detuned from the $|2, 0\rangle$ state to avoid populating the intermediate state.

The magnetically confined ^{87}Rb atoms are evaporatively cooled to just above quantum degeneracy with temperatures of the order of $T \sim 650$ nK and peak density $n_0 \sim 2 \times 10^{13} \text{ cm}^{-3}$. When no external fields are applied, the transition frequency between the two states ν_{12} is affected by the trapping magnetic field-induced Zeeman shift as well as the mean-field collisional shift, since both effects alter atomic energy levels. It is desirable to minimize the inhomogeneity in the differential energy splittings to achieve longer coherence

times. Also starting with a uniform differential potential simplifies spin-state preparation as is described in more detail in the following section.

3.2.1 Uniform differential potential

It is possible to cancel the effect of the differential Zeeman shift and mean-field collisional shift to achieve a uniform differential potential across the atomic distribution. This procedure is usually referred to as mutual compensation scheme. The transition frequency between the two states is measured via Ramsey spectroscopy (see Section 3.3.1), which gives the differential potential between the two states $U_{\text{diff}} = h\nu_{12}$.

The Breit-Rabi formula [88] gives the magnetic field dependence of each m_f energy level, when the m_f degeneracy is lifted in an intermediate magnetic field. This formula, which only applies to the ground state manifold of D transition, predicts a magic spot magnetic field $B_0 \sim 3.23$ G at which a minimum for the transition frequency between the two states is reached, also indicating that at $B = B_0$ the differential energy shift between the two states is first-order independent of the magnetic field. It is desirable to choose the magnetic field value close to B_0 to reduce the spatial inhomogeneity of ν_{12} across the cloud. The magnetic field near the bottom of the trap can be approximated as $B(z) = B_{\text{bias}} + \frac{B''}{2}z^2$. Close to the magic spot magnetic field B_0 , the differential Zeeman shift is $\nu_{12} = \nu_{\text{min}} + \alpha(B - B_0)^2$. Therefore; the position dependence of ν_{12} can be approximated proportional to $(\frac{B''}{2})^2z^4 + (B_{\text{bias}} - B_0)B''z^2$, which scales roughly as z^2 away from B_0 . By adjusting the bias magnetic field B_{bias} compared to B_0 , the differential Zeeman shift curvature can be made positive, negative or zero.

The other effect that modifies ν_{12} is due to the interactions between the trapped atoms. In the cold-collision regime, where the thermal de Broglie wavelength of a particle λ_{dB} is greater than the s-wave scattering length between the two particles a (see Chapter 2), atoms experience energy shifts equal to αgn . α is the two-particle correlation at zero separation, $g = \frac{4\pi\hbar^2}{m}a$ is the coupling constant and n the number density. For non-condensed indistinguishable bosons $\alpha = 2$ due to exchange symmetry. The differential mean-field

cold-collisional shift is then given by

$$\Delta_{MF} = \frac{4\pi\hbar^2}{m}[2a_{11}n_1 - 2a_{22}n_2 + 2a_{12}(n_1 - n_2)], \quad (3.6)$$

where m is the mass of a ^{87}Rb atom, a_{ij} is the s-wave scattering length between states $|i\rangle$ and $|j\rangle$ ($i, j=1,2$), and n_i is the density of atoms in state i [85]. This energy shift scales directly with the density; therefore, for a non-condensed cloud it has a Gaussian profile across the atomic distribution.

By tuning the magnetic field or the number density of the atomic cloud, we can cancel out these two differential contributions to create an approximately uniform differential potential, as schematically presented in Fig. 3.6. To reach the cancellation values for the magnetic field and the density, we keep the magnetic field constant and change the collisional energy shift by varying the density of the atomic cloud. We work at a magnetic field $B_{CS} = 3.3$ G close to the magic spot $B_0 = 3.23$ G, that produces a differential Zeeman shift with an opposite sign compared to the collisional shift, otherwise cancellation is not possible.

Adding arbitrary differential energy shifts to this uniform potential is possible by applying external fields. Our spin-state preparation technique involves adding an arbitrary external differential potential via the ac Stark effect by applying patterned optical profiles. Using these differential energy shifts combined with microwave pulse sequences, we initialize the two-domain longitudinal spin profiles used in this work to study spin diffusion, as will be discussed in more detail in Section 3.4.

3.2.2 The ac Stark effect and the light shift

The oscillating electromagnetic field of an off-resonant laser alters the atomic energy levels via the ac Stark effect. The electric field of the laser induces an atomic electric dipole moment, whose energy is altered due to interaction with the electric field of the laser. The resulting interaction potential between this induced dipole moment and the electric field is [89]

$$U_{\text{dip}}(r) = -\frac{3\pi c^2}{2\omega_0^3} \left(\frac{\Gamma}{\omega_0 - \omega_L} + \frac{\Gamma}{\omega_0 + \omega_L} \right) I(r), \quad (3.7)$$

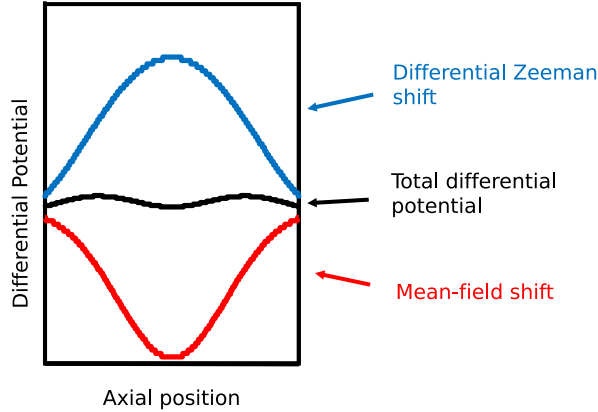


Figure 3.6: Schematic representation of the mutual compensation of the mean-field shift and Zeeman shift. The total differential potential is roughly uniform across the atomic distribution.

where Γ is the excited state spontaneous decay rate, ω_0 is the transition frequency, ω_L is the applied laser frequency and $I(r)$ is the laser intensity spatial distribution. The detuning $\Delta = \omega_L - \omega_0$ is defined as the difference between the atomic resonance frequency ω_0 and the laser frequency ω_L .

When the laser frequency is tuned close to resonance, $|\Delta| \ll \omega_0$, implementing the rotating wave approximation (RWA) leads to a simplified expression for U_{dip} ,

$$U_{\text{dip}}(r) = \frac{3\pi c^2}{2\omega_0^3} \left(\frac{\Gamma}{\Delta} \right) I(r). \quad (3.8)$$

By producing different laser intensity distributions across the atomic cloud, we can create differential potentials with arbitrary geometries. This technique is used in preparing the two-domain spin profile (Section 3.4), as well as adding effective magnetic fields with various size and symmetry for spin diffusion studies in Chapter 5.

The Stark laser

We use a tuneable external cavity diode laser with center wavelength at 780 nm to Stark shift the atomic energy levels. To stabilize its frequency, we use a PLL lock setup

and detune the laser frequency ~ 3 GHz below the resonant D_2 excited-state transition $|2, -2\rangle \rightarrow |3, -3\rangle$. By illuminating the atomic cloud with the laser beam at 3 GHz detuning and 130 W/m^2 intensity, we produce light shifts of the order of 200 kHz. We can modify the magnitude of the differential light shift by either adjusting the intensity of the laser beam or varying the laser detuning. This same Stark laser beam is used both in the procedure for initializing the two-domain spin profile (Section 3.4) as well as applying external effective magnetic fields in spin diffusion studies discussed in Chapter 5 (Section 5.3), in two distinct optical paths.

3.3 Spin transport measurement

In this section we describe different measurement methods used in the experimental studies presented in this thesis. The measurement of different properties involves absorption imaging of atoms to measure the atomic density distribution. The image is divided into equally spaced axial bins to achieve spatial resolution. The Ramsey spectroscopy method is used to measure differential energy shifts between the two states. This method was used for all the U_{diff} measurements presented here and in Chapter 5. Ramsey-type experiments, in which a $\pi/2$ -pulse rotates the transverse spin component S_{\perp} into longitudinal spin component S_{\parallel} , are used to measure the transverse spin component. The longitudinal spin projection is measured by directly measuring the distribution of atoms in states $|1\rangle$ and $|2\rangle$.

3.3.1 Ramsey spectroscopy

The Ramsey spectroscopy method is widely used in different fields of physics to measure coherence. A superposition of two particular quantum states is prepared, and the time evolution of the superposition state is studied. The relative phase of the superposition of the two states evolves proportional to the energy splitting between the two states during the superposition evolution time. A read-out pulse recombines the states interferometrically and a temporal interference pattern is created as a function of Ramsey pulse separation (labeled as evolution time T in Fig. 3.7(b)). The fringe contrast gives a measure of coherence in the system.

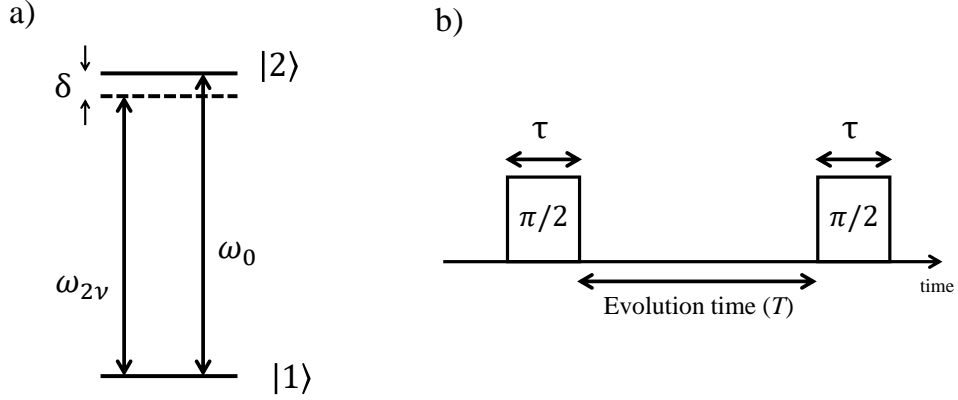


Figure 3.7: a) ω_0 is the resonant transition frequency between the two states $|1\rangle \equiv |1, -1\rangle$ and $|2\rangle \equiv |2, 1\rangle$ (Fig. 3.5) and $\omega_{2\nu}$ is the frequency of the applied two-photon pulses, with $\delta = \omega_{2\nu} - \omega_0$. b) Ramsey spectroscopy sequence.

The Ramsey method used here consists of two $\pi/2$ microwave pulses detuned from the two-photon transition by $\delta = \omega_{2\nu} - \omega_0$. ω_0 is the resonant transition frequency between the two states and $\omega_{2\nu}$ is the frequency of the applied two-photon pulse [Fig. 3.7(a)]. The two $\pi/2$ microwave pulses are separated by a varying free evolution time T as shown in Fig. 3.7(b). After the two pulse sequence, the probability of finding atoms in the excited state P_2 for $\delta \ll \Omega_R$ and pulse length $\tau \ll T$ is [85]

$$P_2(T, \delta) \simeq \frac{1}{2} + \frac{1}{2} \cos(\delta T). \quad (3.9)$$

Figure 3.8 shows the Ramsey spectroscopy process in the Bloch sphere representation schematically. The first $\pi/2$ pulse places the atoms in a coherent superposition of the two spin states. During the evolution time, the relative phase between the two states evolves at a rate proportional to the energy difference between them $\phi_{12} = \omega_0 T$, while the coupling drive acquires a phase $\phi_{2\nu} = \omega_{2\nu} T$, during the free evolution time. The second $\pi/2$ pulse recombines the two states interferometrically, depending on the relative accumulated phases.

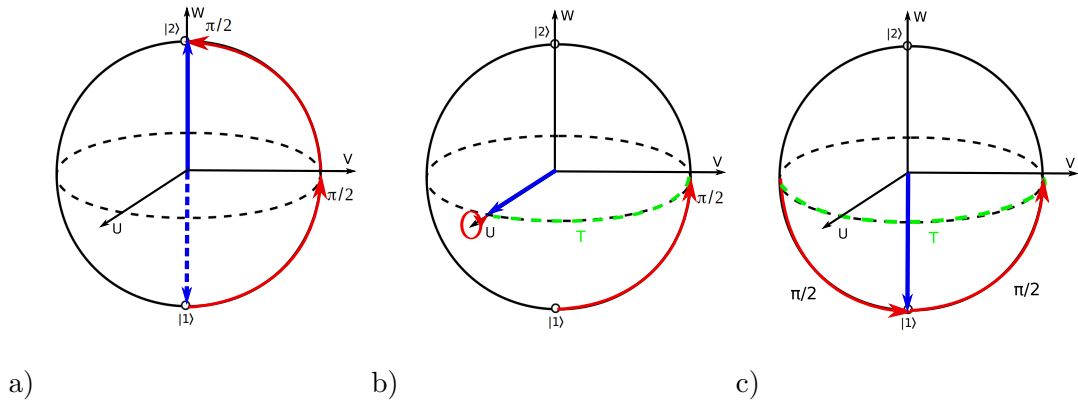


Figure 3.8: Schematic representation of Ramsey oscillations in Bloch sphere representation. Two $\pi/2$ pulses are detuned by $\delta = \omega_{\mu w} - \omega_0$ and separated by time T . (a) When $\delta T = 0$ the two-pulse sequence is equivalent to a π pulse. (b) When $\delta T = \frac{\pi}{2}$ the second $\pi/2$ does not transfer the atoms as the state vector is along the field's torque vector (U - axis). (c) When $\delta T = \pi$ the second $\pi/2$ transfer the atoms back to the initial state.

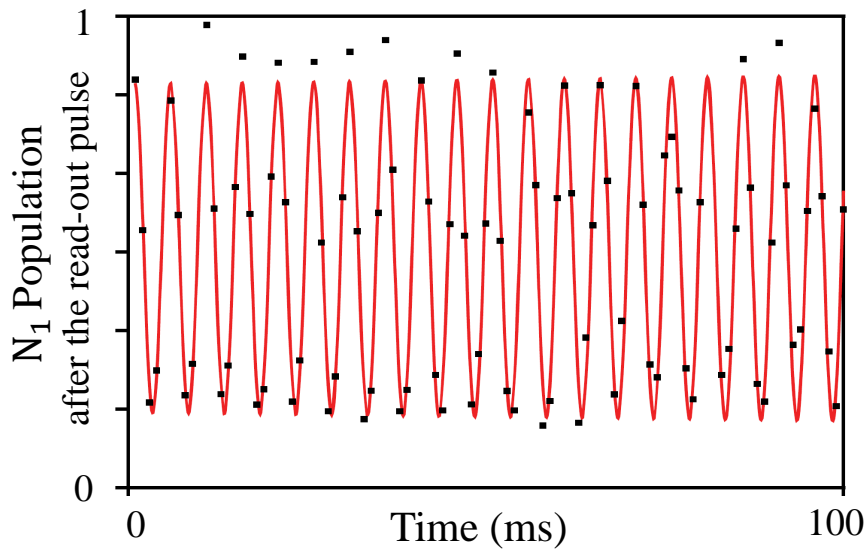


Figure 3.9: Ramsey spectroscopy data showing an oscillation of the population of atoms in state $|1\rangle$ measured after the second $\pi/2$ pulse in the center of the atomic distribution. The solid line is a fit to a sign wave as a guide to eye.

As a result, an oscillation of the population between the two states is observed as a function of the evolution time. Figure 3.9 presents a typical set of Ramsey oscillation data.

The fringe contrast measures coherence and decreases with time as a result of decoherence in the system. The frequency of the Ramsey oscillations is the difference between the transition frequency and the applied two-photon driving field. We extract the differential energy shift between the two states from the Ramsey oscillation frequency measurements. To achieve spatial resolution we divide the cloud into several axial bins and extract Ramsey oscillation frequency for each location separately. Figure 3.10 shows the results of this U_{diff} measurement procedure for cancellation of differential potential (red, \circ) prepared in the mutual compensation scheme, as well as differential potential data with positive (black, \square) and negative (blue, \square) linear gradients (see Section 5.3 for details). The error bars are from Ramsey fringe fitting errors.

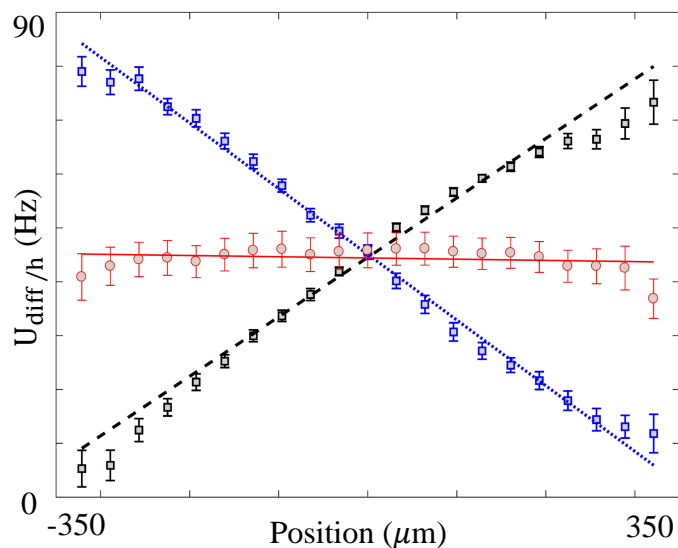


Figure 3.10: The Ramsey oscillation frequency as a function of axial position is shown. The differential energy shift between states $|1\rangle$ and $|2\rangle$ is extracted for different applied fields. (Red, \circ) shows uniform differential potential across the atomic distribution achieved in the mutual compensation scheme (red, \circ). Also are shown differential potential data with positive (black, \square) and negative (blue, \square) linear field gradients. Differential energy shifts are measured by Ramsey spectroscopy (Section 3.3.1).

3.3.2 The experimental method for reconstructing spin

Longitudinal spin

The longitudinal spin projection is measured by directly measuring the spatial distribution $N_i(z)$ of atoms in states $|1\rangle$ and $|2\rangle$ in separate experimental shots with the same initial conditions. The atomic cloud is divided to 23 axial bins for spatial resolution. The longitudinal spin is defined as the local population difference between the two states

$$S_{\parallel}(z) = \frac{N_2(z)}{N_{2\text{tot}}} - \frac{N_1(z)}{N_{1\text{tot}}}, \quad (3.10)$$

with $N_{i\text{tot}} = \sum_z N_i(z)$, $i = 1, 2$, summed over all axial bins. The time evolution of the longitudinal spin $S_{\parallel}(z, t)$ is studied by performing the same procedure of extracting longitudinal spin component distribution $S_{\parallel}(z)$ subsequent to the evolution of the system for different evolution times. We normalize the distribution in each state $N_i(z)$ to the total number in the same state $N_{i\text{tot}}$, to avoid including the effects due to the loss from state $|2\rangle$ from dipolar relaxation during $|2\rangle - |2\rangle$ collisions. The life time for both states $|1\rangle$ and $|2\rangle$ are measured in separate experiments and are higher (> 1 s) than relevant experimental timescales (~ 0.5 s). Figure 3.11 presents typical longitudinal spin distribution data.

Transverse spin

We use Ramsey-type experiments (Section 3.3.1) to measure the transverse spin component $\vec{S}_{\perp} = S_{\perp} e^{i\phi}$. Due to spin initialization processes the spin profile might have a transverse component, meaning the spin initialization processes effectively act as the first pulse in a Ramsey spectroscopy sequence. Therefore, only the second read-out pulse is applied to project the transverse spin into longitudinal spin. Measuring the number of atoms in states $|1\rangle$ after the read-out pulse is equivalent to measuring transverse spin prior to the read-out pulse application. This measurement method also creates an oscillation of the population of atoms between the two state $|1\rangle$ and $|2\rangle$ (Fig. 3.12), as seen in ordinary Ramsey spectroscopy. For these measurements, the amplitude of Ramsey oscillations gives the

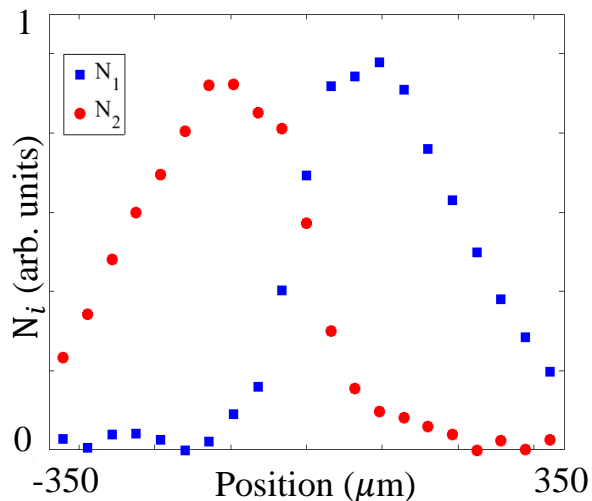


Figure 3.11: Population of atoms in the two states $|1\rangle$ ($N_1(z)$, \blacksquare) and $|2\rangle$ ($N_2(z)$, \bullet). The population in each state is measured in separate experimental shots. The atomic cloud is divided into 21 axial bins for spatial resolution.

transverse spin magnitude S_{\perp} , and the phase of these oscillations gives the transverse spin orientation ϕ .

Typical Ramsey spectroscopy experiment data for transverse spin measurement is presented in Fig. 3.12. The frequency of Ramsey oscillations (ν_{rm}) can be adjusted by changing the detuning of the two-photon driving field with respect to resonance. We use different Ramsey scan frequencies to achieve different levels of time resolution for transverse spin component measurements. To extract the spatiotemporal evolution of the transverse spin component $\vec{S}_{\perp}(z, t)$ we incorporate Ramsey scans with appropriate time resolution depending on the specific features of the dynamics we expect to observe. To detect rapidly changing features in the dynamics of the transverse spin component we need high resolution Ramsey scans. To study long time behaviour of the transverse spin component dynamics in reasonable experiment times, we use lower resolution for the Ramsey scans.

We extract the phase ϕ and amplitude S_{\perp} of the transverse spin component by fitting a sine wave with a fixed frequency but varying phase and amplitude in a moving window that includes at least one single Ramsey oscillation for each bin (Fig. 3.12). By moving this window in time across the Ramsey oscillation raw data for each bin we extract the time

evolution of the magnitude and phase of the transverse spin component across the atomic distribution, creating spatially resolved plots of $\vec{S}_\perp(z, t)$ time evolution.

Depending on the Ramsey spectroscopy sampling rate as well as the chosen size for the moving fitting window, some smoothing of the extracted results might happen. Therefore, great care must be taken while choosing the Ramsey scanning frequency before measurements and fitting window size during data analysis, in order to detect all the important features of the transverse spin dynamics. We discuss this procedure more specifically while presenting the relevant experimental results in Chapters 4 and 5.

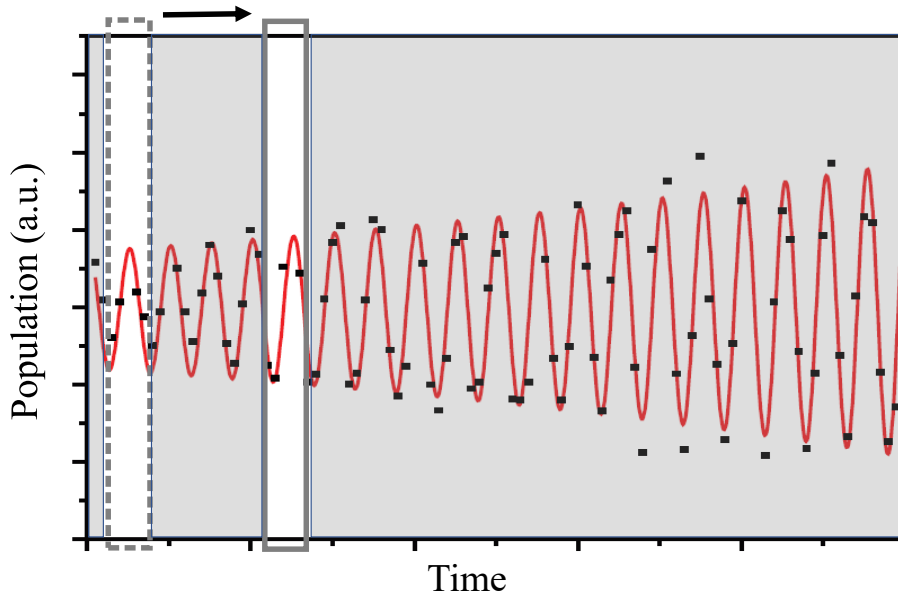


Figure 3.12: Ramsey oscillation data for a typical transverse spin component measurement. A sine wave with fixed frequency but time varying amplitude is fit to the data points in a window that encompasses more than one full Ramsey oscillation. This window is moved in time through each data set to extract the time evolution of the amplitude and phase of Ramsey oscillations. Maximum contrast is measured in a separate calibration Ramsey scan. Sample results of this analysis are shown in Fig. 4.6. The solid line here is a fit to a growing sine wave to guide the eye.

3.4 Spin profile initialization

In this section we describe the procedure used to prepare the two-domain spin profiles used in spin diffusion studies in this work. Initially in state $|1\rangle$, the ensemble is illumi-

nated with the off-resonant partially masked Stark laser beam (Section 3.2.2) that creates an optical step potential on top of the initially uniform differential potential presented in Fig. 3.10. The optical setup for producing the step optical potential is schematically depicted in Fig. 3.13. The masked laser ac-Stark shifts the atomic energy levels only on the illuminated side of the atomic distribution and the energy levels on the other half of the atomic distribution remain unchanged[Fig. 3.14(a,b)].

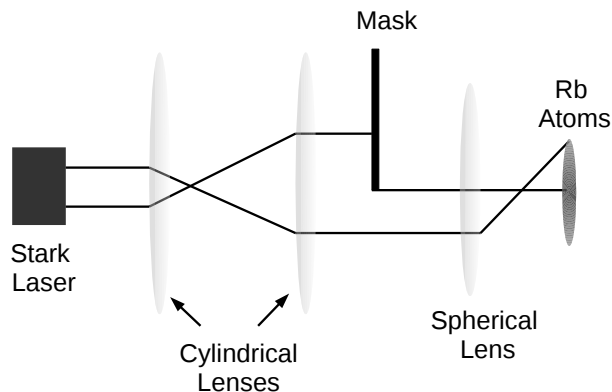


Figure 3.13: Optical setup used in producing the step optical potential schematically presented in Fig. 3.14(a). The collimated beam from the laser is expanded axially using a pair of cylindrical lenses. The dark mask is imaged on the atomic cloud by a single spherical lens.

This light shift is large compared to the resonant Rabi frequency $\Omega_R = 3.4$ kHz, and thus a π -pulse resonant with the unperturbed atoms is far detuned from the transition on the unmasked side, resulting in no transfer of atoms between the two states on the illuminated side of the atomic distribution (see [57]). The light shifts employed are ~ 200 kHz ($\sim 50\Omega_R$). Figure. 3.14(b) depicts the two-domain spin profile preparation sequence using the Bloch sphere representation of the spin doublet. Applying a microwave π -pulse to the atoms initially in $|1\rangle$ while illuminating them with the masked laser transfers atoms in the unilluminated half of the distribution to $|2\rangle$ and the atoms in the illuminated side remain in their initial state $|1\rangle$.

We use this initialization procedure to prepare the two-domain spin texture used in studying spin diffusion dynamics. Figure 3.15 shows the spatial atomic distribution in the

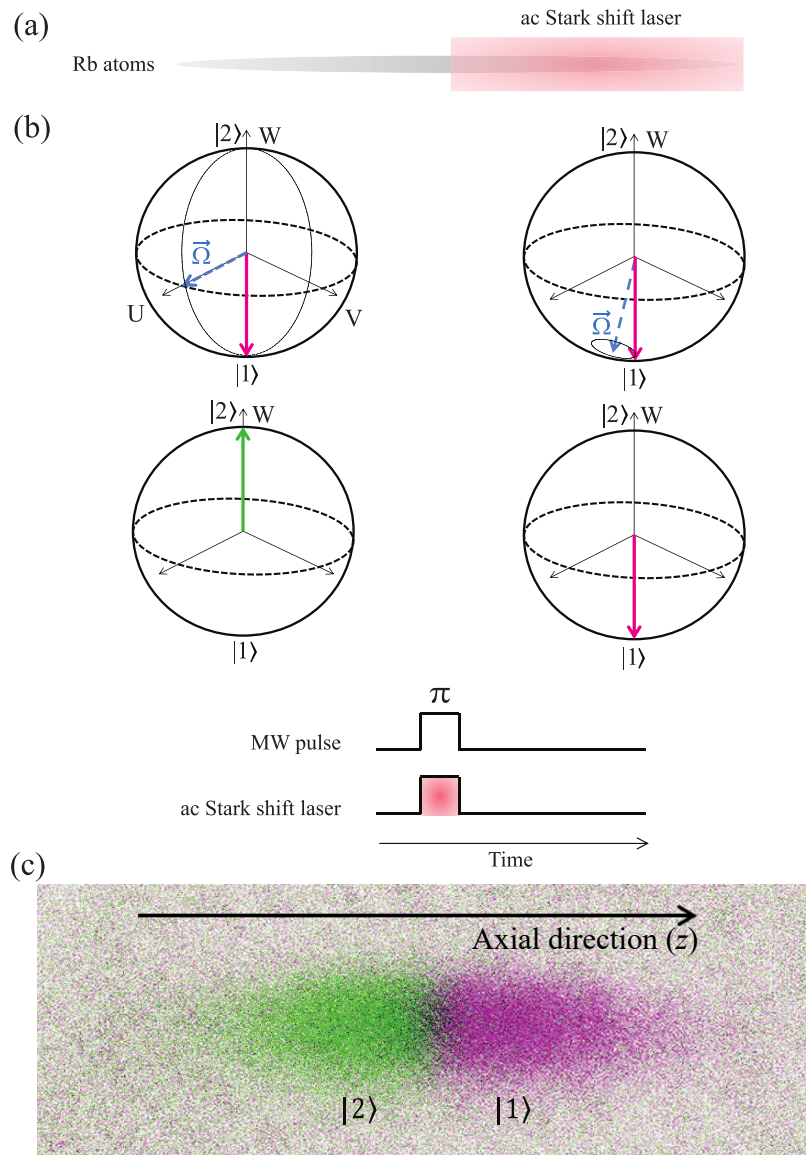


Figure 3.14: Preparation of the two-domain spin structure. (a) Conceptual schematic of the off-resonant patterned laser beam. (b) Bloch sphere representation of the two-domain spin structure preparation sequence: Applying a microwave π -pulse to the atoms initially in $|1\rangle$ while illuminating them with a masked laser transfers atoms in the unilluminated half of the distribution to $|2\rangle$. Time goes from top to bottom. (c) Composite image of atoms in $|1\rangle$ (right, purple) and $|2\rangle$ (left, green) following the initialization sequence and radial expansion, destructively acquired on sequential experimental sequences.

two states $|1\rangle$ and $|2\rangle$ measured after the initialization sequence. The initial longitudinal spin component $S_{\parallel}(z)$ of the two-domain spin profile Fig. 3.15(b) is extracted from the measured longitudinal spin data in Fig. 3.15(a) using Eq. 3.10. The characteristic parameters of this initial longitudinal two-domain domain profile are extracted from $S_{\parallel}(z)$.

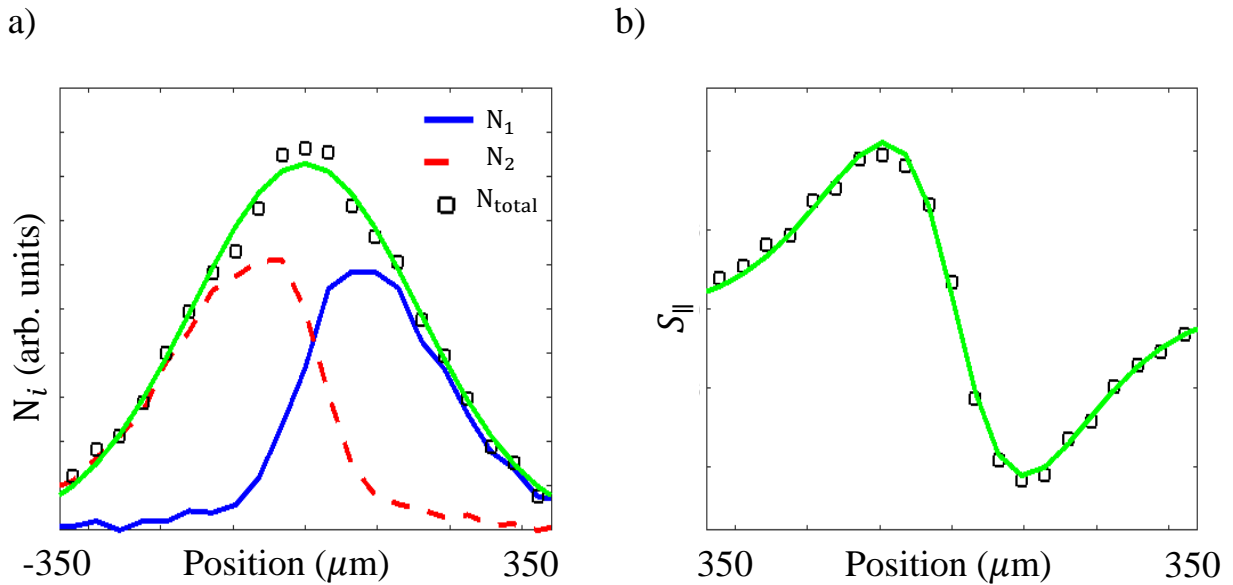


Figure 3.15: (a) Population of atoms in the two states $|1\rangle$ ($N_1(z)$, solid line) and $|2\rangle$ ($N_2(z)$, dashed line) at $T = 650$ nK and $n_0 \simeq 2 \times 10^{13} \text{cm}^{-19}$. The population in each state is measured in separate experimental shots. The sum of population in the two states $N_{\text{total}}(z) = N_1 + N_2$ (\square), is fit to a Gaussian function to extract the Gaussian half-width ($w_z \simeq 180(4) \mu\text{m}$) of the atomic distribution. As described earlier the cloud is divided axially into 21 bins for spatial resolution; here each data point corresponds to one bin. This data is used to reconstruct the longitudinal spin component. (b) Longitudinal spin component extracted using Eq. 3.10. We fit a Gaussian-weighted hyperbolic tangent function $S_{\parallel}(z) = A \exp(-z^2/2w_z^2) \tanh(z/\ell)$ to the initial $S_{\parallel}(z)$ to extract the initial domain-wall width $\ell \simeq 74(7) \mu\text{m}$ for the presented initial spin profile data here.

The initial transverse spin profile is measured using Ramsey spectroscopy with high frequency ($\nu_{rm} \sim 1$ kHz) at short times (~ 3 ms) compared to the evolution time (> 100 ms), to ensure that no dynamics is occurring while the initial transverse spin component in the domain-wall is measured. Figure 3.16(a) shows the transverse spin phase extracted from the measurement of initial transverse spin profile in the domain-wall. A schematic representation

of the transverse spin orientation across the domain-wall is depicted in Figure 3.16(b). The total initial spin profile prepared using the procedure described above is shown in Fig. 3.17. This procedure creates anti-parallel longitudinal spin domains separated by a helical domain-wall (Fig. 3.16) where the spin vector is coherently twisted, while remaining fully polarized.

The general procedure to study spin diffusion dynamics in this thesis project is as follows. After the desired spin texture preparation we let the initialized two-domain spin structure evolve in time and reconstruct longitudinal and transverse spin components using the methods described in the previous section. The next two chapters present the experimental results of these spin diffusion studies.

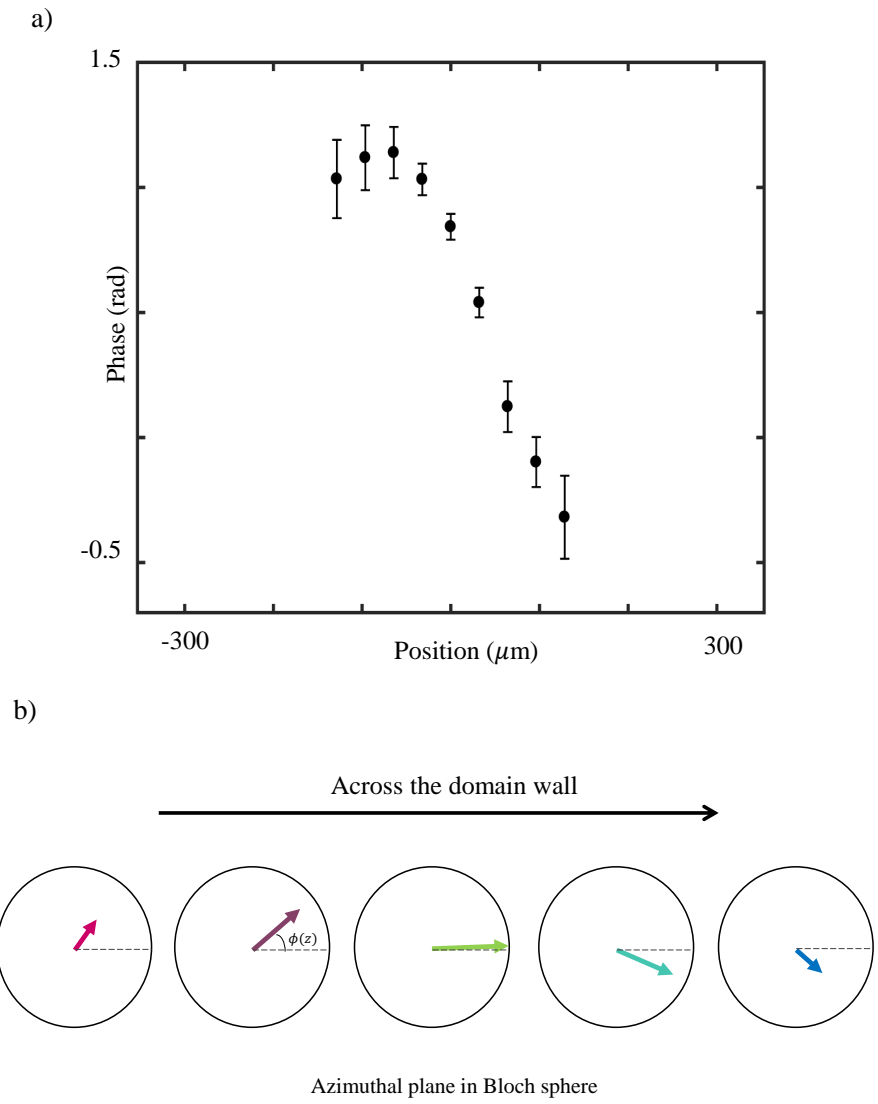


Figure 3.16: The initial transverse spin profile phase extracted from high resolution transverse spin component measurements is shown in (a). (b) Schematic depiction of the magnitude and orientation of the initial transverse spin component across the domain-wall region.

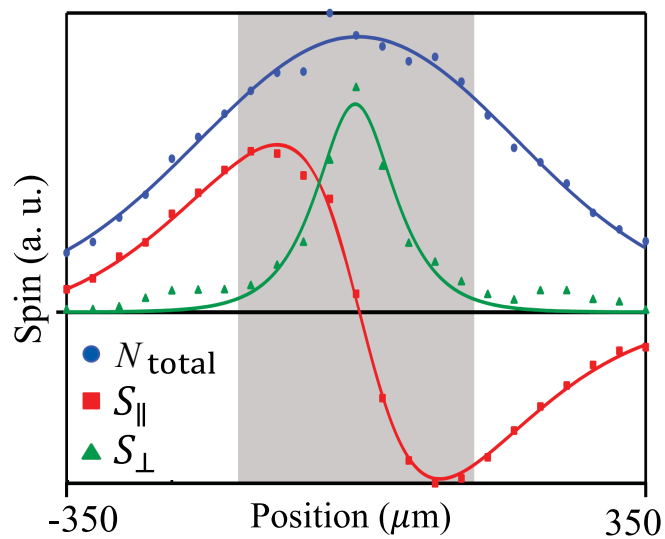


Figure 3.17: The initial two-domain spin profile consists of two anti-parallel longitudinal spin domains separated by a helical domain-wall. The initial transverse spin component magnitude S_{\perp} is extracted from Ramsey fringe contrast. The total spin $N_{\text{total}} \simeq N_1 + N_2$ is also shown. Solid lines are fits to a Gaussian (S_{total}), and the same Gaussian multiplied by $\text{sech}(z/\ell)$ (S_{\perp}) and $\tanh(z/\ell)$ (S_{\parallel}). The gray shaded region shows the domain-wall.

Chapter 4

Spin transport study in a trapped Bose gas

This chapter presents the experimental results of spin diffusion dynamics studies in a weakly-interacting trapped Bose gas. We initialize a one-dimensional two-domain antiparallel spin texture and observe the dynamics from this initial nonequilibrium profile to the final equilibrium state. In the first part of this chapter, we start by presenting a brief review of experimental spin transport studies in ultra-cold atomic systems. We continue by presenting the general results observed in our diffusion experiments for both longitudinal and transverse spin components and propose a phenomenological description for the observed behaviour. In the second part, we study how tuning the degree of initial coherence in the domain-wall region affects the diffusion dynamics. Finally, we discuss the mechanism governing the diffusion dynamics and present numerical results from numerical calculations of the semiclassical Boltzmann equation, covering a broader range of parameter space than is experimentally available in our current experimental setup.

4.1 Introduction

Collective spin behaviour occurs in degenerate Fermi liquids due to strong interactions in these quantum fluids and was the focus of many experimental and theoretical studies in late 1900s [45, 62, 63, 64, 90]. Though spin is a fundamentally quantum property, in dilute non-degenerate gases spin transport was expected to be accurately described by classical Boltzmann theory, since quantum degeneracy effects are absent in such systems. In 1982 Bashkin [48] and Lhuillier and Laloë [50] independently predicted that macroscopic

collective behaviour is feasible to occur in dilute non-condensed Bose and Fermi gases when the thermal de Broglie wavelength is larger than the two-body interaction length scale in collisions (see Chapter 2 for details).

In such conditions in the two-body collisions between identical atoms symmetrization requirements of the wave functions lead to exchange interactions described as an identical spin rotation effect (ISRE) in [50]. Therefore, transport properties of the system are significantly affected by these coherent interactions. In this regime, spin diffusion is no longer a purely dissipative process but rather a coherent effect dominated by the ISRE [77]. Quantum indistinguishability becomes important, and interactions are no longer just randomizing events on a path to equilibrium, but instead become coherent interactions that can drive macroscopic collective behaviour even at temperatures above quantum degeneracy. Following these theoretical predictions, many groups studied the effect in spin-polarized gases experimentally, manifesting interesting phenomena including spin waves [59, 60, 61], spin-wave instabilities during longitudinal spin diffusion [79, 80, 81] and spin-echo experiments [91].

In 2002, the observation of spin-state segregation by Lewandowski *et al.* in a trapped non-condensed Bose gas [52] was explained as overdamped pseudo-spin oscillations due to the ISRE during collisions [67, 73, 74, 75]. This observation and the following theoretical studies renewed the interest in studying the ISRE-driven collective behaviour in non-degenerate gases. Spin waves [40, 42], spin self-rephasing [54], collapse and revival of coherence [58] and non-conservation of transverse spin [81] are examples of the effect of this collective behaviour due to the ISRE, observed in trapped non-condensed gases since the first observation in 2002.

4.1.1 Review of spin transport studies in ultra-cold gases

Quantum modifications to spin transport manifest in various ways in ultra-cold atomic systems. Since strongly interacting Fermi gases provide a perfect model system to study the less understood non-equilibrium dynamics of strongly interacting fermionic matter, many transport studies focus on the behaviour of the strongly interacting Fermi gas close to unitarity. Here, we briefly present the results of a few of such spin transport studies.

Experiments on spin excitations in a strongly interacting Fermi gas by Sommer *et al.* showed reversal of spin currents [37]. A spin current was initially induced by spatially separating the center of mass of two opposite spin states. Following the initialization stage the system evolved in the external confining potential. The two spin states were observed to bounce off each other [Fig. 4.1(a)] resulting in quantum-limited spin diffusion. Their results show that although the collective density excitations are weakly damped in the hydrodynamic regime for a Fermi gas, the spin excitations are indeed maximally damped, and the interactions can be strong enough to reverse the spin currents.

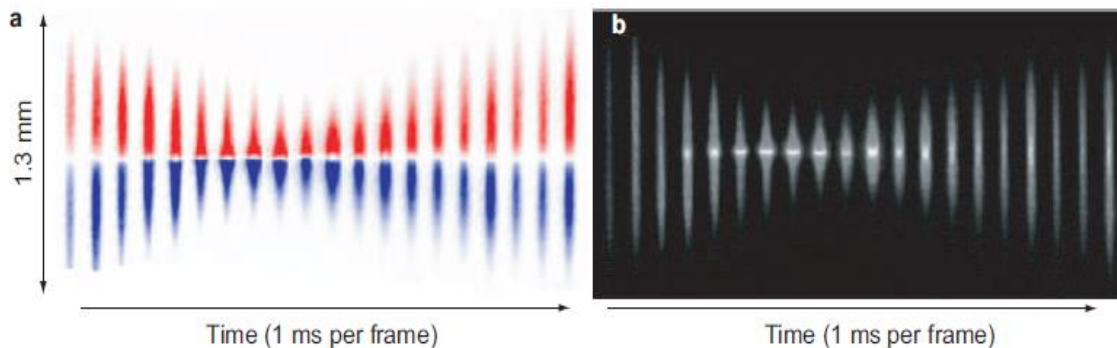


Figure 4.1: (a) The two oppositely polarized spin clouds of the strongly interacting Fermi gas bounce off each other. (b) The total column density, showing a high density region at the interface between the two opposite spin states due to collisions. Reprinted figure with permission from [37].

In two-dimensional Fermi gases, Koschorreck *et al.* measured the quantum limit of the lowest transverse spin diffusion constant for a strongly interacting Fermi gas, in a transversely polarized state [36]. Their results revealed an exceptionally low transverse spin diffusion constant in 2D, which is still unexplained and needs to be understood. They used a spin-echo technique to measure the transverse spin diffusion constant. In the strongly interacting regime, spin diffusion dominates spin transport, allowing the measurement of

the minimum transverse spin diffusion coefficient from the decaying spin echo signal. In the weakly interacting non-degenerate and degenerate regime for the Fermi gas under study, they observed spin waves due to the ISRE and effective spin-exchange interactions respectively. The observed spin-echo signal acquired an oscillatory character in the weakly interacting regime, as a result of the spin-wave excitation (Fig. 4.2).

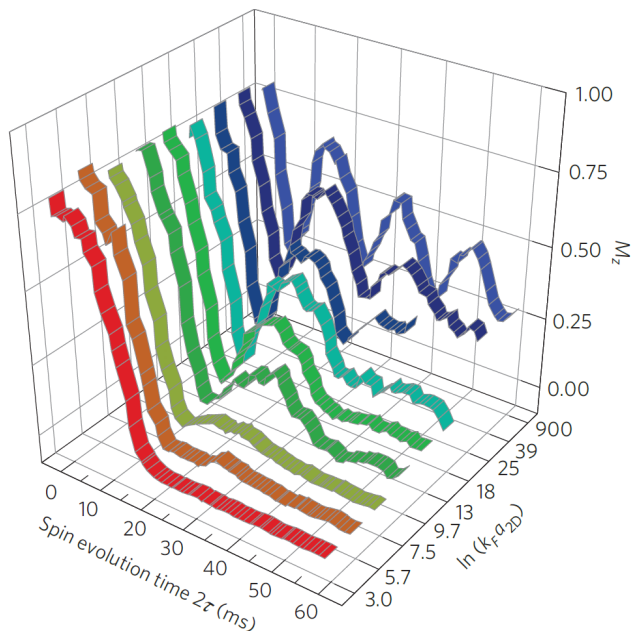


Figure 4.2: Time evolution of the spin oscillations as a function of interaction strength. For strong interactions the spin wave dynamics is suppressed. Reprinted figure with permission from [36].

Bardon *et al.* also studied the transverse demagnetization of a unitary Fermi gas but in three dimensions [34]. The initially fully polarized transverse spin profile developed a gradient in the transverse magnetization due to a linear magnetic field gradient. This gradient in the transverse magnetization lead to irreversible transverse diffusion in the strongly interacting limit, while exciting spin waves in the weakly interacting regime. The interaction strength was adjusted using a Feshbach resonance. The transverse spin diffusion coefficient was measured using a spin-echo technique as a function of the magnetic field gradient (temperature) at a fixed temperature (magnetic field gradient).

Motivated by the unexplained results observed in two-dimensional Fermi gases [36], Hild *et al.* explored the spin diffusion effect in a strongly interacting Bose gas instead [35]. They

used patterned spin textures of a Bose gas in the strong coupling regime in an optical lattice to study diffusion of one-dimensional and two-dimensional transverse pseudo-spin spiral states. Their results show diffusion-like behaviour in one dimension, but unexplained large departures from classical behaviour in two dimensions in agreement with results of [36].

While most studies in the field focus on degenerate Bose and Fermi gases, ultra-cold gases in the cold collision regime indeed exhibit interesting behaviour due to the spin-exchange interactions during collisions. For example the ISRE in the cold-collision regime modifies the transport properties of a weakly interacting ultra-cold gas. In the work presented in this thesis we study the quantum modifications to longitudinal spin diffusion dynamics in a weakly interacting non-condensed Bose gas.

Our results indeed manifest a significant deviation from classical diffusion, mainly due to the coherent spin interactions as a result of the ISRE, as also confirmed by numerical simulation of the transport equation. In the non-degenerate case of a one-dimensional two-domain spin structure of anti-parallel spins studied here, quantum modifications to spin diffusion are manifested as a decrease in the oscillation rate of the spin domains and an increase in the longitudinal spin diffusion time. This effect shows sensitivity to the degree of coherence in the domain-wall between the two spin domains, which highlights the quantum mechanical nature of the dynamics more clearly.

4.2 Quantum mechanical modifications to longitudinal spin diffusion in a non-condensed Bose gas

In any system with an out-of-equilibrium profile, currents of the associated out-of-equilibrium properties are generated to cancel out inhomogeneities and send the system back to its final equilibrium state. In a two-component system without any external potentials, the final equilibrium state is reached when the two components have uniform densities. Therefore, any nonuniformity in the density of atoms in either state generates currents to cancel out these inhomogeneities. In the pseudo-spin (two-level) description in our system, with longitudinal spin defined as the difference in the population of the atoms in the two

different states and transverse spin defined as the population of atoms in the superposition of the two states (Section 3.3.2), the final equilibrium corresponds to a state with zero spin, when the system is equivalent to a classical mixture of atoms in two different states. The mean-field energy gradient across the atomic cloud with initial longitudinal domains act as an effective magnetic field. This effective magnetic field is negligible compared to the external trapping potential, due to similarities in different s-wave scattering lengths for ^{87}Rb with $a_{22} = 95.47a_0$, $a_{12} = 98.09a_0$, and $a_{11} = 100.44a_0$ (a_0 is the Bohr radius) [85].

In the initial spin profile we create, the centers of mass of the atoms in the two pseudo-spin states are spatially separated, which corresponds to a longitudinal spin gradient. This spin inhomogeneity can generate spin currents to diffuse along the initial spin gradient and bring the system back to the final uniform equilibrium state. Therefore, this tailored spin profile provides us with an appropriate system to study spin diffusion in a less studied regime of weakly interacting non-condensed gas, where one can observe the cross-over between classical and quantum diffusion. We can explore this intermediate regime by adjusting the quantum effects occurring in the system during the time evolution.

This adjustment could be simply controlling the degree of coherence in the domain-wall. Since decreasing the degree of coherence in a system weakens the quantum effects, we expect classical behaviour in the low coherence limit. The results of studying this effect are presented later in this chapter (Section 4.3). In addition, this adjustment can be done by controlling the coherent spin dynamics in the system in a more complicated manner by adding external magnetic fields. We study this effect in detail in Chapter 5, by adjusting the symmetry and size of the effective magnetic field to adjust the longitudinal domain lifetime via controlling the coherent spin dynamics occurring in the domain-wall region. A historical background of studying the effect of nonuniform magnetic fields on spin dynamics is also discussed in the introduction of Chapter 5 (Section 5.1.1).

The theoretical description of the system studied here is explained in detail in Chapter 2. Here we summarize the results relevant to the experimental studies in this work and describe the experimental observables. The mechanism for coherent atom-atom scattering is the identical spin rotation effect (ISRE), where exchange scattering between indistin-

guishable particles with different spin leads to a precession of each atom's spin about their combined spin. As discussed in detail in Chapter 2, we describe the time evolution of the spin distribution $\vec{M}(p, z, t)$ with a one-dimensional quantum Boltzmann equation that includes the ISRE via a spin-torque term

$$\partial_t \vec{M}(p, z, t) + \partial_0 \vec{M}(p, z, t) - \vec{\Omega} \times \vec{M}(p, z, t) = \frac{\partial \vec{M}}{\partial t} |_{1D}, \quad (4.1)$$

where $\partial_0 = \frac{p}{m} \frac{\partial}{\partial z} - \frac{\partial U_{\text{ext}}}{\partial z} \frac{\partial}{\partial p}$ and $\vec{\Omega} = (U_{\text{diff}} \hat{w} + g \vec{S})/\hbar$. $g = \frac{4\pi\hbar^2 a}{m}$ is the mean-field interaction strength for two scattering particles with s -wave scattering length a and mass m . The experimental observable quantity is $\vec{S}(z, t) = \int dp \vec{M}(p, z, t)/2\pi\hbar$, with S_{\parallel} the longitudinal spin component and $\vec{S}_{\perp} = c e^{i\phi}$ with c the transverse spin component magnitude, which quantifies the spin coherence, and ϕ the superposition phase. For the rest of this thesis we replace S_{\perp} with c , for simplicity. U_{diff} and U_{ext} are the differential potential experienced between the two states and the trapping potential, respectively.

4.2.1 Experimental study of longitudinal spin diffusion in uniform magnetic fields

Figure 4.3 shows the experimental sequence used for longitudinal spin diffusion studies schematically. The experimental sequence is summarized as follows. After the initialization sequence (Section 3.4) the spin structure evolves in a uniform magnetic field with field gradient $G \simeq 0$ Hz/mm achieved using the mutual compensation scheme. The longitudinal spin component S_{\parallel} is then measured destructively by measuring the population of atoms in each state, followed by extracting the population differences (Section 3.3.2). The transverse spin component is measured using the Ramsey spectroscopy method (Section 3.3.1). Figure 4.4 shows typical spatiotemporal evolution for the relaxation of the two-domain spin structure to its final equilibrium for both the longitudinal and transverse spin components.

Figure 4.4(a) shows data for the longitudinal spin component, showing an oscillation of the longitudinal spin domains as well as diffusion of the longitudinal spin gradient. The classical longitudinal diffusion time scale is on the order of the elastic collision time $\tau_{el} \sim 24$ ms for these experimental parameters, but our measurements reveal that the longitudinal

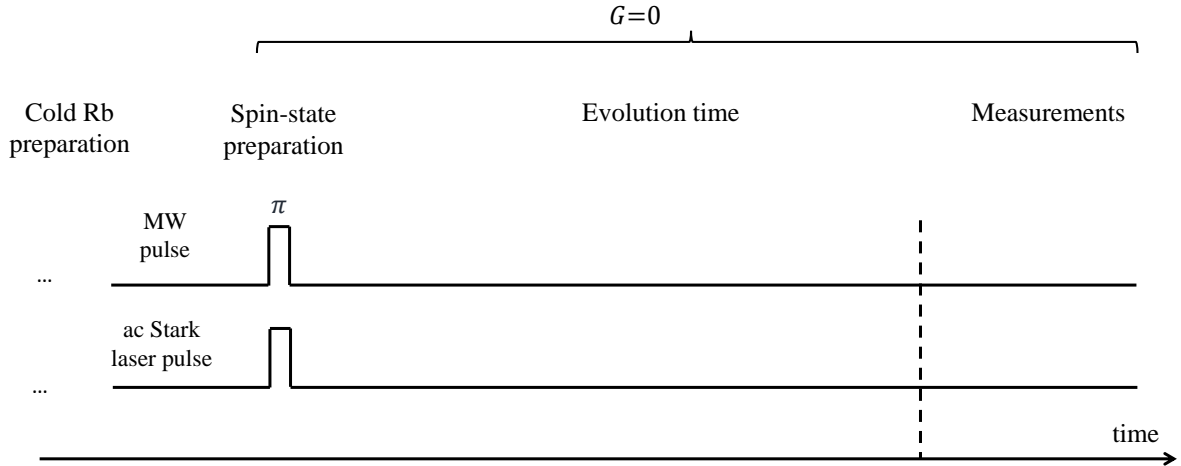


Figure 4.3: Schematic depiction of the experimental sequence used for spin diffusion studies in uniform magnetic fields.

domains persist for around 10 times longer than expected for the classical longitudinal diffusion. Also the domains oscillate much slower than trap oscillations $f_{\text{axial}}/f \sim 7$, with f_{axial} the axial trap oscillation frequency and f the frequency of the longitudinal domain oscillation. The existence of the transverse spin component in the coherent domain-wall has a stabilizing effect on the two-domain spin structure, which agrees with theoretical predictions and previous experiments in spin-polarized gases [79, 80, 81, 90]. We study this effect in more detail by controllably tuning the magnitude of the initial transverse spin component in the domain-wall, and the results are presented later in this chapter (Section 4.3).

The more striking results are observed in the time evolution of the transverse spin component. Figure 4.4(c) shows the spatiotemporal evolution of the amplitude of the transverse spin extracted from the Ramsey spectroscopy measurements [Fig. 4.4(d),(e)]. The Ramsey fringe contrast rapidly rises within the longitudinal spin domains, where the initial fringe amplitude is small [Fig. 4.4(e)], showing the spread of transverse spin component toward the edges of the atomic cloud, as seen in Fig. 4.4(c).

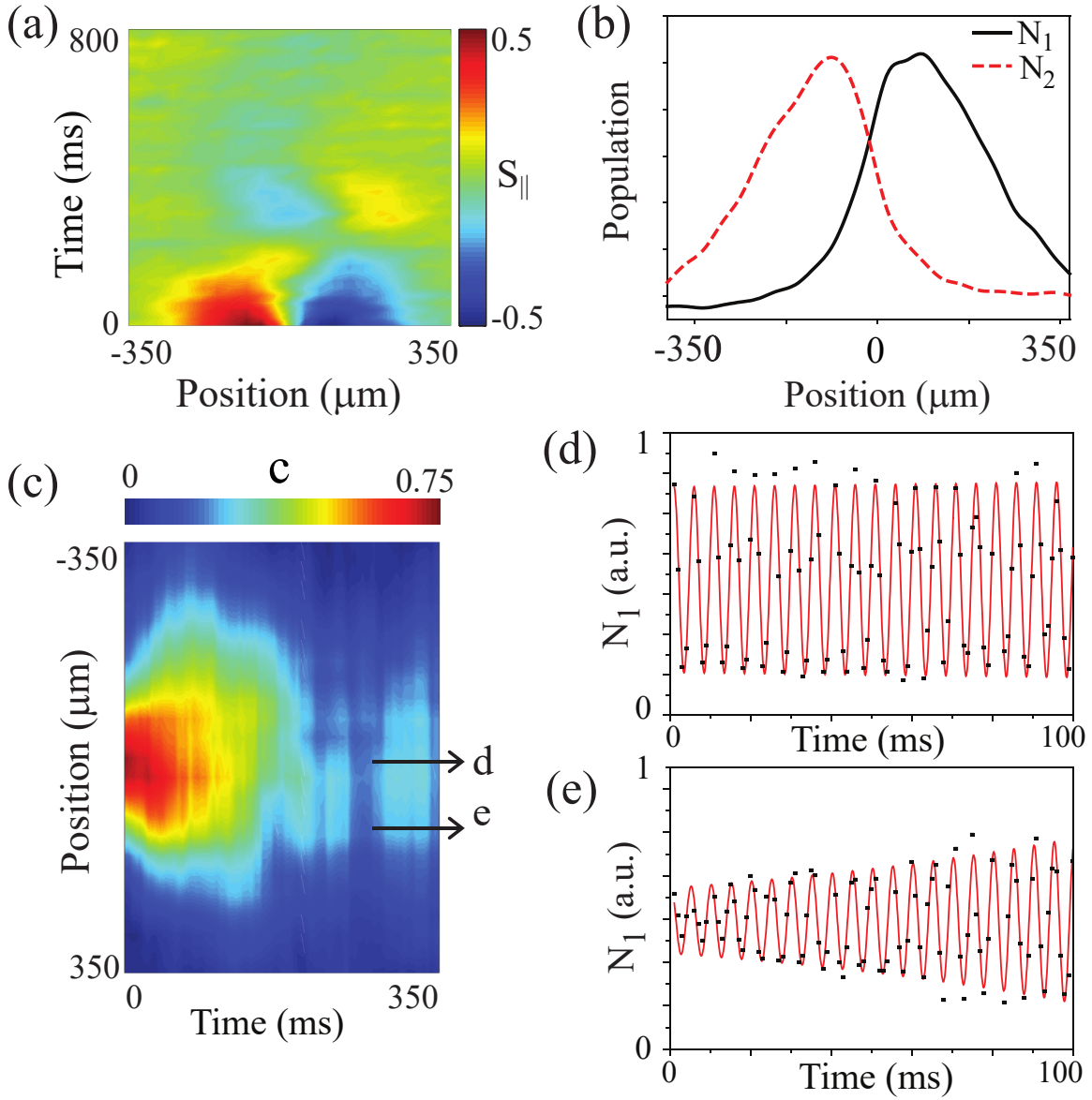


Figure 4.4: Time evolution of the two-domain spin structure. (a) Longitudinal spin component, S_{\parallel} , evolution shows increased longitudinal spin domain lifetimes. (b) Typical population measurements of $|1\rangle$ (solid line) and $|2\rangle$ (dashed line) at $t = 1 \mu\text{s}$, used to extract the longitudinal spin projection. (c) Evolution of transverse spin component amplitude, $c(z, t)$. Initially the transverse spin component is confined in the center of the atomic distribution in a region of width $\sim 0.6 \times w_z$. The transverse spin magnitude calculated from Ramsey fringe contrast rapidly spreads toward the edges of the atomic cloud where initial transverse spin magnitude is small, covering a region of the size $\sim 1.4 w_z$ by 200 ms. Ramsey fringes at (d) the trap center and (e) edge of the atomic distribution as shown by arrows (d,e) respectively in (c).

The observed spreading of the transverse spin component could result from diffusion of the transverse spin, but Fig. 4.5 shows that the total transverse spin magnitude in the gas increases, without any decrease observed in the fringe contrast in the center of the initial domain-wall region as seen in Fig. 4.4(d). This increase implies that the appearance of the transverse spin component on the edges of the atomic cloud is not due to spin diffusion, but rather is due to conversion of longitudinal spin component into transverse spin component as a result of an instability in the longitudinal spin current. This effect has been observed in spin-polarized gas systems [79, 80] and was described as an experimental manifestation of Castaing’s instability (Section 2.3.2) [81].

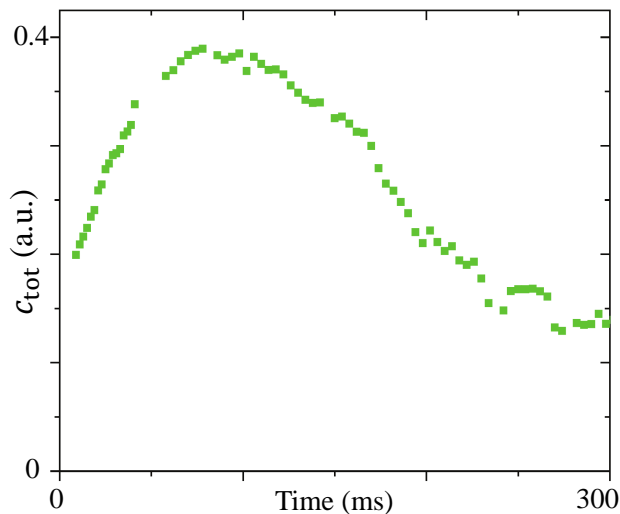


Figure 4.5: The total ensemble transverse spin magnitude c_{tot} is shown as a function of time. c_{tot} is calculated by summing transverse spin magnitude for all the bins across the atomic cloud $c_{\text{tot}}(t) = \sum_{i=1}^n c_i(t)$, with $n =$ number of axial bins. At the initial stage of the dynamics $t < 100$ ms the total transverse spin increases rapidly, followed by a gradual decay. Beyond 300 ms sine fits are less reliable due to low signal-to-noise ratio and are not included.

Although the trapped atomic systems possess different experimental parameters than untrapped spin-polarized gases, the physics governing the phenomenon is similar [55, 56, 76]. As discussed in Reference [76], in nonuniform magnetic fields if the transverse spin is confined in the domain-wall area, it dephases and the gradient in S_{\parallel} decays via ordinary longitudinal diffusion. This happens due to the fact that the kinetic equation decouples for purely longitudinal and transverse spin components, since the ISRE only acts on spins

that are fully or partially indistinguishable [51]. Though if the ISRE is large enough (ISRE parameter $\mu \gg 1$), the longitudinal spin current becomes unstable, a coupling between longitudinal and transverse spin dynamics occurs and the S_{\parallel} gradient decays via transverse diffusion across the coherent domain-wall. This transverse spin-mediated longitudinal diffusion increases the longitudinal diffusion times significantly. This increase in the longitudinal spin domain lifetime is due to the coherent spin interactions for transverse spin component, which are absent from purely longitudinal spin dynamics, as will be discussed in more detail in Section 4.4.

The other remarkable feature in the transverse spin evolution is the time evolution of the transverse spin phase ϕ . Figure 4.6(b) shows the spatially resolved time evolution of the transverse spin phase for regions marked as (i),(ii) and (iii) in Fig. 4.6(a). The transverse spin phase stays almost stationary for the full course of the dynamics showing very little change, resembling a situation in which the spin vector is gradually rotated as it passes through the domain-wall.

This stable phase behaviour is not expected from a first guess, since the transverse dynamics is dominated by the ISRE, which tends to result in oscillations in both amplitude and phase of the transverse spin component. Though, we emphasize that we start with an initial spin profile that is mostly longitudinally polarized and the transverse spin component is mainly confined in the domain-wall region. The transverse spin component slightly spreads toward the edges of the atomic distribution as the system evolves in time but never reaches a configuration in which the transverse spin component covers the whole cloud. Since the ISRE acts only on the spins that are fully or partly indistinguishable (*i.e.* transverse), purely longitudinal spins do not contribute in the ISRE-generated spin rotations. Due to this specific initial spin profile, the spin rotation interactions tend to homogenize the transverse spin orientation locally, and the phase profile stays uniform [Fig. 4.6(b)].

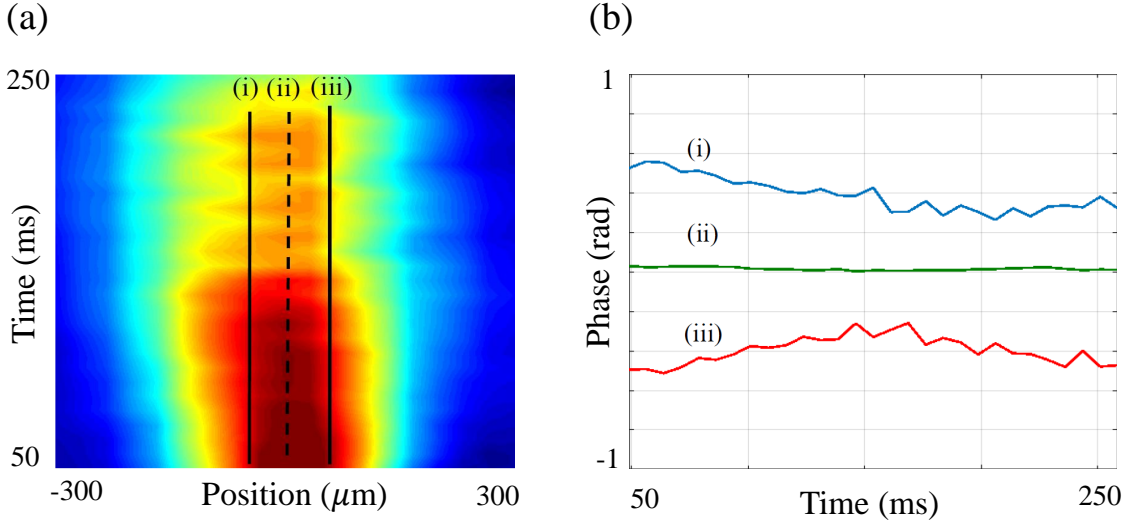


Figure 4.6: (a) Dynamics of the transverse spin amplitude in uniform external magnetic field. (b) Dynamics of the transverse spin phase for regions denoted as (i),(ii) and (iii) in (a). The initial transverse spin phase across the atomic distribution stays unchanged during the relaxation of the two-domain spin profile.

4.3 The effect of the initial transverse spin magnitude in the domain-wall

This section focuses on the experimental study of the effect of the initial transverse spin magnitude in the domain-wall on the diffusion dynamics for the two-domain spin structure. As discussed earlier in this chapter, a transverse spin domain-wall increases the longitudinal spin domain lifetime, due to the coherent spin dynamics in the transverse spin channel. To further study this effect experimentally, we optically adjust the initial transverse spin magnitude in the domain-wall and study the relaxation of the two-domain spin structures prepared with different transverse spin magnitudes in the domain-wall to the final equilibrium state.

The spin texture preparation method we use (Section 3.4) creates anti-parallel spin domains separated by a helical domain-wall where the spin vector is coherently rotated; therefore, the domain-wall's transverse component is initially fully coherent. We use an optical method to controllably adjust the initial amount of coherence in the domain-wall.

We apply a short pulse (0.2 - 0.5 ms) of strong off-resonant laser beam that is spatially nonuniform, targeted locally on the domain-wall region. We use the same laser beam used for spin profile preparation (Section 3.2.2), since it creates a sharp axial gradient (~ 200 KHz) in the differential potential experienced by atoms across the domain wall region. This laser pulse creates a highly nonuniform differential atomic potential, whose inhomogeneity introduces rapid dynamically averaged dephasing of the initial transverse spin component in timescales < 1 ms, creating domain-walls with lower initial transverse spin magnitude.

The degree of coherence is controlled by the optical pulse length and inhomogeneity. We keep the spatial profile of the laser beam constant, therefore the degree of coherence is controlled solely by the pulse length. The initial amount of coherence in the domain-wall is measured immediately after the preparation pulses are applied via Ramsey spectroscopy with high resolution ($\simeq 1$ kHz). By exploiting this forced dephasing procedure we create domain-walls with initial coherence reduced by up to 70 %, to cover the range of initial domain-wall coherence we choose to explore. We can achieve lower coherence amounts by applying longer pulses, but longer pulses tend to alter the initial domain profile and longitudinal spin gradient; therefore, those studies are not included in the results presented here. Also, for very low amounts of transverse spin the Ramsey fringe contrast might not be detectable compared to the shot-to-shot noise. Figure 4.7 summarizes the experimental sequence used for exploring the effect of domain-wall coherence on diffusion dynamics of the two-domain spin structure.

Figure 4.8(a)(i-iii) shows the longitudinal time evolution for different initial degrees of coherence in the domain-wall; from top to bottom the initial domain-wall coherence is $c_{\text{init}} = S_{\perp}/S_{\perp}^{\text{max}} = 0.74, 0.51, 0.28$ respectively in the cloud center. The longitudinal lifetime of the two-domain spin structure decreases with lower initial coherence in the domain-wall. Dynamics for a two-domain structure in a uniform external magnetic field are dominated by the dipole mode, which we isolate via the dipole moment of the spin distribution, $\langle zS_{\parallel}(z, t) \rangle = \frac{1}{n} \sum_{i=1}^n z_i S_{\parallel}(z_i, t)$, where n denotes the axial bin number. Figure 4.8(b) shows time evolution of the calculated spin-dipole moments for the data in Fig. 4.8(a)(i-iii). The frequency f and damping rate Γ of longitudinal oscillations are extracted from these

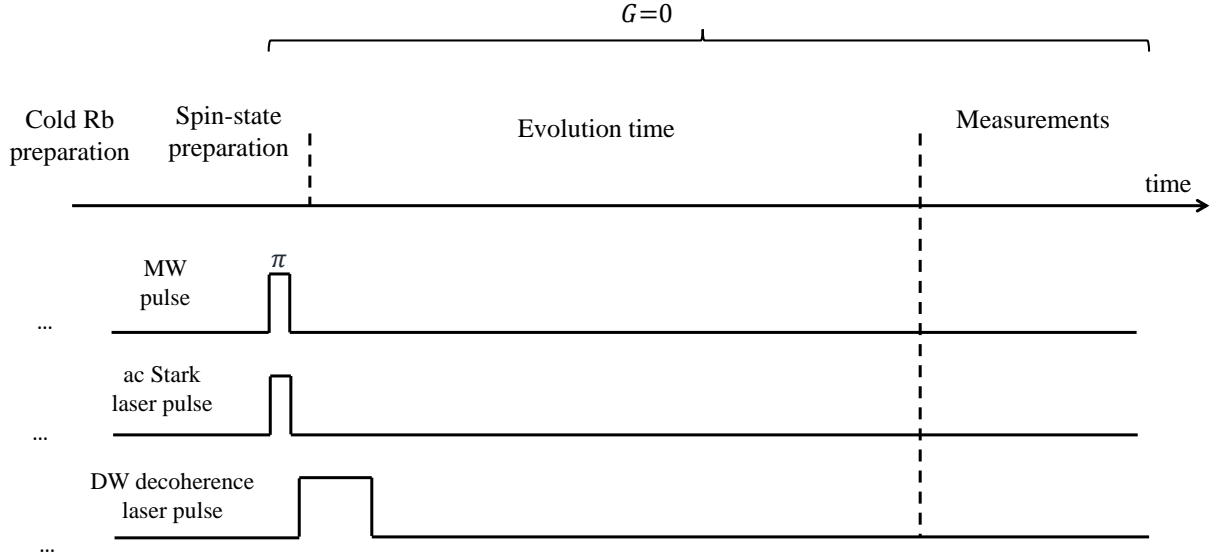


Figure 4.7: Schematic depiction of the experimental sequence used for studying samples with different initial degrees of coherence in the domain-wall.

by fitting an exponentially damped sine function to the dipole moment oscillation. The fitted curve is shown with the black line in Figure 4.8(b) for the $c_{\text{init}} = 0.28$ data points.

We repeat the experiment for different initial amounts of coherence, c_{init} ; calculate the time-dependent dipole moment; and extract f and Γ from exponentially decaying sinusoidal fits to these dipole moment oscillations. The results show both the frequency of longitudinal spin domain oscillations as well as longitudinal spin diffusion rates decrease as domain-wall coherence is increased. Figure 4.8(c) and (d) summarize the results. Both Γ and f decrease as c_{init} increases, showing the stabilizing effect of a coherent domain-wall. The longitudinal spin domain oscillation frequency is primarily controlled by two factors: oscillations in the harmonic trapping potential and mean-field-induced spin rotation. In the incoherent limit, f approaches the trapping frequency as the upper limit for domain oscillation frequency, as the system approaches a mixture of distinguishable classical ideal gases that diffuse according to classical Boltzmann theory. The large c_{init} limit entrains longitudinal diffusion with slower transverse diffusion.

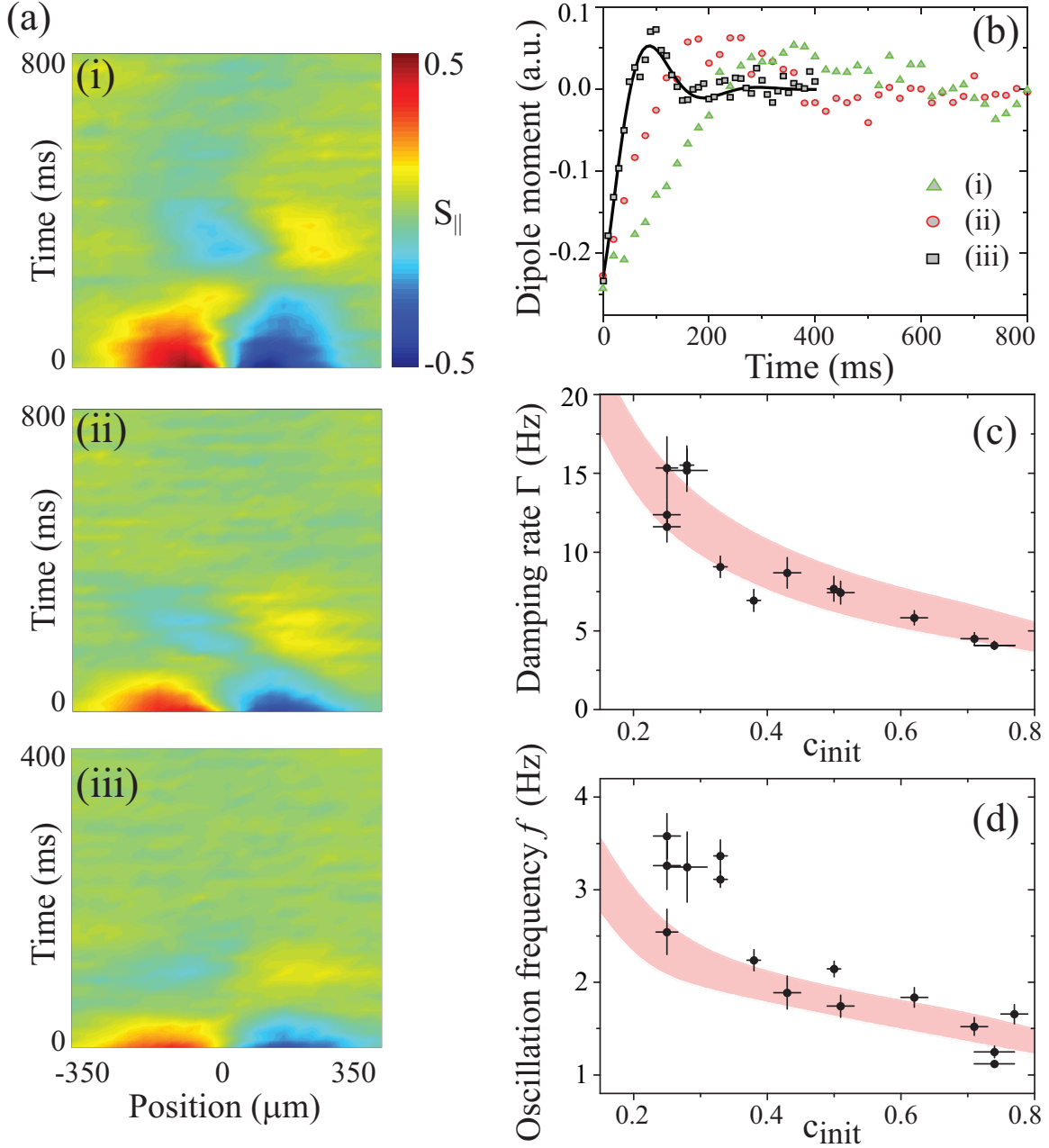


Figure 4.8: (a) Time evolution of S_{\parallel} for different initial domain-wall coherences, from top to bottom $c_{\text{init}} = S_{\perp}/S_{\perp}^{\text{max}} = 0.74, 0.51, 0.28$ respectively in the cloud center. (b) Dipole moment time evolution calculated from (a), with a representative decaying sinusoidal fit to (iii) $c_{\text{init}} = 0.28$. (c) Damping rate and (d) oscillation frequency of the dipole moment for different c_{init} . Error bars correspond to fit uncertainties for dipole moment oscillations and c_{init} measurements. The shaded band is the result of numerical simulations of Eq. 4.1.

We compare these measurements with transport theory by numerically solving Eq. 4.1. We solve the one-dimensional transport equation (Eq. 4.1) using an alternating direction implicit finite difference method (see [41] for details). We simulate the dynamics by using numerical cloud parameters and initial spin profiles that match our experimental parameters. The shaded regions in Fig. 4.8(c) and (d) represent one-sigma confidence bands from Monte Carlo simulations of Eq. 4.1, including statistical fluctuations ($\sim 10\%$) in n , T , and domain-wall size, as well as a systematic density calibration uncertainty ($\sim 20\%$). The data agrees well with theoretical predictions without any free parameters. Discrepancies in f at low coherence are likely due to challenges in fitting critically damped oscillations where the quality factor drops. Overdamping should occur for $c_{\text{init}} < 0.2$, but reducing coherence to this level without altering the longitudinal spin domains is challenging.

The effect of the spin instability can be seen more clearly in the transverse spin dynamics as shown in Fig. 4.9. The time evolution of $S_{\perp}(z, t)$ for different initial domain-wall coherence is shown in Fig. 4.9(a). The rise and spread of coherence for different c_{init} shows similar spatial behaviour, but S_{\perp} persists longer when there is more coherence in the domain-wall initially. Figure 4.9(b) shows the evolution of coherence in different regions of the cloud for the high c_{init} preparation [Fig. 4.9(a)-(i)].

Figure 4.9(c) shows total ensemble coherence, $c_{\text{tot}}(t)$, for different c_{init} , calculated by summing the coherence across the cloud. Coherence rapidly rises followed by a gradual decrease, but with different timescales for different c_{init} . We use different sampling rates for Ramsey spectroscopy to measure both the fast initial rise of coherence and longer relaxation to equilibrium. The dashed box in Fig. 4.9(b) indicates this change in sampling rate for Ramsey measurements. Maximum total coherence reached across the cloud depends on the initial coherence, and the time to reach maximum coherence also increases as c_{init} increases. These results highlight the transverse source of enhanced lifetimes of longitudinal spin domains with a coherent domain-wall. The presence of transverse spin component in domain-walls links transverse and longitudinal diffusion timescales. The longitudinal spin domain lifetimes are observed to extend significantly above classical predictions.

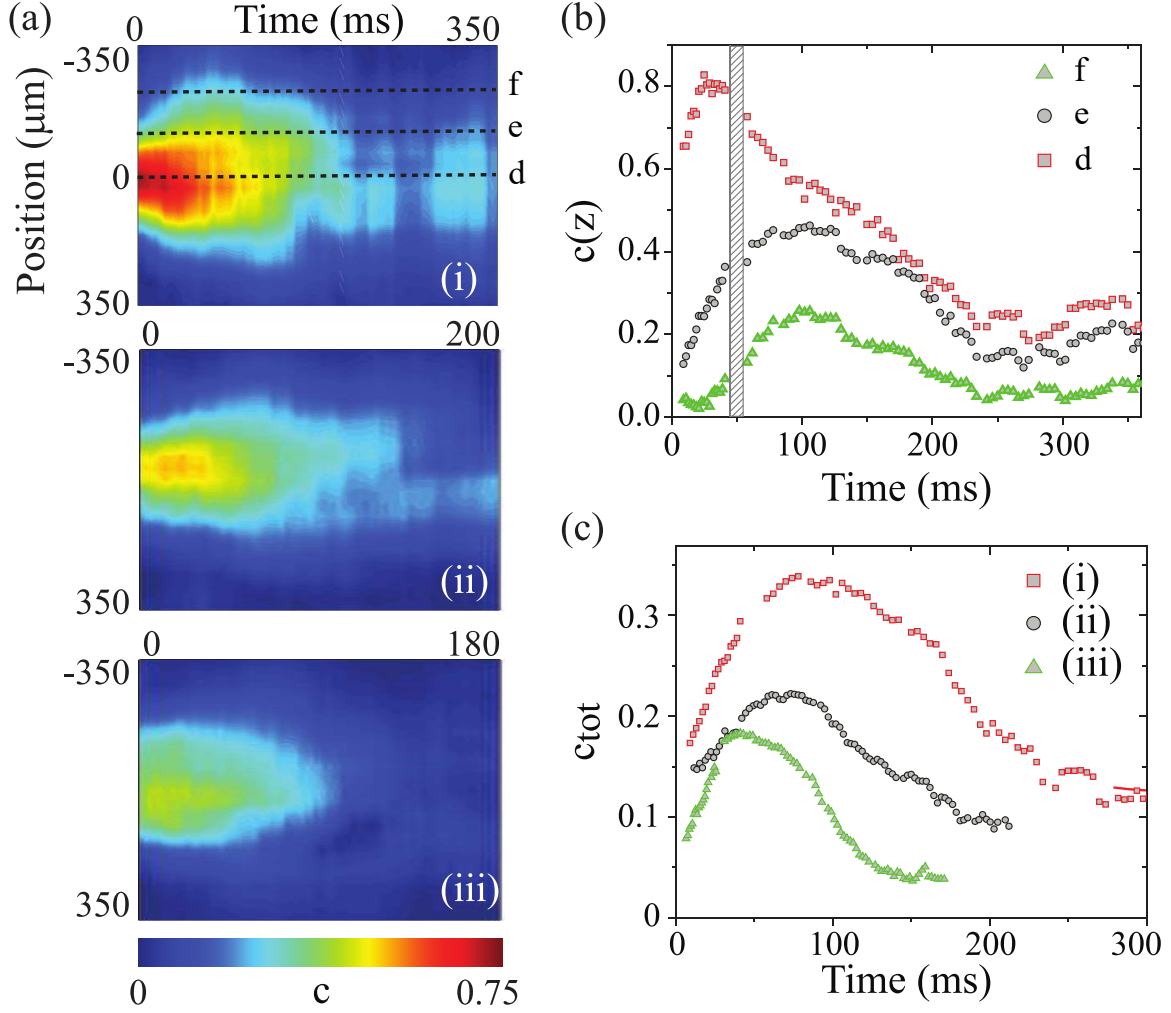


Figure 4.9: (a) Time evolution of S_{\perp} for different domain-wall degrees of coherence, from top to bottom $c_{\text{init}} = 0.71, 0.51, 0.30$ respectively in the cloud center. (b) Time evolution of S_{\perp} in different spatial regions, denoted by the dotted lines (d-f) in (a-i). The dashed box indicates a change in sampling rate to measure both the fast initial rise of coherence and longer relaxation to equilibrium. (c) Time evolution of total ensemble coherence for c_{init} data shown in (a). c_{tot} for each data plot (i-iii) in (a) is calculated by summing transverse spin magnitude for all the bins across the atomic distribution for each time step.

4.4 Discussion

In this section we describe the physical mechanism governing the experimental results presented in the previous sections. We focus on the instability effect observed in the transverse spin dynamics and use numerical solutions of the spin transport equation (Eq. 4.1) to expand the instability study to a parameter space broader than what is available experimentally in our system. These numerical results motivate studying the effect in a broader parameter space in improved experimental configurations.

The experimental results presented in the previous sections show unexpectedly long longitudinal diffusion time scales compared to classical predictions, which are sensitive to the degree of coherence in the domain-wall. To better understand the peculiarity of the observed experimental results we emphasize that the two pseudo-spin states are orthogonal and energetically separated ($U_{12} \simeq h \times 6.8$ GHz); therefore, without a driving field conversions between the states cannot occur. Any internally driven conversions happening are solely due to spin interactions occurring during collisions, which are included in the Boltzmann equation Eq. 4.1 as the spin-torque term $g/\hbar \vec{S} \times \vec{M}(p, z, t)$. Since the two states $|1\rangle$ and $|2\rangle$ are orthogonal and do not coherently interact, the longitudinal spin is in principle expected to diffuse classically. But in spin profiles containing a longitudinal spin gradient, for strong enough spin rotation interactions, longitudinal spin current becomes unstable with respect to transverse perturbations and a conversion of longitudinal spin to transverse spin occurs (see Section 2.3.2). This conversion of longitudinal spin component to transverse spin component leads to an increase in the total amount of coherence in the system. This conversion is only possible, without any external field acting on the two-level system, if coherent interactions occur during binary collisions.

For the instability to occur, the coherent interactions must be strong. That is, the ratio of exchange scattering to elastic scattering, quantified by the ISRE parameter μ , should be greater than one; otherwise elastic collisions will damp the spin currents before they grow large. Also, it should be considered that longitudinal diffusion is very efficient in diffusing a spin gradient; therefore, to be able to observe the signs of the instability experimentally one needs to maintain a strong longitudinal spin gradient. The time for the instability to

grow t_{inst} , must be smaller than the longitudinal diffusion time t_{diff} [55], otherwise the spin structure relaxes to the final equilibrium rapidly before the instability could occur. This requirement sets a limit on the longitudinal spin gradient length scale ℓ with respect to the atomic distribution axial Gaussian half-width w_z . If $\ell \sim w_z$ then the instability cannot grow fast enough to be observed before the longitudinal spin gradient relaxes as the diffusion time is comparable to the time needed for the instability to develop. Therefore, one needs to start with a strong longitudinal spin gradient well above this threshold $\ell < w_z$.

The diffusion coefficient is given by $D = k_B T \tau / m$ for the classical limit of two domains of fully distinguishable components. For our cloud parameters this gives the diffusion time as $t_{\text{diff}} \sim w_z^2 / D \simeq 24$ ms and an estimation for the time for the instability to grow $t_{\text{inst}} \sim \ell^2 / D \simeq 4$ ms for $\ell \simeq 0.4 w_z$ (see [55]). Due to this small t_{inst} we observe the signs of the onset of instability as the growth of the total ensemble coherence almost immediately for all configurations in Fig. 4.9(c). Also, due to our spin texture preparation the initial two-domain longitudinal spin profile has a strong transverse spin component in the domain-wall. Presence of this strong transverse spin component leads to a significant increase in the lifetime of the longitudinal spin domains, with our experimental results revealing $t_{\text{diff}} \simeq 200$ ms for samples with higher degree of initial coherence in the domain-wall *i.e.* in Fig. 4.8(a-i). Therefore, the instability has enough time to grow before the longitudinal spin gradient vanishes.

The instability effect can be explored in more detail by adjusting important experimental parameters: the scattering length a , the initial domain-wall size ℓ and the temperature T . We extend our simulations to a broader parameter space than can be achieved in our current experimental system to explore further the crossover from classical to quantum diffusion, by numerically varying T , a and ℓ . Since the primary signature of the instability is the increase we observe in the total ensemble coherence, we quantify the strength of the instability as the ratio of maximum ensemble coherence to initial coherence, $c_{\text{tot}}^{\text{max}} / c_{\text{tot}}^{\text{init}}$. Figure 4.10 shows the numerical study results of the effects of T , a , and ℓ on the spin instability. Because of near-critical damping and spatially varying density (thus collision rates), the system exhibits a smooth transition between diffusive regimes. Furthermore, since μ is independent

of n , density has little effect on the instability within the range between collisionless and hydrodynamic behaviour.

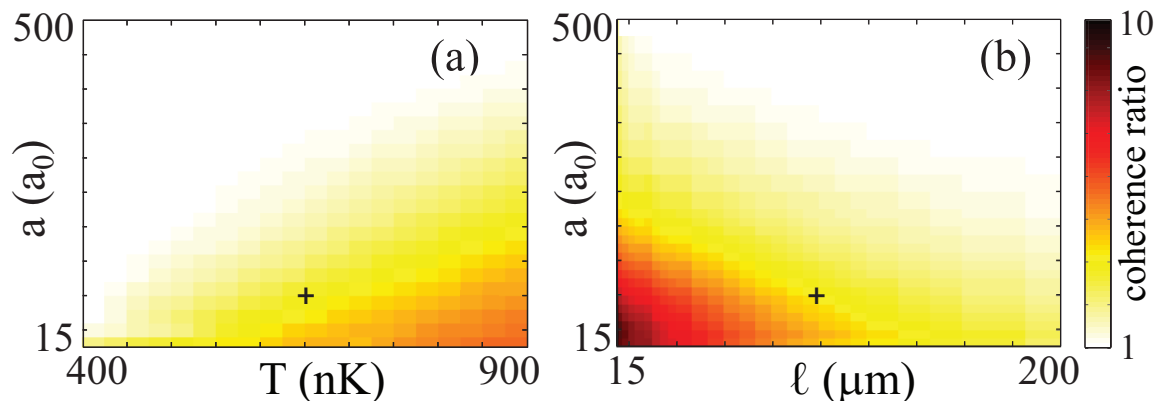


Figure 4.10: Instability onset seen in the ratio of maximum ensemble coherence to initial coherence, $c_{\text{tot}}^{\text{max}}/c_{\text{tot}}^{\text{init}}$, from simulations of Eq. 4.1, plotted logarithmically to highlight instability threshold. We vary a and (a) T or (b) ℓ with other parameters set to conditions of Fig. 4.8(a-ii). Crosses represent the experimental conditions used in this work.

As the region of experimental interest lies between the collisionless and hydrodynamic regimes, no analytic approximation is readily available for the instability criterion, such as was done in [56] (see Section 2.3.2). The most important requirement for the instability is that the ratio of exchange scattering to elastic scattering rates must be approximately greater than 1 (quantified by the ISRE parameter μ [55], ~ 3 for this experiment), lest collisions damp spin currents before they can grow large. If the number of exchange collisions while traversing the domain-wall is large and greater than number of elastic collisions, then a spin crossing the gradient will smoothly rotate from one domain to the other, similar to adiabatic following.

Since $\mu = \omega_{\text{exch}}\tau \propto 1/a$, increasing a diminishes the instability, as collisional damping ($\propto a^2$) grows faster than exchange scattering ($\propto a$). Decreasing T [Fig. 4.10(b)] and increasing ℓ [Fig. 4.10(b)] weakens the effect of the instability, through increasing adiabatic rotation during domain-wall crossing. The effect of temperature on the instability is more complicated and needs more clarification. Since $\mu \propto 1/\sqrt{T}$ increasing T decreases the spin rotation strength. However, the numerical results of Fig. 4.10(a) shows that increasing T makes the instability stronger. To explain this effect we define a dimensionless effective domain-wall width that includes the effect of collisions during a domain-wall crossing as

$\ell_{\text{eff}} = (\ell/v)\omega_{\text{exch}}$, with velocity $v \propto \sqrt{T}$. Here decreasing T increases ℓ_{eff} , which weakens the effect of the instability as seen in Fig. 4.10(b).

4.5 Summary

In summary, the results presented in this chapter reveal that the presence of a transverse spin component in the domain-wall combined with the anisotropy in the longitudinal and transverse diffusion coefficients, lead to the increased longitudinal lifetimes observed in our experiments, relative to classical predictions. The instability couples the longitudinal and transverse spin components, observed as a conversion of the longitudinal spin component to transverse spin. The longitudinal spin diffuses through the region of transverse domain-wall via transverse diffusion, which in turn leads to increased longitudinal domain lifetimes.

Coherent spin dynamics does not occur in a purely longitudinal spin system, since the atoms are in orthogonal spin states and the spin-torque term in the transport equation (Eq. 4.1) always gives a zero value. As a result, collisions are only dissipating scattering events and the problem becomes a classical diffusion of a two-component gas. However, initializing the system with a specific spin profile with a strong transverse spin component in the domain-wall changes the behaviour of the longitudinal diffusion significantly.

In addition, we emphasize that since with our initialized spin profile, the longitudinal spin diffuses through the transverse domain-wall via transverse diffusion, the symmetry and strength of the coherent spin dynamics occurring in the domain-wall region affects the behaviour and time scale of the longitudinal diffusion significantly. In Section 4.3, we discussed the experimental results studying the effect of the strength of the coherent dynamics by controllably adjusting the degree of coherence in the domain-wall region. By tailoring the symmetry of the propagating transverse spin modes via applying an effective inhomogeneous magnetic field, one can further study the effect and manipulate and adjust the longitudinal diffusion time scales and spatial behaviour even further. The results of studying the effect of effective magnetic field inhomogeneities with linear symmetry are presented in Chapter 5.

Chapter 5

Spin diffusion dynamics in inhomogeneous effective magnetic fields

In Chapter 4, we presented the experimental and numerical results of studying the relaxation of a two-domain spin structure to the final equilibrium state in uniform effective magnetic fields. This chapter is focused on studying the effect of inhomogeneous effective magnetic fields of different symmetry in the diffusion dynamics of the two-domain spin structure. We start by giving an overview of different experimental and theoretical studies exploring the effect of effective magnetic field gradients in spin-polarized systems. Next, we describe the procedure used in this work to apply external inhomogeneous effective magnetic fields and the experimental sequence incorporated for studies in this chapter. We proceed by presenting the results for both longitudinal and transverse spin components. Finally, we give a phenomenological description for the observed results when external effective magnetic fields with linear gradients are applied.

5.1 Introduction

In a system with a spin degree of freedom, exploring the effect of magnetic fields on its behaviour is a crucial further step. Also as discussed earlier in Chapter 4, the symmetry and strength of the coherent transverse spin dynamics in the extended domain-wall region affects the behaviour and time scale of the longitudinal diffusion significantly, since the longitudinal spin diffuses through the domain-wall via transverse diffusion and the coherent transverse

dynamics dominate the diffusion dynamics. The coherent transverse spin dynamics are governed by the spin-exchange interactions due to the ISRE during collisions, the outcome of which depends on the orientation of spins contributing in the collisions. The transverse spin orientation at the initial stage of the dynamics is initialized by the spin preparation sequence and then affected by the effective magnetic fields acting on the system as well as the ISRE interactions.

One can manipulate and adjust the longitudinal diffusion time scales and spatial behaviour by controlling the coherent transverse spin dynamics occurring in the system. The effect of the strength of the transverse spin dynamics can be studied by controlling the degree of initial coherence when preparing the initial spin structure. In Chapter 4 the effect of the degree of coherence in the domain-wall region on diffusion dynamics was studied in uniform external magnetic fields; there, the dynamics were mainly governed by the ISRE and the boundary conditions at the edges of the longitudinal spin domains. The results of that study revealed increased longitudinal lifetime of the two-domain spin structure as the degree of coherence in the domain-wall was elevated [92]. Also, the results revealed the pure quantum mechanical origin of the observed modifications to the longitudinal spin domain lifetime, as the diffusion time scale of the longitudinal spin domains showed sensitive dependence on the degree of coherence in the domain-wall (see Section 4.3 for details).

One can further manipulate the transverse spin dynamics by applying nonuniform external magnetic fields. When inhomogeneous external magnetic fields exist there are three different regimes one might consider. If Δ , the root mean square (rms) inhomogeneity of the effective magnetic field, is small compared to the spin-exchange interaction $\Delta \ll \omega_{exch}$, the effect of the external magnetic field gradient is negligible. A large gradient in the external magnetic field $\Delta \gg \omega_{exch}$ leads to fast decoherence of transverse spin, and as a result fast relaxation of the whole spin structure. The most interesting region is where the effect of the external magnetic field gradient is comparable to the effect of the ISRE, $\Delta \sim \omega_{exch}$. The overall transverse spin dynamics in this region exhibit different behaviour depending on the interplay between these two important factors, since these two contributing pieces in the spin interaction can either cooperate or compete.

The ISRE interactions modify all spin components during a collision, while the magnetic field only affects the precession rate and thus orientation of the transverse spin. Also we emphasize that the combined effects of the ISRE and magnetic fields are much more complicated. The outcome of the ISRE interaction depends on the spin orientation of the contributing spins in the exchange collision, while the spin orientations are also affected by the external magnetic field gradients. Therefore, the effect of the ISRE is not constant spatially and temporally. In contrast, the twisting effect of the external magnetic field gradient is constant during the experiment time as long as the effective magnetic field is kept unchanged. In this chapter we extend our studies to explore these effects in detail by modifying the transverse spin dynamics via application of effective magnetic field gradients of different magnitude and symmetry.

5.1.1 Review of ISRE-driven spin dynamics studies in nonuniform magnetic fields

No specific theoretical study has been conducted to investigate the effect of effective magnetic field gradients in a regime directly relevant to our system, but there are similar studies showing the important role the field gradients play in the diffusive spin dynamics. The pioneering studies of the spin dynamics governed by the ISRE go back to the early studies in He systems. In 1992 NMR results of longitudinal spin diffusion studies in dilute ^3He - ^4He mixtures [79], a spontaneous long lived transverse spin signal was detected and attributed to the appearance of a transverse spin domain-wall structure as a manifestation of the Castaing instability. Nunes *et al.* reported that large enough magnetic field gradients suppressed the appearance of these signals. Ragan *et al.* theoretically explored the connection between Castaing's instability and the observed long lived transverse domain-wall structures in longitudinal spin diffusion experiments in an idealized experiment in detail [81]. They investigated the stability of the different possible steady state solutions and the effect of the external field gradients in stabilizing the longitudinal spin current. The results of both studies suggest that external magnetic field gradients suppress the occurrence of Castaing's instability.

In 1994 Dmitriev and Fomin derived a solution to the spin dynamics equation for a normal Fermi liquid in a slightly nonuniform magnetic field in the collisionless regime representing a two-domain spin structure with spatially-separated anti-parallel spins [82]. In a discussion of Fomin’s early work on the formation of these quasi-equilibrium longitudinal domains, Kuklov states that a field gradient is necessary to maintain these domain states [56]. Without such field gradients the domain-like structure becomes unstable against transverse perturbations, revealing that a magnetic field gradient increases the lifetime of the two-domain spin structure. This quasi-equilibrium domain structure slowly relaxes to the final equilibrium due to diffusive processes.

After the observation of spatial separation of pseudo-spin states in trapped ^{87}Rb [52], there was a considerable amount of theory work describing the analogy between pseudo-spin states in two-component trapped quantum gases and spin-polarized spin-1/2 gases [67, 73, 74, 75], explaining the observed separation in [52] as a longitudinal spin-wave oscillation. These studies were followed by a few more theory works expanding the analogy between trapped multi-component gases and spin-polarized systems to a wider range of phenomenon including Castaing’s instability and formation of longitudinal domains [55, 56, 76]. Among these studies, in [76] numerical studies of the dynamics of trapped quantum gases in the hydrodynamic regime were performed for fully transverse initial preparation (after a $\pi/2$ pulse), while the other two works focused on the instability of the longitudinal spin current in spin profiles with large initial longitudinal spin gradients (see Chapter 4 and [57] for details) without particularly focusing on the effect of field gradients.

In the former study [76], Ragan numerically studied the formation of longitudinal spin domains from an initial transverse spin profile (after a $\pi/2$ pulse) for these different regimes and discussed the stability of the lowest lying longitudinal modes (dipole and quadrupole modes). He stated that in the limit of small field gradients and small ISRE interaction strength the field gradient acts as a perturbation of the equilibrium spin state and leads to excitation of transients after a $\pi/2$ pulse with zero-field spin-wave frequency. For larger values of the field gradient and ISRE interaction strength, the evolution of the system after a $\pi/2$ pulse drives the dipole or quadrupole longitudinal spin modes for linear and quadratic

field gradient symmetry respectively. The excited dipole (or quadrupole) longitudinal modes will develop into long-lived longitudinal spin domains, if the ISRE interaction is strong enough for the longitudinal spin current to become unstable and the confined transverse spin component develops into a coherent domain-wall, dividing the domains of the longitudinal spin, which then diffuse through the domain-wall via transverse diffusion. The domain-walls are destroyed for large enough field inhomogeneities $\Delta \gg \omega_{exch}$ due to the decoherence induced by inhomogeneity in the applied field.

None of the aforementioned studies is directly related to our experimental study, but their results motivate us to further study the effect of field gradients on the diffusion dynamics. One of the main differences is the fact that our experimental system lies in between the hydrodynamic and collisionless regime and treating it in one of these limits will not describe the dynamics thoroughly. Thus we conduct numerical simulation of the full semi-classical transport equation to compare with our experimental results. Also we initialize the system with fully polarized longitudinal domains separated by a strong transverse spin domain-wall, in which spin is coherently rotated; therefore, the domain formation from an initial transverse profile is not our concern for studying the effect of field gradients, but we are more interested to further study the consequences of adding field gradients on diffusive behaviour of the initialized longitudinal domains. We numerically study this effect by adding external field gradients in the numerical solution of our full transport equation. We extend our experimental studies to investigate the effect of such field gradients from a more general perspective with a goal of investigating the nature of the effect in more detail.

5.2 Diffusion in a nonuniform effective magnetic field with linear symmetry

To better understand how the effective magnetic field gradients affect the diffusion dynamics of the longitudinal spin domains a few facts should be considered. First, the effect of any differential mechanical force due to the effective external magnetic field is negligible. For instance, a 50 Hz/mm field gradient shifts the relative trap centers by only 0.1 μm , less than 0.1% of the Gaussian half-width of the distribution w_z . Any observed effect is instead due to coherent spin interactions. Also, the effective magnetic field does not directly interact

with the longitudinal spin components. The effective magnetic field is pointing along the longitudinal axis in the Bloch sphere representation; therefore, in the spin transport equation (Eq. 4.1) the effective magnetic field interaction term $U_{\text{diff}} \hat{w} \times \vec{M}_{\parallel}(p, z, t)$ is always zero since the cross product of parallel vectors gives zero. Therefore, any observed modification is expected to be due to interactions with the transverse spin component. In addition, field inhomogeneities are expected to speed up the dephasing of the transverse spin component phase [54], which leads to a faster decay of the initial coherence in the domain-wall and faster diffusion of the longitudinal domains accordingly.

A simple estimate considering all these facts might conclude introducing external nonuniform effective magnetic fields leads to a shorter longitudinal spin domain lifetime. However, our experimental results are in sharp contrast with these predictions. In fact the full picture should be considered so that one can explain the behaviour thoroughly. Although the effective magnetic field does not directly interact with the longitudinal spin component, the interactions in the transverse spin component generates longitudinal spin currents that affect the longitudinal domain diffusion time scales significantly. Our experimental results reveal that propagation in an inhomogeneous effective magnetic field indeed has a noticeable effect on the diffusion dynamics of the two-domain spin structure (Section 5.4.1).

We explore the effect of adding a linear field inhomogeneity in this chapter. As the symmetry of the initial spin profile (longitudinal spin dipole mode) matches the linear symmetry of the effective magnetic field gradient, we can avoid any extra complications due to symmetry mismatch. We expect to see drastically different results for linear field gradients with opposite signs. In principle the added effective magnetic field inhomogeneity generates extra spin dynamics that are not evident in the zero-field propagation data of the previous chapter.

We expect these extra spin dynamics to either increase or decrease the longitudinal spin domain lifetime depending on the longitudinal spin currents initiated in the system as a result of the coherent dynamics. If the coherently generated longitudinal spin currents counteract the diffusive longitudinal spin currents from the domains, longitudinal spin domain lifetime increases. The longitudinal spin domain lifetime decreases if the coherently

generated longitudinal spin currents speed up the frustrated longitudinal currents through the domain-wall.

Our experimental results show slower oscillation frequency of the longitudinal spin domains for positive linear field gradients. Positive field gradients are antialigned with respect to the initial longitudinal spin gradient across the domain wall. In fact for large enough positive field gradients the longitudinal spin domains do not oscillate, but diffuse instead slowly until the longitudinal spin gradient vanishes. Propagation in negative linear field gradients increases the longitudinal domain oscillation frequency significantly and leads to a much faster relaxation of the two-domain spin structure to the final equilibrium state.

For positive field gradients the longitudinal spin domain lifetime characterized by the inverse of damping rate of the two-domain oscillation hits a maximum [Fig. 5.5-(b)], signifying a specific field gradient for which the system reaches the most stabilized longitudinal domain structure. For a trapped gas in the hydrodynamic regime, Ragan *et al.* in Reference [76] derived an equation that relates an equilibrium domain-wall size ℓ_{eq} to a linear field gradient G for steady state time independent domain states [83],

$$G = \frac{1}{\mu M} \frac{\omega_z}{w_z} \left(\frac{\pi/2}{1.1\ell_{eq}/w_z} \right)^3 \omega_z \tau \quad (5.1)$$

with τ the time between collisions. μM is the ISRE parameter, which is the main parameter for the coherent spin dynamics. w_z is the Gaussian half-width of the atomic distribution and ω_z is the axial trap frequency. If the initialized two-domain spin structure domain-wall width ℓ matches ℓ_{eq} for a specific stabilizing field gradient G from Eq. 5.1, the initial two-domain spin structure will have the longest lifetime in that specific field.

5.3 Effective magnetic field

The differential potential experienced by atoms in the two different spin states acts as an effective magnetic field for the pseudo-spin system. By adjusting the differential potential we can add inhomogeneity and study the effect of these effective magnetic field gradients on transport properties of the two-domain spin structure. Trapped atoms experience differential potentials due to the Zeeman shift of the trapping magnetic field and the mean-field shift

due to the density of atoms. These two contributions to the total differential potential can be mutually canceled if properly adjusted (see Section 3.2.1). The regime where these two cancel out is referred to as mutual compensation. All the experiments of Chapter 4 are conducted in this regime, at uniform differential potentials.

Different methods could be used to add inhomogeneities to the differential potential. The differential potential can be adjusted by tuning the cancellation between the magnetic field shift and the mean-field shift experienced by trapped atoms. By moving away from the cancellation magnetic field B_{CS} , we add quadratic magnetic field inhomogeneity. We can also use the Stark laser described in Section 3.2.2 to produce differential optical light shifts that also acts as an effective magnetic field for the pseudo-spin system.

5.3.1 Linear inhomogeneities in differential potential

To add linear effective magnetic field gradients for the experimental studies presented in this chapter, we use an external optical field to create inhomogeneities in the differential potential. This can be done by starting from a uniform differential potential at the cancellation field B_{CS} and applying an additional off-resonant laser field with nonuniform spatial profile. We use the same principle of light shifts already discussed in Section 3.2.2 for preparing our initial spin profile. The oscillating electromagnetic field of an off-resonant laser alters the atomic energy levels via the ac Stark effect, creating an optical differential potential for the pseudo-spin system.

By producing different laser intensity profiles across the atomic distribution, we create differential potentials with arbitrary symmetries. We use this optical method to produce effective magnetic fields with linear gradients. We add an extra optical path using the same off-resonant laser used for spin-state preparation. To create linear gradients in the spatial intensity profiles, we used the method already described and employed in [41] by means of an acousto-optic modulator (AOM). Figure 5.1 shows the apparatus used for this procedure schematically. The procedure involves sweeping a focused laser beam from our Stark laser detuned ~ 3 GHz from the D_2 excited-state transition (Fig. 3.2), while controlling the intensity of the laser beam during the sweep. By modulating the frequency and amplitude of the AOM rf drive signal at modulation rates of several kHz, we create time-averaged

linear gradients in optical intensity across the atomic distribution along the axial direction. Since the modulation rate is significantly higher than all the other experimental time scales, the time-averaged optical potential can be viewed as a static differential potential.

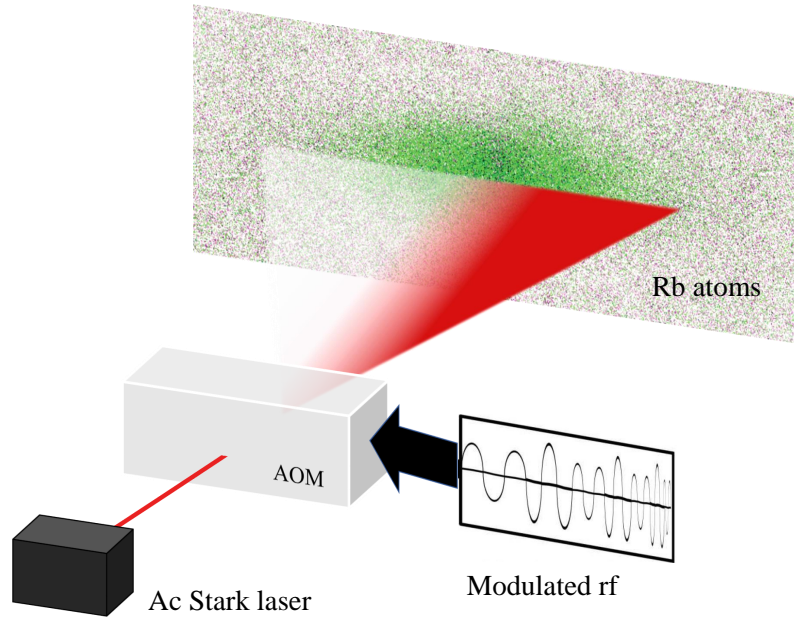


Figure 5.1: Schematic of the apparatus used to create linear gradients in the differential potential, showing the time averaged laser intensity profile applied on the atomic distribution.

Figure 5.2 shows the uniform differential potential (red) created by the mutual compensation scheme along with a negative (blue) and a positive (black) linear gradient produced using the aforementioned method. U_{diff} is measured using a $\pi/2 - \pi/2$ Ramsey interferometer by varying the $\pi/2$ pulse separation for times up to 10 ms. The number of atoms returning to the $|1\rangle$ state is measured after the full Ramsey sequence. To obtain spatially resolved data, the atomic cloud is divided into axial bins and each bin is fitted to a sinusoid to extract the local differential potential energy from the Ramsey oscillation frequency. The value of the linear gradient is extracted from these spatially resolved U_{diff} data sets by performing a linear fit as shown by the dashed (dotted) line for the positive (negative) linear gradient. The positive linear gradient is extracted as $G \simeq 110$ Hz/mm for the U_{diff} presented in Fig. 5.2.

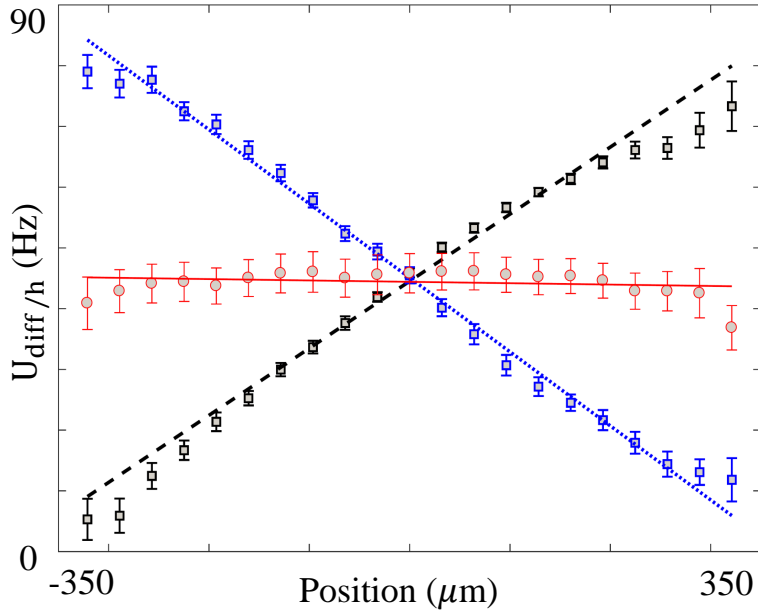


Figure 5.2: U_{diff}/h for uniform (red), negative (blue) with $G \sim -121$ Hz/mm and positive (black) with $G \sim 110$ Hz/mm linear gradients across the atomic distribution. dashed (dotted) line shows a linear fit for the positive (negative) gradient. The linear fit is used to extract the linear gradient G across the atomic distribution. The solid line shows a linear fit for the uniform differential potential. U_{diff} is measured by Ramsey spectroscopy.

5.4 Longitudinal diffusion results in applied linear field gradients

Figure 5.3 depicts the typical experimental sequence used for studying the effect of linear field gradients on diffusion of the two-domain spin structure. We initialize our spin profile into the two-domain anti-parallel longitudinal spin texture as usual in the cancellation field with gradient $G \sim 0$. Following the spin-state initialization we turn on the nonuniform U_{diff} laser with a known value of linear gradient $G \neq 0$ across the atomic distribution and keep the extra optical potential on during the evolution of the spin profile towards equilibrium. By adjusting the time-averaged laser intensity profile, we controllably adjust the sign and the magnitude of the linear gradients to cover a wide range of linear inhomogeneities and

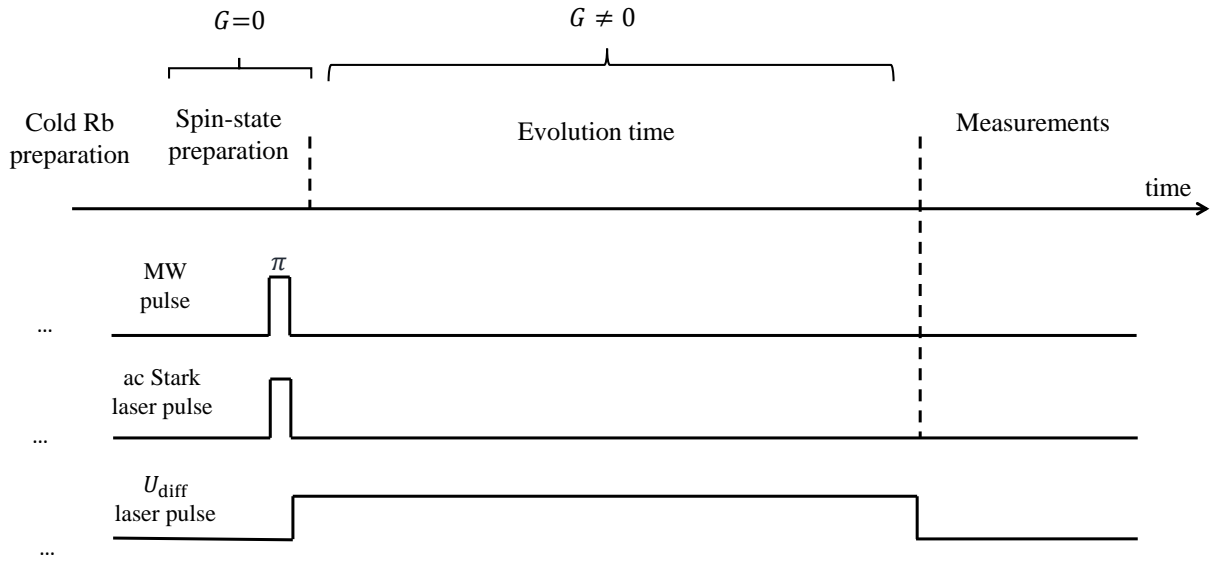


Figure 5.3: Experimental sequence for studying the effect of linear field gradients on diffusion of the two-domain spin structure, showing the timing and duration of all the different applied fields. Each sequence begins with the initial spin-state preparation into a two-domain anti-parallel longitudinal spin texture in $G \sim 0$. Following the initialization sequence in a uniform differential potential, the nonuniform U_{diff} laser pulse is applied to create linear field gradients $G \neq 0$ during the relaxation of the spin structure to its final equilibrium. After the evolution time, the longitudinal spin component is destructively measured. The experimental sequence is repeated for each value of the evolution time. The transverse spin component is measured using the Ramsey spectroscopy method.

study the relaxation of the two-domain spin structure via measuring the longitudinal and transverse spin dynamics for each value of G .

5.4.1 Longitudinal domain dipole oscillation

Figure 5.4(a-c) represents typical experimental results for the longitudinal spin dynamics as the two-domain spin structure relaxes to the final equilibrium state for cancellation field gradient $G \sim 0$ (middle), positive $G > 0$ (right) and negative $G < 0$ (left) linear effective magnetic field gradients. The contrast in the diffusion dynamics time scales is clearly evident in these results. Figure 5.4(c) shows that propagating in an effective magnetic field with a positive linear gradient increases the longitudinal spin domain lifetime noticeably. On the contrary, propagation in an effective magnetic field with negative field gradient increases the longitudinal spin diffusion and results in much faster relaxation of the longitudinal spin domains [Fig. 5.4(a)]. We discuss later in this section that the observed contrast in the behaviour for different applied linear magnetic field gradient signs is due to the differences in the transverse spin dynamics excited in the system and the presence of the initial longitudinal spin domains.

As described in the previous chapter to explore the effect of these added inhomogeneous magnetic fields on the longitudinal spin diffusion time scales, we calculate the dipole moment of the longitudinal spin domain oscillations to isolate the dynamics of the spin dipole mode. Exponentially damped sine waves are fitted to the dipole moment oscillations to determine the frequency f and damping rate Γ of the longitudinal spin domain oscillations [Fig. 5.4(d)]. It should be noted that the domain oscillations are not purely sinusoidal nor precisely exponentially damped, since there are multiple dynamical effects altering the oscillations, but this analysis gives a reasonable estimate of the characteristic time scales.

Figure 5.5 shows the extracted frequency f [Fig. 5.5(a)] and damping rate Γ [Fig. 5.5(b)] of the dipole moment oscillations calculated for longitudinal spin evolution data for different positive and negative linear effective magnetic field gradients. It is seen that both the oscillation frequency and the damping rate hits a minimum at around $G \sim 25$ Hz/mm.

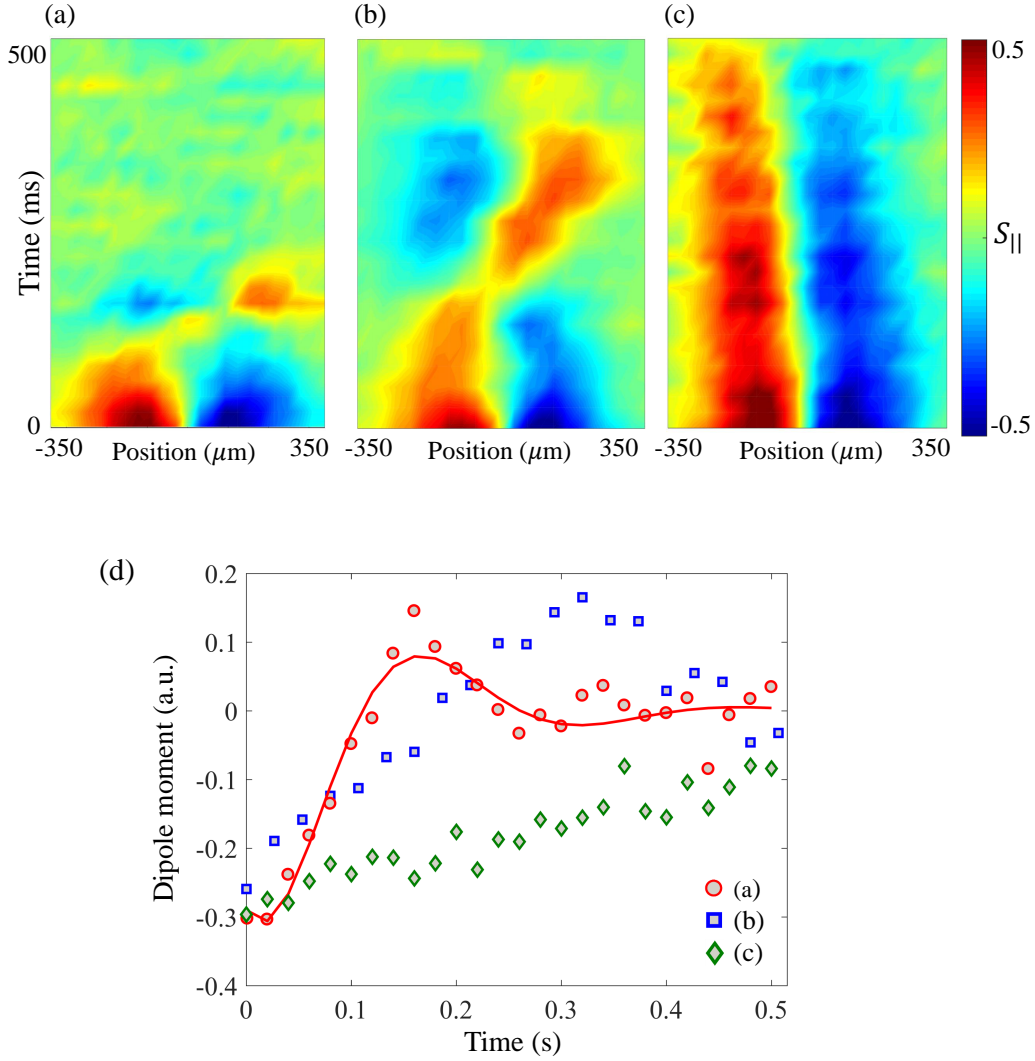


Figure 5.4: (a)-(c) Spatiotemporal evolution of the longitudinal spin component $S_{||}$ in negative $G \simeq -20$ Hz/mm (a), cancellation field $G \sim 0$ Hz/mm (b) and positive $G \simeq 24$ Hz/mm (c) linear effective magnetic field gradients. The initial longitudinal domains undergo dipole oscillation in $G \sim 0$ Hz/mm in (b). Propagation in an effective magnetic field with negative field gradient in (a) increases the longitudinal domain oscillation frequency and also leads to much faster relaxation of the longitudinal spin domains, while propagating in an effective magnetic field with a positive linear gradient in (c) increases the longitudinal spin domain lifetime noticeably, compared to the uniform magnetic field results in (b). (d) Dipole moment time evolution calculated for longitudinal domain oscillations in (a)-(c). The solid line shows a representative exponentially decaying sinusoidal fit for (a). Frequency f and damping rate Γ of the longitudinal domain oscillations are extracted from these fits.

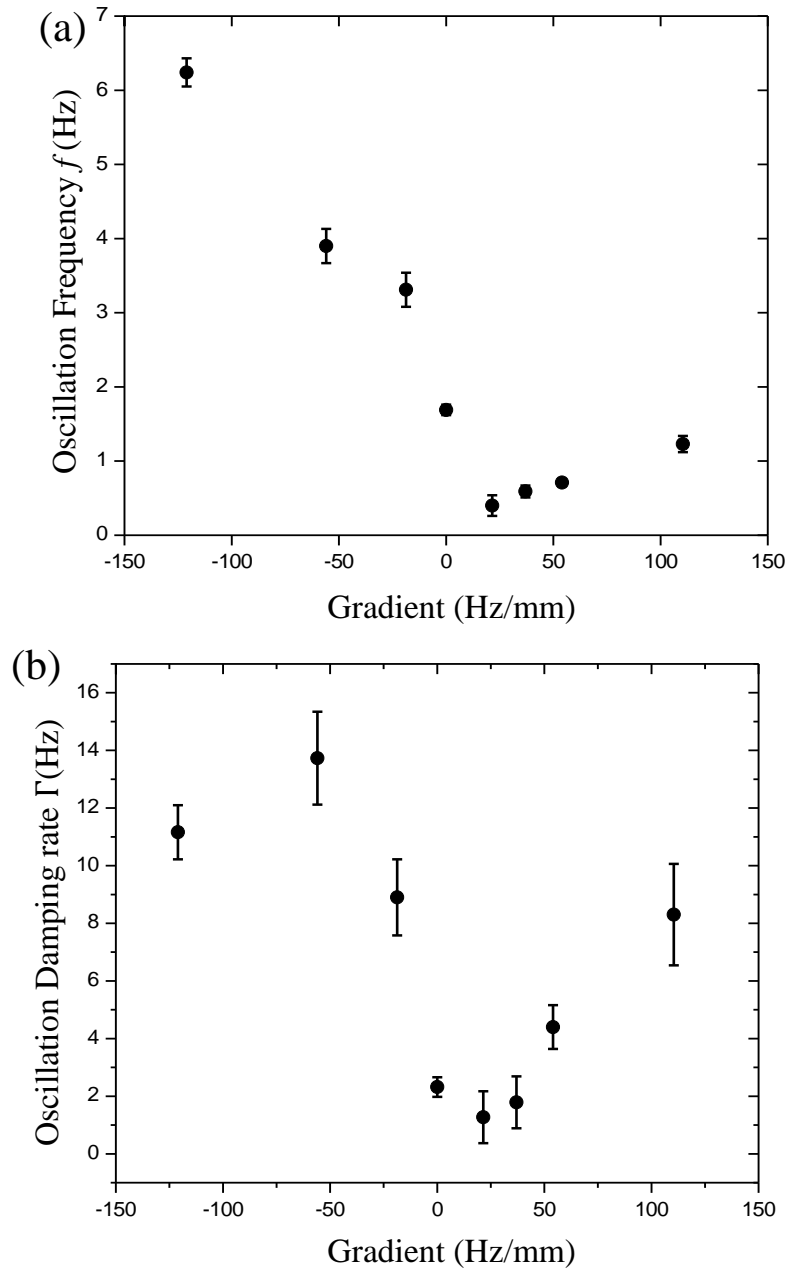


Figure 5.5: (a) Dipole moment oscillation frequency f and (b) damping rate Γ for positive and negative linear field gradient G . Error bars correspond to fit uncertainties for dipole moment oscillations [Fig. 5.4(d)].

Although this analysis inevitably mixes the oscillation frequency with the damping rate, it still manages to produce a reasonable estimate of the domain stabilization effect.

The oscillation frequency of the longitudinal domains, f , decreases for small and intermediate positive linear field gradients, hitting a minimum at around $G \sim 25$ Hz/mm. The oscillation frequency is decreased significantly and the longitudinal spin domains practically do not oscillate [Fig. 5.4(c)]. For negative field gradients f increases and approaches the trap oscillation frequency f_{axial} for the large negative field gradient limit. For positive field gradients extracting a frequency while no oscillation is actually occurring might seem unreasonable, but the main goal is to show the contrast in the two-domain relaxation behaviour for positive and negative field gradients. We emphasize that the sine fits to dipole moment data in positive field gradients are dominated by the initial transient currents, rather than real oscillations.

The damping rate of the dipole moment oscillations Γ gives an estimate of the lifetime of the longitudinal domains. Γ decreases with increased positive linear field gradients in the small field gradient range, but as the inhomogeneity is increased further, Γ increases; since larger inhomogeneities induce rapid decoherence and lead to faster relaxation of the spin texture to the final equilibrium. In conclusion, there is a range of positive linear field gradients in which the effect of applying inhomogeneous effective magnetic fields leads to longer lifetimes for the longitudinal spin domains. Negative linear field gradients increase the damping rate of the oscillations Γ significantly, leading to much faster relaxation of the longitudinal spin domains compared to results in $G \geq 0$.

As explained in Section 5.2, if the initialized two-domain spin structure domain-wall width ℓ matches ℓ_{eq} for a specific stabilizing field gradient G from Eq. 5.1, the initial two-domain spin structure will have the longest lifetime in that specific field. According to the experimental results for the domain dipole moment damping rates (Fig. 5.5(b)), we conclude that the domain-wall width ℓ of our initial two-domain longitudinal spin profile matches a field gradient $G \sim 25$ Hz/mm [Fig. 5.5-(b)], for a stable domain structure. Since Eq. 5.1 was derived with the assumption that the system lies in the hydrodynamics regime, our

experimental result cannot be compared directly to the predictions for the stabilizing field gradient from Eq. 5.1.

5.4.2 Transverse spin dynamics in the domain-wall

We investigate the nature of this contrast in the longitudinal diffusion dynamics time scales in effective magnetic fields with linear gradients by studying the dynamics of the transverse spin component. Figure 5.6(a-c) represents the full dynamics of the transverse spin component in an effective magnetic field with positive linear gradient $G \simeq 24$ Hz/mm, showing the spatially-resolved transverse spin amplitude dynamics across the atomic ensemble in Fig. 5.6(a) and the evolution of the transverse spin phase in the domain-wall region in Fig. 5.6(b). Figure 5.6(c) shows that at the initial stage of the dynamics the ensemble cloud coherence, calculated as the total transverse spin magnitude across the atomic distribution increases. However, this increase is suppressed compared to the experimental results observed in flat field ($G \sim 0$) discussed in Chapter 4 [see Fig. 4.9(c)].

The coherent oscillation of the transverse spin component phase in Fig. 5.6(b) is a new feature observed in the transverse spin component dynamics data, which is due to applying positive effective magnetic field gradients. The propagation of this coherent transverse spin mode is the key to increased longitudinal domain lifetimes. It has been known that magnetic field inhomogeneities lead to excitation of transverse spin dynamics (spin waves) [41, 52, 67, 75]. Here, the added positive linear field gradient combined with the effect of the ISRE excite transverse spin oscillation modes in the domain-wall region. These transverse spin component oscillations are coherence-preserving transverse spin dynamics, leading to less overall dephasing over time. Therefore coherence times are longer compared to cases where these coherent spin oscillations are absent or weaker, for the same value of μ . It is crucial that the exchange interactions are strong enough, otherwise the dephasing due to external field gradients becomes dominant and the coherence decays rapidly, leading to fast relaxation of the two-domain, as seen in the longitudinal diffusion results for large field gradients in Fig. 5.5(b).

Figure 5.6(d-f) represents the transverse spin component evolution data in an effective magnetic field with negative linear gradient. It is evident that in this case the coherence

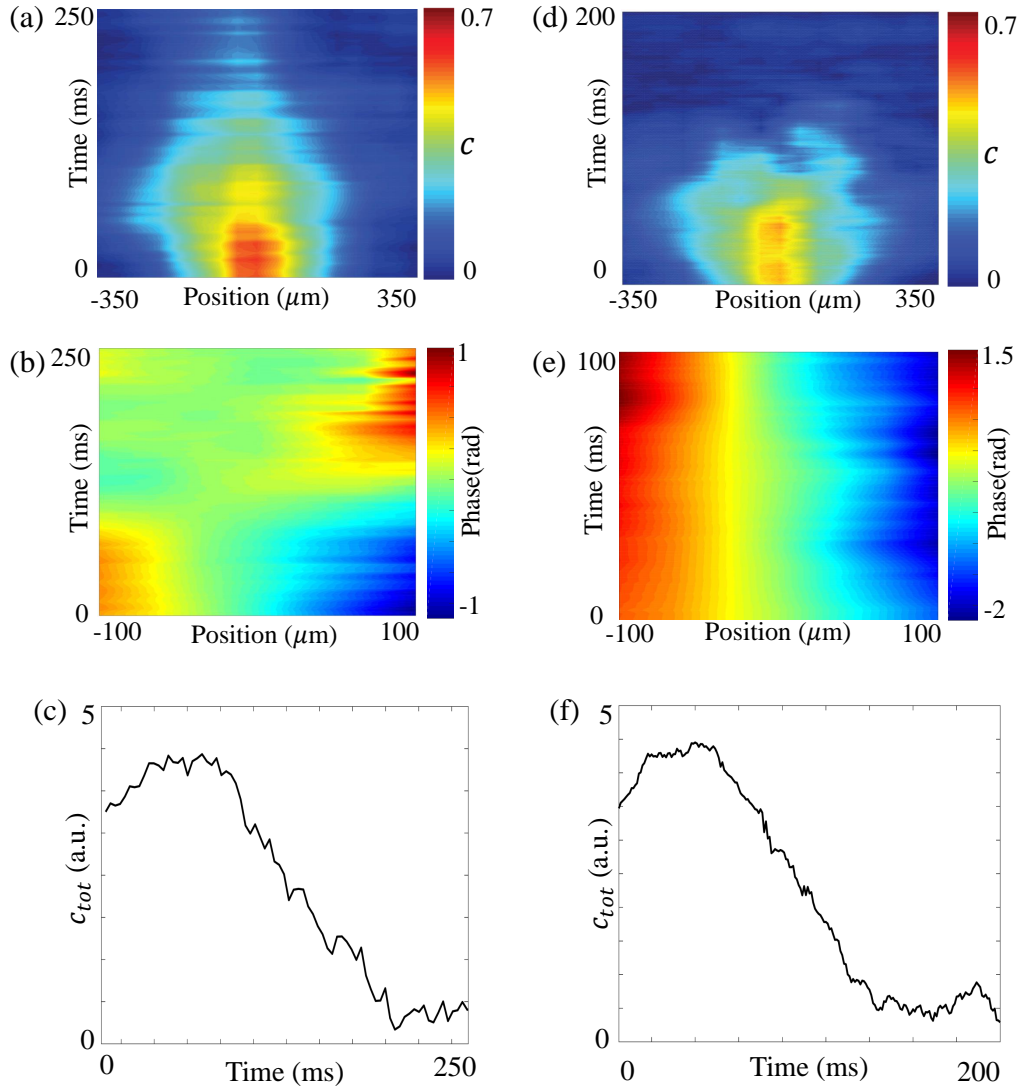


Figure 5.6: Time evolution of the transverse spin component S_{\perp} for linear magnetic field gradient $G \simeq 24$ Hz/mm (a-c) and $G \simeq -20$ Hz/mm (d-f). Spatially resolved time evolution of the transverse spin magnitude (a/d) and transverse spin phase in the domain-wall region (b/e) for positive/negative G respectively. Time evolution of the total ensemble coherence for $G \simeq 24$ Hz/mm (c) and $G \simeq -20$ Hz/mm (f).

decays much faster, as seen in Fig. 5.6(d,f). The other important difference is the evolution of the transverse spin phase in the domain-wall region presented in Fig. 5.6(e). The transverse spin component phase is clearly not oscillating, but increasing for each lobe, indicating that the system is getting more out-of-phase. This is also the reason for the fast coherence decay, since applying the negative field gradient to the two-domain spin structure with the specific initial transverse phase profile, induces fast dephasing of the transverse spin phase and subsequent loss of coherence in collisions. We will discuss this effect in more detail and compare the experimental results with numerical results from the solution of the quantum Boltzmann equation (Eq. 4.1) in Section 5.5.

The contrast in the two different phase evolution data for positive and negative linear gradient can be seen more clearly in Fig. 5.7 and Fig. 5.8. For the positive linear gradient a coherent oscillation of the phase is seen in the domain-wall region, which preserves coherence for longer times. In the negative linear gradient data such behaviour is absent and the transverse spin tends to grow further out of phase, accompanied by a much faster decay of coherence in the domain-wall.

Figure 5.9(a-b) shows the initial stage of the transverse spin dynamics for uniform external field $G \sim 0$ [Fig. 5.9(a)] along with negative external linear field gradient data $G < 0$ [Fig. 5.9(b)]. For $G < 0$ the transverse spin component is mainly confined in the domain-wall region, and the rise in the total transverse spin component magnitude across the cloud is suppressed compared to the transverse spin component evolution in $G \sim 0$. To quantify the effect of suppression of Castaing's instability, *i.e.* conversion of longitudinal spin component to transverse spin, we extract the ensemble coherence ratio $c_{\text{ratio}} = c_{\text{tot}}^{\text{max}}/c_{\text{tot}}^{\text{init}}$ from the transverse spin component evolution data. The results are summarized in Fig. 5.10, representing a decrease of the initial rise observed in the transverse spin component magnitude as linear effective magnetic fields are added.

The dynamics of the transverse spin component has already been studied both theoretically and experimentally in different regimes [40, 52, 54, 67, 73, 74, 75]. Although describing the differences between the longitudinal spin diffusion time scales for positive and negative linear magnetic field gradients as a consequence of the excited transverse spin dynamics is

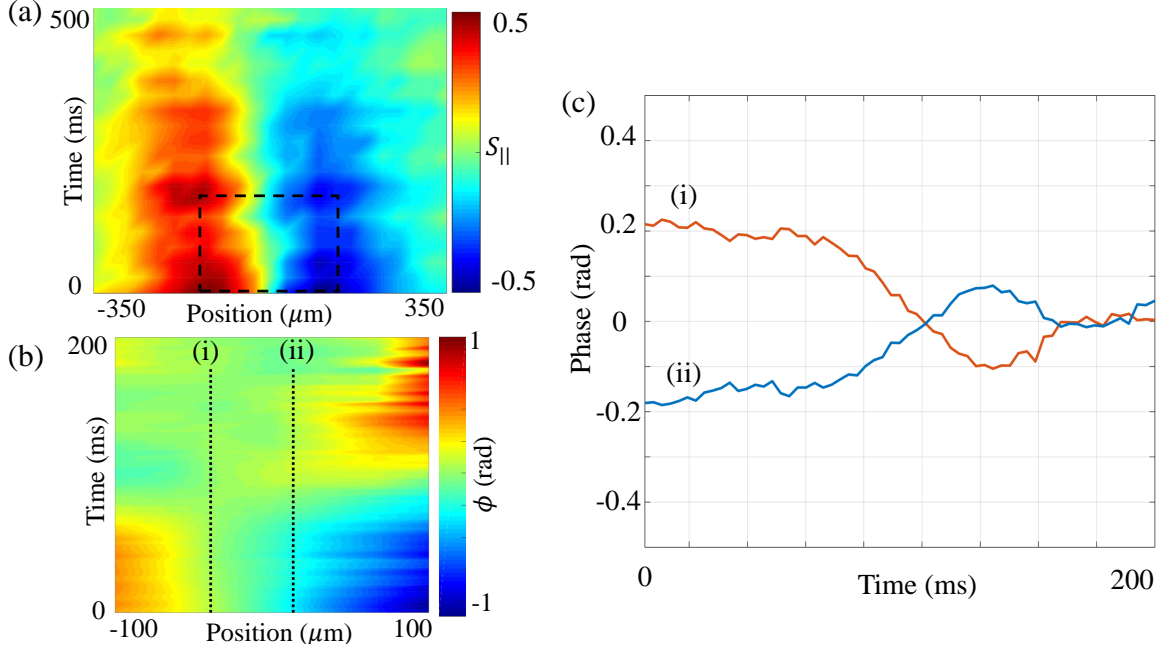


Figure 5.7: (a) The stabilized longitudinal domains for positive linear gradient $G \simeq 24$ Hz/mm. (b) The spatiotemporal evolution of the transverse spin orientation ϕ for the domain-wall region marked with the dashed square in (a). (c) The time evolution of ϕ highlighted for two locations in the domain-wall marked with dotted lines (i) and (ii) in (b). The transverse spin orientation exhibits dipolar spin oscillations in the domain-wall region.

correct, it is too simple to be able to explain the effect thoroughly. The sign of the applied linear field gradients only reverses the symmetry of the excited transverse spin modes and no other major difference is expected. Therefore, this significant difference observed in the longitudinal diffusion time scales needs more clarification, since it can not originate solely from the different transverse spin oscillation symmetries. The significant difference observed between the diffusion dynamics in positive and negative linear field gradients is mainly due to the initial longitudinal spin profile. The combined effects of all these contributions eventually result in the differences observed in the longitudinal spin diffusion time scales. We explain this point further in the discussion part of this chapter.

5.5 Discussion

It is important to note that the specific initial longitudinal domain profile is crucial to observe such contrast in the longitudinal spin diffusion time scales for positive and negative linear field gradients, since in a fully transverse initial spin state with no longitudinal spin

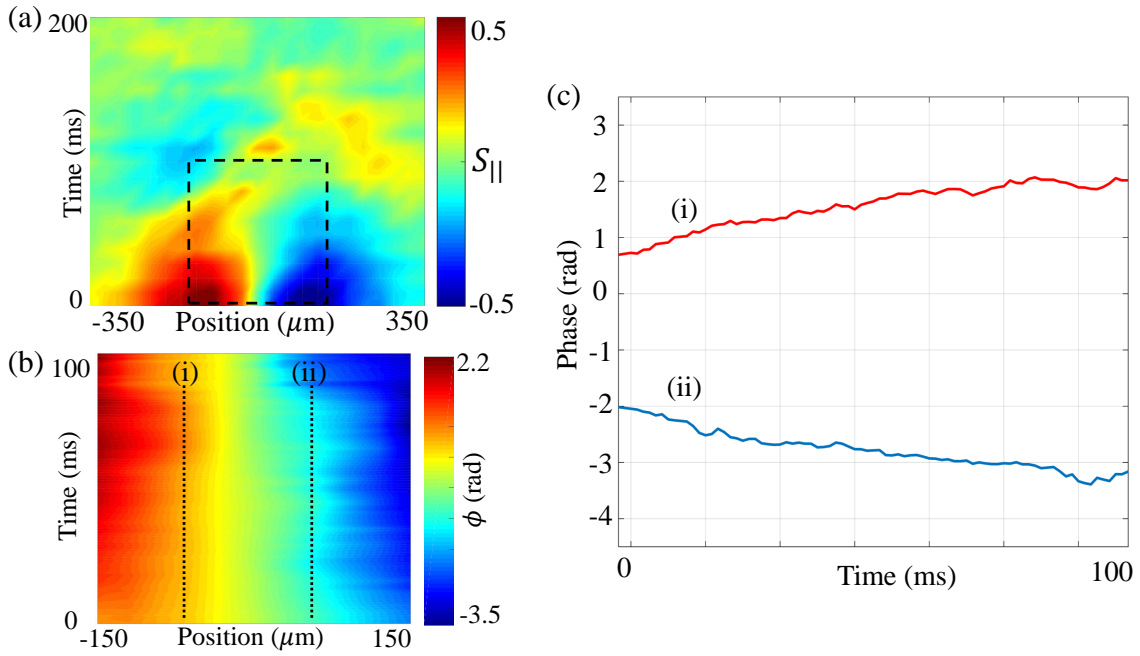


Figure 5.8: (a) The fast decaying longitudinal domains for negative linear gradient $G \simeq -20$ Hz/mm (b) The spatiotemporal evolution of the transverse spin orientation ϕ for the domain-wall region marked with the dashed square in (a). (c) The time evolution of ϕ highlighted for two locations in the domain-wall marked with dotted lines (i) and (ii) in (b). The transverse spin orientation becomes further out of phase with time across the domain-wall, in contrast to the dipolar spin oscillations observed for positive linear gradients in Fig 5.7(c).

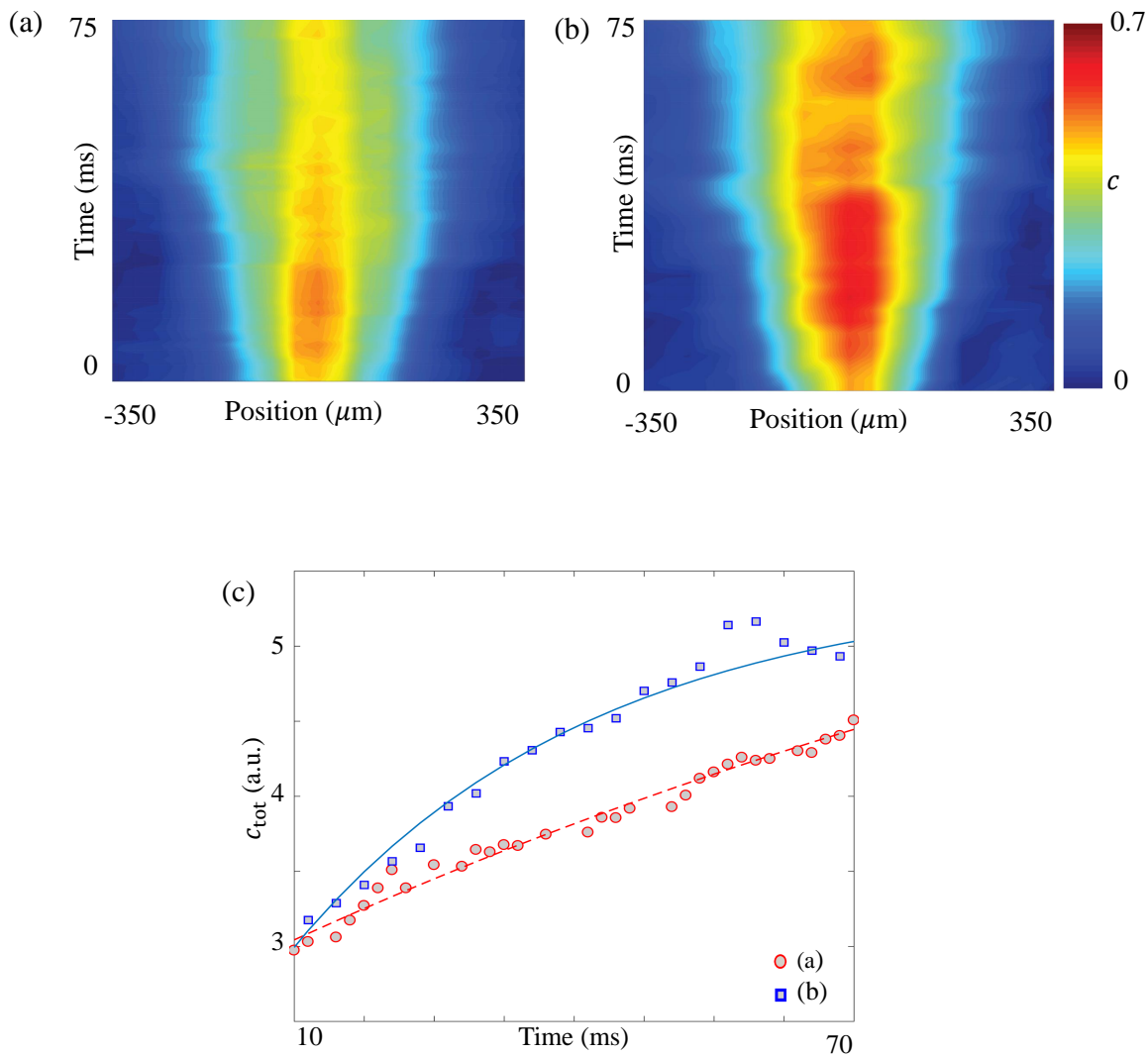


Figure 5.9: The initial stage of the spatiotemporal dynamics of the transverse spin magnitude $c(z,t)$ for negative field gradient $G \sim -21$ Hz/mm (a) and uniform magnetic field $G \sim 0$ Hz/mm (b). (c) The time evolution of the total ensemble coherence c_{tot} for (a) and (b), showing the suppression of the initial rise in $c_{\text{tot}}(t)$ for $G < 0$ compared with $G \sim 0$ Hz/mm (solid/dashed line are a guide to eye).

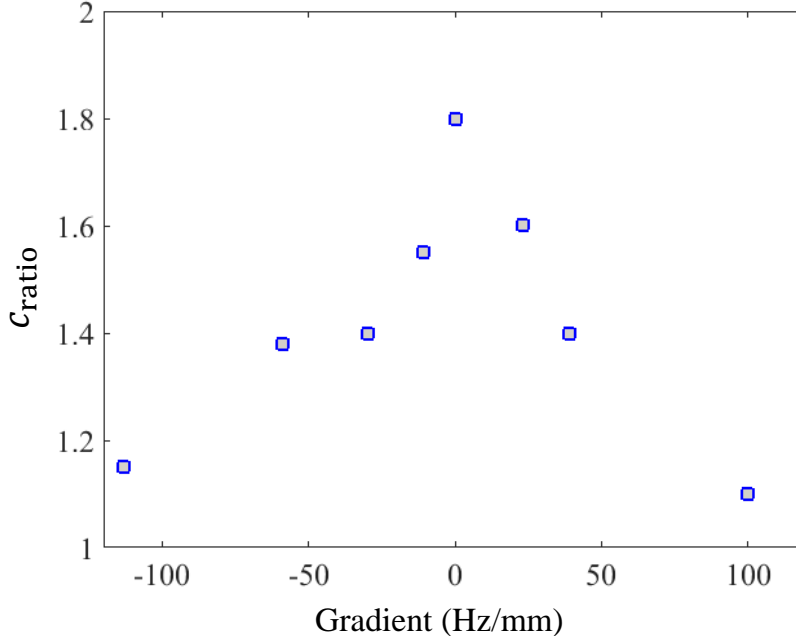


Figure 5.10: $c_{\text{ratio}} = c_{\text{tot}}^{\text{max}}/c_{\text{tot}}^{\text{init}}$ decreases as linear field gradients G are applied.

domains, the sign of the effective magnetic field gradients only reverses the symmetry of the generated modes without changing the general behaviour. Basically, the specific initial longitudinal two-domain spin profile breaks the rotational symmetry in the spin dynamic problem by introducing a specific spin orientation. In other words an initial longitudinal spin domain profile with a distinct orientation supports the propagation of specific modes of coherence-preserving transverse dynamics, which in turn increases the longitudinal spin domain lifetime, via canceling longitudinal spin currents from the longitudinal domains. If we reverse the initial longitudinal spin domain symmetry, the role of positive and negative linear field gradients in stabilizing the longitudinal domains are exchanged.

To better understand the discussion, qualitative simulation results of the quantum Boltzmann equation (Eq. 4.1) are presented in Fig. 5.11 for atomic clouds with similar parameters a , n and T as the atomic clouds experimentally studied here. The initial longitudinal domain orientation is reversed spatially between Fig. 5.11(a) and Fig. 5.11(b) while all other aspects (ℓ and initial phase profile) are unchanged. In Fig. 5.11(b) it is seen that the same positive linear gradient that increases the lifetime of the longitudinal two-domain spin structure in Fig. 5.11(a) leads to faster longitudinal diffusion and decreases the longitudinal spin-domain

lifetime. These simulations are conducted to compare the qualitative behavior and are not quantitatively accurate.

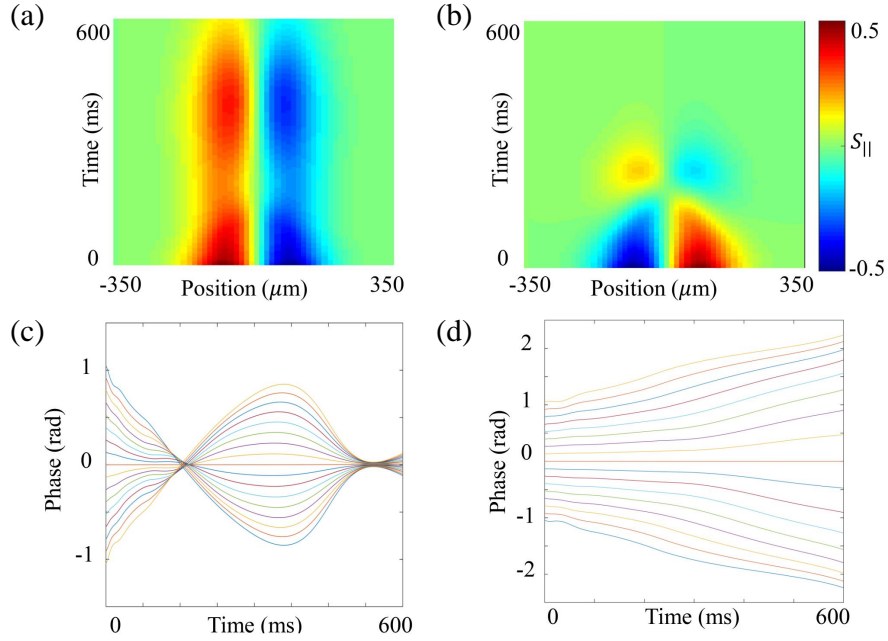


Figure 5.11: Simulation results for longitudinal domain dynamics (a-b) and transverse spin phase (c-d) for the same positive field gradient G . The initial longitudinal domain orientation is reversed between (a-c) and (b-d), while the initial transverse spin helix is unchanged. The same external field gradient stabilizes the longitudinal domains for (a), while it leads to faster decay of the longitudinal spin domains in (b). The contrast in the time evolution of the transverse spin phase can be seen in (c) and (d). The transverse spin phase exhibits oscillations in (c), while it grows further out of phase for (d).

Figure 5.12 schematically depicts the situation when positive [Fig. 5.12(b)] and negative [Fig. 5.12(c)] field gradients are applied. In a system with a nonuniform longitudinal spin profile, longitudinal spin currents from the domains tend to relax the longitudinal gradient and the domains. For positive linear gradients, the excited transverse spin dynamics results in generation of longitudinal spin currents that counteract the diffusive longitudinal spin currents in the system. As a result the total longitudinal spin current in the system becomes effectively negligible. Also, the spread in the transverse spin component phase is effectively unwrapped, leading to a coherent oscillation of the transverse spin orientation, preserving the coherence in the domain-wall for longer. Both effects lead to increased longitudinal domain lifetimes, as our experimental results show.

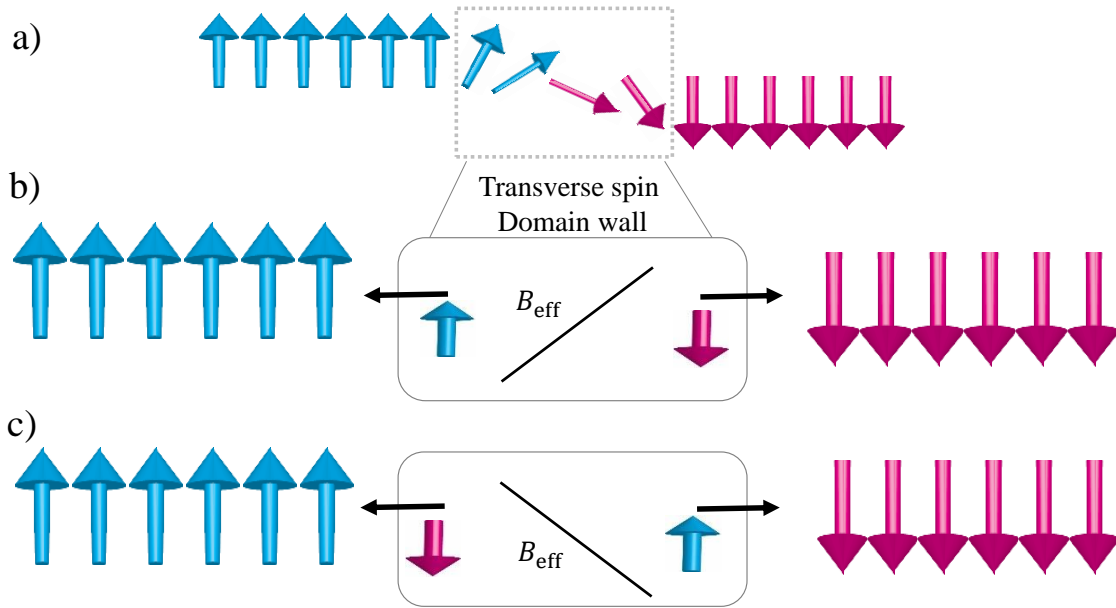


Figure 5.12: (a) Schematic representation of the two-domain spin structure. The spin vector is rotated across the domain-wall such that in the middle of the domain-wall the spin is purely transverse. (b) For this specific initial longitudinal domain orientation - positive linear gradient in the effective magnetic field - the ISRE-driven longitudinal spin currents are generated from the transverse domain-wall region towards the longitudinal domains of the same orientation. Due to this effect the total longitudinal current is decreased significantly. (c) For this specific initial longitudinal domain orientation - negative linear gradient in the effective magnetic field - the ISRE-driven longitudinal spin currents are generated from the transverse domain-wall region towards the longitudinal domains of the opposite orientation, which adds to the diffusive longitudinal spin currents from the domains. Due to this effect the longitudinal domains decay rapidly. Diffusive longitudinal spin currents from the longitudinal spin domains are not shown here.

For negative field gradients the coherently excited longitudinal spin currents are towards the longitudinal domains of opposite sign, schematically depicted in Fig. 5.12(c). These longitudinal currents generated as a result of the coherent transverse spin interactions in the domain-wall flow in the same direction as the diffusive longitudinal spin currents from the longitudinal domains; therefore, the longitudinal diffusion effectively speeds up. Also, the added effective magnetic field tends to force the transverse spin phase to grow further out-of-phase, in such a way that the ISRE is not efficient in unwrapping the out-of-phase spins. This leads to faster decay of the transverse spin magnitude. As a result the domain-wall decays faster, leading to faster longitudinal spin diffusion. In this case no coherence-preserving transverse spin oscillations occurs.

The experimental results for negative field gradients can be compared to the study of the diffusion dependence on domain-wall coherence discussed in Chapter 4 as well (see Section 4.3 for details). In those studies we initialize the system with lower coherence using fast light-induced dephasing in the domain-wall and study the impact of the degree of initial coherence in the domain-wall on the subsequent longitudinal diffusion dynamics. The results showed that the domain lifetime decreases as the domain-wall coherence is lowered. Here, we start with the same initial coherence in the domain-wall for all experiments, but the presence of the effective magnetic field with negative gradients and the specific initial longitudinal domain orientation induces fast decay of the domain-wall. The fast decay of the domain-wall is due to the rapid dephasing of the transverse spin component and the subsequent loss of coherence during collisions. Therefore, when negative field gradients are applied the longitudinal spin diffusion speeds up in two ways. Firstly, the coherently excited longitudinal currents increase the overall diffusing longitudinal currents in the system. Secondly, the coherence in the domain-wall decays rapidly, leading to faster diffusion of the longitudinal domains as a consequence.

5.6 Summary

In summary, in this chapter we studied the diffusion of a two-domain spin structure when inhomogenous external magnetic fields with positive and negative linear gradients are

applied. The longitudinal spin component diffuses through the transverse spin domain-wall, and the ISRE-dominated transverse spin dynamics occurring in the domain-wall region modifies the longitudinal diffusion noticeably. In this chapter, we manipulated the ISRE-dominated transverse spin dynamics by applying nonuniform external magnetic fields. We studied how these added inhomogeneous fields affect the relaxation of the two-domain spin structure to the final equilibrium state.

We observed a sharp contrast in the longitudinal domain relaxation time when positive and negative effective magnetic field gradients are added (Fig. 5.4). For positive linear field gradients our results revealed that this modification leads to further stabilization of the longitudinal spin domains and longer longitudinal domain lifetimes. On the contrary, for negative field gradients the results showed an increase in the longitudinal spin diffusion and rapid decay of the longitudinal spin domains. In the positive field gradients we observed a dipolar transverse spin oscillation confined in the domain-wall region (Fig. 5.7). This coherent oscillation of transverse spin phase is a key to increases observed in the longitudinal spin domain lifetimes. This coherent oscillation of the transverse spin phase was absent when negative effective field gradients were applied (Fig. 5.8).

We also observed a suppression of Castaing's instability when linear gradients of both signs are applied (Fig. 5.10). Finally, we presented a phenomenological description for the observed effects, discussing how the coherently generated longitudinal spin currents in the system lead to the stabilized domains for positive field gradients and faster relaxation for negative field gradients.

Chapter 6

Conclusion and future direction

In this work, we studied spin transport in a weakly interacting trapped Bose gas in the cold-collision regime. Although systems in the cold-collision regime are non-degenerate, they behave far from a classical gas due to quantum-symmetry requirements during binary collisions between atoms. This effect leads to a spin rotation of the colliding spins (the ISRE), due to spin-exchange interactions during collisions. The ISRE indeed modifies transport properties of a system in the cold-collision regime, which motivated the transport studies presented in this thesis. We studied the relaxation dynamics of a two-domain longitudinal spin structure to the final equilibrium state, and explored the effect of the ISRE on the spatiotemporal behaviour of the diffusion dynamics.

We started this thesis by presenting the theoretical description of the system relevant to this work. In Chapter 2, we derived the transport equation that describes the dynamics in this regime, which includes the so-called ISRE interaction as a spin-torque term. Furthermore, we discussed how the ISRE term emerges from quantum-symmetry requirements during collisions.

Our experimental results are presented in Chapters 4 and 5. The results indeed manifest a significant deviation from classical diffusion, due to coherent spin interactions as a result of the ISRE. In Chapter 4, we studied the diffusion of a non-degenerate one-dimensional spin structure of two anti-parallel spin domains in uniform external magnetic fields. The quantum modifications to spin diffusion were manifested as a decrease in the oscillation rate of the spin domains and an increase in the longitudinal spin diffusion time. The results showed sensitivity to the degree of coherence in the domain-wall (Fig. 4.8), which highlighted

the quantum mechanical nature of the phenomenon more clearly. We concluded that the presence of a transverse spin component in the domain-wall combined with the anisotropy in the longitudinal and transverse spin diffusion coefficients, lead to the increased longitudinal lifetimes observed in our experiments.

We also observed an instability in the longitudinal spin component as a conversion of longitudinal spin component into transverse spin, in conformity with Castaing’s instability. The instability tends to couple the two spin components, and the longitudinal spin diffuses through the region of transverse domain-wall via transverse diffusion, which in turn leads to increased longitudinal domain lifetimes. We numerically studied the instability onset as a function of important experimental parameters: the temperature T , the domain-wall width ℓ and the scattering length a , in a broader parameter space than experimentally explored (Fig. 4.10). The results manifest that increasing ℓ and decreasing T weakens the instability, while decreasing a increases the spin rotation parameter μ and strengthens the instability.

Since the longitudinal spin component diffuses through the transverse domain-wall via transverse diffusion, the symmetry and strength of the coherent spin dynamics occurring in the domain-wall region affects the behaviour and time scale of the longitudinal diffusion significantly. In Section 4.3, we studied how the strength of the coherent dynamics affects the diffusion time scales by controllably adjusting the degree of coherence in the domain-wall region. The diffusion time scales depended sensitively on the initial degree of coherence in the domain-wall. Furthermore, by tailoring the symmetry of the transverse spin modes via applying an effective inhomogeneous magnetic field, one can further study the effect and manipulate and adjust the longitudinal diffusion time scales and spatial behaviour.

Motivated by our results in uniform magnetic fields as well as multiple theoretical predictions, we extended our diffusion dynamics studies of the two-domain spin structure by exploring the effect of applying nonuniform magnetic fields. According to our experimental results, the ISRE-dominated transverse spin dynamics occurring in the domain-wall region modifies the longitudinal diffusion noticeably. In Chapter 5, we manipulated the ISRE-dominated transverse spin dynamics by applying nonuniform external magnetic fields.

We further studied the diffusion dynamics in inhomogeneous external magnetic fields with positive and negative linear gradients. We observed a sharp contrast in the longitudinal spin domain relaxation time when positive and negative effective magnetic field gradients were applied (Fig. 5.4). For positive linear field gradients our results revealed that this modification leads to further stabilization of the longitudinal spin domains and longer longitudinal domain lifetimes. On the contrary, for negative field gradients the results showed an increase in the longitudinal spin diffusion and rapid decay of the longitudinal spin domains. In the positive field gradients we observed a dipolar transverse-spin oscillation confined in the domain-wall region (Fig. 5.7).

The coherent oscillation of the transverse spin phase is a key to the increases observed in the longitudinal spin domain lifetimes. Such coherent oscillations of the transverse spin phase were absent when negative effective field gradients were applied (Fig. 5.8). We explained that the differences in longitudinal diffusion time scales for positive and negative field gradients are due to the differences in the ISRE-generated longitudinal spin currents. For positive field gradients these coherently-generated longitudinal spin currents cancel the diffusive longitudinal spin currents, leading to increased longitudinal domain lifetimes. For negative field gradients these ISRE-generated longitudinal spin currents add to the diffusive spin currents and increase the longitudinal diffusion significantly. We also observed a suppression of the instability in the longitudinal spin component when linear external field gradients of both signs were applied (Fig. 5.10).

Looking into the future, one can extend and improve this work in many different ways. Although our experimental results validate predictions from the Boltzmann equation, only a small parameter space was explored in this work. The effect should be investigated in a broader parameter space to confirm the validity of the model with higher confidence. The first further step motivated by our numerical results presented in Chapter 4 would be exploring a broader experimental parameter-space than studied here.

One could further investigate the effect by exploring the effect of the temperature T , the domain wall size ℓ and the scattering length a on the observed instability as well as the diffusion dynamics. The scattering length a can be modified by means of Feshbach resonances

[93] to tune the ISRE strength independent of other experimental parameters. Improved optical equipment and creative microwave pulse techniques are needed to adjust ℓ controllably. For instance, using a spatial-light-modulator for creating various optical intensity profiles simplifies performing spin-state preparation significantly and allows for controllably adjusting the domain-wall width ℓ . By increasing ℓ one could observe the cross-over between stable domain structures where the transverse spin is confined in the domain-wall region, to more smoothly propagating spin-wave oscillations across the atomic distribution.

Furthermore, one can explore the effect in a broader range of interactions between collisionless and hydrodynamic regimes by adjusting the density n . Composite microwave pulse techniques can be applied to perform better atom transfer between different spin-states with higher fidelity and without loss of coherence. In addition, measuring the momentum distribution of different spin states using improved imaging protocols will be an extremely useful tool in studying transport phenomena.

Bibliography

- [1] Mike H Anderson, Jason R Ensher, Michael R Matthews, Carl E Wieman, and Eric A Cornell. Observation of Bose-Einstein condensation in a dilute atomic vapor. *Science*, 269(5221):198–201, 1995.
- [2] M-O Mewes, MR Andrews, NJ Van Druten, DM Kurn, DS Durfee, and W Ketterle. Bose-Einstein condensation in a tightly confining DC magnetic trap. *Phys. Rev. Lett.*, 77(3):416, 1996.
- [3] Simon L Cornish, Neil R Claussen, Jacob L Roberts, Eric A Cornell, and Carl E Wieman. Stable ^{85}Rb Bose-Einstein condensates with widely tunable interactions. *Phys. Rev. Lett.*, 85(9):1795, 2000.
- [4] C Bradley, CA Sackett, JJ Tollett, and Randall G Hulet. Evidence of Bose-Einstein condensation in an atomic gas with attractive interactions. *Phys. Rev. Lett.*, 75(9):1687, 1995.
- [5] Curtis Charles Bradley, CA Sackett, and RG Hulet. Bose-Einstein condensation of lithium: Observation of limited condensate number. *Phys. Rev. Lett.*, 78(6):985, 1997.
- [6] Kendall B Davis, M-O Mewes, Michael R Andrews, NJ Van Druten, DS Durfee, DM Kurn, and Wolfgang Ketterle. Bose-Einstein condensation in a gas of sodium atoms. *Phys. Rev. Lett.*, 75(22):3969, 1995.
- [7] Giacomo Roati, Matteo Zaccanti, C D'Érrico, Jacopo Catani, Michele Modugno, Andrea Simoni, Massimo Inguscio, and G Modugno. ^{39}K Bose-Einstein condensate with tunable interactions. *Phys. Rev. Lett.*, 99(1):010403, 2007.

- [8] Giovanni Modugno, Gabriele Ferrari, Giacomo Roati, Robert J Brecha, A Simoni, and Massimo Inguscio. Bose-Einstein condensation of potassium atoms by sympathetic cooling. *Science*, 294(5545):1320–1322, 2001.
- [9] Tino Weber, Jens Herbig, Michael Mark, Hanns-Christoph Nägerl, and Rudolf Grimm. Bose-Einstein condensation of cesium. *Science*, 299(5604):232–235, 2003.
- [10] Takeshi Fukuhara, Seiji Sugawa, and Yoshiro Takahashi. Bose-Einstein condensation of an ytterbium isotope. *Phys. Rev. A*, 76(5):051604, 2007.
- [11] Yosuke Takasu, Kenichi Maki, Kaduki Komori, Tetsushi Takano, Kazuhito Honda, Mitsutaka Kumakura, Tsutomu Yabuzaki, and Yoshiro Takahashi. Spin-singlet Bose-Einstein condensation of two-electron atoms. *Phys. Rev. Lett.*, 91(4):040404, 2003.
- [12] Takeshi Fukuhara, Seiji Sugawa, Yosuke Takasu, and Yoshiro Takahashi. All-optical formation of quantum degenerate mixtures. *Phys. Rev. A*, 79(2):021601, 2009.
- [13] Sebastian Kraft, Felix Vogt, Oliver Appel, Fritz Riehle, and Uwe Sterr. Bose-Einstein condensation of alkaline earth atoms: ^{40}Ca . *Phys. Rev. Lett.*, 103(13):130401, 2009.
- [14] Simon Stellmer, Meng Khoon Tey, Bo Huang, Rudolf Grimm, and Florian Schreck. Bose-Einstein condensation of strontium. *Phys. Rev. Lett.*, 103(20):200401, 2009.
- [15] Bose-einstein.
- [16] Simon Stellmer, Meng Khoon Tey, Rudolf Grimm, and Florian Schreck. Bose-Einstein condensation of ^{86}Sr . *Phys. Rev. A*, 82(4):041602, 2010.
- [17] Pascal Gerry Mickelson, YN Martinez De Escobar, M Yan, BJ DeSalvo, and Thomas C Killian. Bose-Einstein condensation of ^{88}Sr through sympathetic cooling with ^{87}Sr . *Phys. Rev. A*, 81(5):051601, 2010.
- [18] Brian DeMarco and Deborah S Jin. Onset of Fermi degeneracy in a trapped atomic gas. *Science*, 285(5434):1703–1706, 1999.

- [19] Andrew G Truscott, Kevin E Strecker, William I McAlexander, Guthrie B Partridge, and Randall G Hulet. Observation of Fermi pressure in a gas of trapped atoms. *Science*, 291(5513):2570–2572, 2001.
- [20] Brian J DeSalvo, Mi Yan, Pascal Gerry Mickelson, YN Martinez De Escobar, and Thomas C Killian. Degenerate Fermi gas of ^{87}Sr . *Phys. Rev. Lett.*, 105(3):030402, 2010.
- [21] Takeshi Fukuhara, Yosuke Takasu, Mitsutaka Kumakura, and Yoshiro Takahashi. Degenerate Fermi gases of ytterbium. *Phys. Rev. Lett.*, 98(3):030401, 2007.
- [22] Christian Gross, Tilman Zibold, Eike Nicklas, Jerome Esteve, and Markus K Oberthaler. Nonlinear atom interferometer surpasses classical precision limit. *Nature*, 464(7292):1165, 2012.
- [23] Alexander D Cronin, Jörg Schmiedmayer, and David E Pritchard. Optics and interferometry with atoms and molecules. *Rev. Mod. Phys.*, 81(3):1051, 2009.
- [24] Artur Widera, Olaf Mandel, Markus Greiner, Susanne Kreim, Theodor W Hänsch, and Immanuel Bloch. Entanglement interferometry for precision measurement of atomic scattering properties. *Phys. Rev. Lett.*, 92(16):160406, 2004.
- [25] Wolfgang P Schleich and Herbert Walther. *Elements of Quantum Information*. John Wiley & Sons, 2007.
- [26] LC Kwek and B Grémaud. *Ultracold Gases and Quantum Information: Lecture Notes of the Les Houches Summer School in Singapore: Volume 91, July 2009*, volume 91. Oxford University Press, 2011.
- [27] D Jaksch. Optical lattices, ultracold atoms and quantum information processing. *Contemporary Physics*, 45(5):367–381, 2004.
- [28] Akos Rapp, Gergely Zaránd, Carsten Honerkamp, and Walter Hofstetter. Color superfluidity and baryon formation in ultracold fermions. *Phys. Rev. Lett.*, 98(16):160405, 2007.

- [29] Maciej Lewenstein, Anna Sanpera, Veronica Ahufinger, Bogdan Damski, Aditi Sen, and Ujjwal Sen. Ultracold atomic gases in optical lattices: mimicking condensed matter physics and beyond. *Adv. Phys.*, 56(2):243–379, 2007.
- [30] Immanuel Bloch, Jean Dalibard, and Sylvain Nascimbene. Quantum simulations with ultracold quantum gases. *Nat. Phys.*, 8(4):267, 2012.
- [31] Iacopo Carusotto, Serena Fagnocchi, Alessio Recati, Roberto Balbinot, and Alessandro Fabbri. Numerical observation of Hawking radiation from acoustic black holes in atomic Bose-Einstein condensates. *New J. Phys.*, 10(10):103001, 2008.
- [32] Daniel Greif, Thomas Uehlinger, Gregor Jotzu, Leticia Tarruell, and Tilman Esslinger. Short-range quantum magnetism of ultracold fermions in an optical lattice. *Science*, page 1236362, 2013.
- [33] Jonathan Simon, Waseem S Bakr, Ruichao Ma, M Eric Tai, Philipp M Preiss, and Markus Greiner. Quantum simulation of antiferromagnetic spin chains in an optical lattice. *Nature*, 472(7343):307, 2011.
- [34] AB Bardon, S Beattie, C Luciuk, W Cairncross, D Fine, NS Cheng, GJA Edge, E Taylor, S Zhang, S Trotzky, et al. Transverse demagnetization dynamics of a unitary Fermi gas. *Science*, 344(6185):722–724, 2014.
- [35] Sebastian Hild, Takeshi Fukuhara, Peter Schauß, Johannes Zeiher, Michael Knap, Eugene Demler, Immanuel Bloch, and Christian Gross. Far-from-equilibrium spin transport in Heisenberg quantum magnets. *Phys. Rev. Lett.*, 113(14):147205, 2014.
- [36] Marco Koschorreck, Daniel Pertot, Enrico Vogt, and Michael Köhl. Universal spin dynamics in two-dimensional Fermi gases. *Nat. Phys.*, 9(7):405–409, 2013.
- [37] Ariel Sommer, Mark Ku, Giacomo Roati, and Martin W Zwierlein. Universal spin transport in a strongly interacting Fermi gas. *Nature*, 472(7342):201–204, 2011.
- [38] David Chen, Matthew White, Cecilia Borries, and Brian DeMarco. Quantum quench of an atomic Mott insulator. *Phys. Rev. Lett.*, 106(23):235304, 2011.

- [39] Giacomo Lamporesi, Simone Donadello, Simone Serafini, Franco Dalfovo, and Gabriele Ferrari. Spontaneous creation of Kibble-Zurek solitons in a Bose-Einstein condensate. *Nat. Phys.*, 9(10):656, 2013.
- [40] J.M. McGuirk, H.J. Lewandowski, D.M. Harber, T. Nikuni, J.E. Williams, and E.A. Cornell. Spatial resolution of spin waves in an ultracold gas. *Phys. Rev.Lett.*, 89(9):090402, 2002.
- [41] J.M. McGuirk and L.F. Zajiczek. Optical excitation of nonlinear spin waves. *New J. Phys.*, 12(10):103020, 2010.
- [42] Jannes Heinze, Jasper Simon Krauser, Nick Fläschner, Klaus Sengstock, Christoph Becker, Ulrich Ebling, Andre Eckardt, and Maciej Lewenstein. Engineering spin waves in a high-spin ultracold Fermi gas. *Phys. Rev. Lett.*, 110(25):250402, 2013.
- [43] Leticia Tarruell, Daniel Greif, Thomas Uehlinger, Gregor Jotzu, and Tilman Esslinger. Creating, moving and merging Dirac points with a Fermi gas in a tunable honeycomb lattice. *Nature*, 483(7389):302, 2012.
- [44] Jasper S Krauser, Jannes Heinze, Nick Fläschner, Sören Götze, Ole Jürgensen, Dirk-Sören Lühmann, Christoph Becker, and Klaus Sengstock. Coherent multi-flavour spin dynamics in a fermionic quantum gas. *Nat. Phys.*, 8(11):813, 2012.
- [45] AJ Leggett. Spin diffusion and spin echoes in liquid ^3He at low temperature. *J. Phys. C: Solid State Physics*, 3(2):448, 1970.
- [46] K Miyake, WJ Mullin, and PCE Stamp. Mean-field and spin-rotation phenomena in Fermi systems: the relation between the Leggett-Rice and Lhuillier-Laloë effects. *J. Physique*, 46(5):663–671, 1985.
- [47] S Trotzky, S Beattie, C Luciuk, S Smale, AB Bardon, T Enss, E Taylor, S Zhang, and JH Thywissen. Observation of the Leggett-Rice effect in a unitary Fermi gas. *Phys. Rev. Lett.*, 114(1):015301, 2015.

- [48] EP Bashkin. Spin waves in polarized paramagnetic gases. *JETP Letters*, 33(1):8–11, 1981.
- [49] Jean-Noël Fuchs, DM Gangardt, and Franck Laloë. Large amplitude spin waves in ultra-cold gases. *Eur. Phys. J. D*, 25(1):57–75, 2003.
- [50] C. Lhuillier and F. Laloë. Transport properties in a spin polarized gas, I. *J. Physique*, 43(2):197–224, 1982.
- [51] A. E. Meyerovich. Quantum and nonlocal coherent effects in Boltzmann gases. *Phys. Rev. B*, 39(13):9318, 1989.
- [52] HJ Lewandowski, DM Harber, DL Whitaker, and Eric A Cornell. Observation of anomalous spin-state segregation in a trapped ultracold vapor. *Phys. Rev. Lett.*, 88(7):070403, 2002.
- [53] X Du, L Luo, B Clancy, and JE Thomas. Observation of anomalous spin segregation in a trapped Fermi gas. *Phys. Rev. Lett.*, 101(15):150401, 2008.
- [54] Christian Deutsch, Fernando Ramirez-Martinez, Clement Lacroûte, Friedemann Reinhard, Tobias Schneider, Jean-Noël Fuchs, Frédéric Piéchon, Franck Laloë, Jakob Reichel, and Peter Rosenbusch. Spin self-rephasing and very long coherence times in a trapped atomic ensemble. *Phys. Rev. Lett.*, 105(2):020401, 2010.
- [55] J.N. Fuchs, O. Prévoté, and D.M. Gangardt. Castaing’s instability in a trapped ultracold gas. *Eur. Phys. J. D*, 25(2):167–171, 2003.
- [56] A. Kuklov and A. E. Meyerovich. Precessing domains and the Castaing instability in confined alkali-metal gases. *Phys. Rev. A*, 66(2):023607, 2002.
- [57] Dorna Niroomand. *Observation of the Castaing Instability in a Trapped Ultracold Bose Gas*. M.Sc. Thesis, Simon Fraser University, 2013.
- [58] J. M. McGuirk and L. F. Zajiczek. Localized collapse and revival of coherence in an ultracold Bose gas. *Phys. Rev. A*, 83(1):013625, 2011.

- [59] BR Johnson, JS Denker, N Bigelow, LP Lévy, JH Freed, and DM Lee. Observation of nuclear spin waves in spin-polarized atomic hydrogen gas. *Phys. Rev. Lett.*, 52(17):1508, 1984.
- [60] Pierre-Jean Nacher, Geneviève Tastevin, Michèle Leduc, SB Crampton, and Franck Laloë. Spin rotation effects and spin waves in gaseous $^3\text{He}\uparrow$. *J. Physique Lettres*, 45(9):441–448, 1984.
- [61] WJ Gully and WJ Mullin. Observation of spin rotation effects in polarized ^3He - ^4He mixtures. *Phys. Rev. Lett.*, 52(20):1810, 1984.
- [62] VP Silin. Oscillations of a Fermi-liquid in a magnetic field. *Sov. Phys. JETP*, 6:945–950, 1958.
- [63] N Masuhara, D Candela, DO Edwards, RF Hoyt, HN Scholz, DS Sherrill, and R Combescot. Collisionless spin waves in liquid ^3He . *Phys. Rev. Lett.*, 53(12):1168, 1984.
- [64] JR Owers-Bradley, H Chocholacs, RM Mueller, Ch Buchal, M Kubota, and F Pobell. Spin waves in liquid ^3He - ^4He mixtures. *Phys. Rev. Lett.*, 51(23):2120, 1983.
- [65] H. J. Metcalf and P. Van der Straten. *Laser Cooling and Trapping*. Springer Verlag, 1999.
- [66] Leslie Allen and Joseph H Eberly. *Optical Resonance and Two-level Atoms*, volume 28. Courier Corporation, 1975.
- [67] J. E. Williams, T. Nikuni, and Charles W. Clark. Longitudinal spin waves in a dilute Bose gas. *Phys. Rev. Lett.*, 88:230405, 2002.
- [68] Neil W Ashcroft. *Solid State Physics*. 1976.
- [69] Michel Pinard and Franck Laloë. The role of the Pauli principle in spin exchange collisions. *J. Physique*, 41(8):769–797, 1980.
- [70] Leslie E Ballentine. *Quantum Mechanics: A Modern Development Second Edition*. World Scientific Publishing Company, 2014.

- [71] MOSM Hillery, Robert F O'Connell, Marlan O Scully, and Eugene P Wigner. Distribution functions in physics: fundamentals. *Physics Reports*, 106(3):121–167, 1984.
- [72] HJ Groenewold. On the principles of elementary quantum mechanics. *Physica*, 12:405, 1946.
- [73] M. Ö. Oktel and L. S. Levitov. Internal waves and synchronized precession in a cold vapor. *Phys. Rev. Lett.*, 88(23):230403, 2002.
- [74] J. N. Fuchs, D. M. Gangardt, and F. Laloë. Internal state conversion in ultracold gases. *Phys. Rev. Lett.*, 88:230404, May 2002.
- [75] T. Nikuni, J. E. Williams, and C. W. Clark. Linear spin waves in a trapped Bose gas. *Phys. Rev. A*, 66(4):043411, 2002.
- [76] R Ragan and J Baggett. Leggett-Rice systems in harmonic traps. *J. Low Temp. Phys.*, 134(1-2):369–374, 2004.
- [77] C Lhuillier and Franck Laloë. Transport properties in a spin polarized gas, II. *J. Physique*, 43(2):225–241, 1982.
- [78] B. Castaing. Polarized ^3He . *Physica B*, 126:212–216, 1984.
- [79] G. Nunes, C. Jin, D. L. Hawthorne, A. M. Putnam, and D. M. Lee. Spin-polarized ^3He - ^4He solutions: Longitudinal spin diffusion and nonlinear spin dynamics. *Phys. Rev. B*, 46:9082–9103, 1992.
- [80] Hikota Akimoto, Osamu Ishikawa, Gong-Hun Oh, Masahito Nakagawa, Tohru Hata, and Takao Kodama. Nonlinear effects on spin waves in ^3He - ^4He dilute solutions. *J. Low Temp. Phys.*, 82(5):295–316, 1991.
- [81] R.J. Ragan and D.M. Schwarz. Castaing instabilities in longitudinal spin-diffusion experiments. *J. Low Temp. Phys.*, 109(5-6):775–799, 1997.
- [82] VV Dmitriev and IA Fomin. Coherently precessing spin structure in a normal fermi liquid. *JETP Letters*, 59:378–378, 1994.

- [83] S. D. Graham, D. Niroomand, R. J. Ragan, and J. M. McGuirk. Stable spin domains in a nondegenerate ultracold gas. *Phys. Rev. A*, 97:051603, 2018.
- [84] H. J. Lewandowski, D. M. Harber, D. L. Whitaker, and E. A. Cornell. Simplified system for creating a Bose–Einstein condensate. *J. Low Temp. Phys.*, 132(5):309–367, 2003.
- [85] H. J. Lewandowski. *Coherences and correlations in an ultracold Bose gas*. PhD thesis, University of Colorado, 2002.
- [86] D.A. Steck. Rubidium 87 D Line Data, available online at <http://steck.us/alkalidata>(revision 2.1.4), 23 December 2010.
- [87] W. Ketterle, D. S. Durfee, and D. M. Stamper-Kurn. *Making, Probing and Understanding Bose-Einstein Condensates*, *Proc. Int. School of Physics-Enrico Fermi. Ed. M. Inguscio et al.* Amsterdam: IOS Press, 1999.
- [88] S. Svanberg. *Atomic and Molecular Spectroscopy: Basic Aspects and Practical Applications*. Springer Verlag, 2004.
- [89] R. Grimm, M. Weidemüller, and Y. B. Ovchinnikov. Optical dipole traps for neutral atoms. *Advances in atomic, molecular, and optical physics*, 42:95–170, 2000.
- [90] R. König, J. H. Ager, R. M. Bowley, J. R. Owers-Bradley, and A. E. Meyerovich. Spin-wave instabilities in ^3He - ^4He solutions at high magnetic field. *J. Low Temp. Phys.*, 101(3):833–838, 1995.
- [91] RJ Ragan and RW Weber. Casting instabilities in spin-echo experiments. *J. Low Temp. Phys.*, 118(3-4):167–188, 2000.
- [92] D. Niroomand, S. D. Graham, and J. M. McGuirk. Longitudinal spin diffusion in a nondegenerate trapped ^{87}Rb gas. *Phys. Rev. Lett.*, 115(7):075302, 2015.
- [93] Christopher J Pethick and Henrik Smith. *Bose-Einstein condensation in dilute gases*. Cambridge university press, 2002.